

# Battery metals recycling by flash Joule heating

Weiyan Chen,<sup>1</sup> Ksenia V. Bets,<sup>2</sup> Rodrigo V. Salvatierra,<sup>1</sup> Guanhui Gao,<sup>2</sup> Chi Hun Choi,<sup>2</sup> Xin Wang,<sup>3</sup> John Tianci Li,<sup>1</sup> Carter Kittrell,<sup>1,4</sup> Nghi La,<sup>1</sup> Jinhang Chen,<sup>1</sup> Kevin Wyss,<sup>1</sup> Lucas Eddy,<sup>1,6</sup> Phelecia Scotland,<sup>2</sup> Bowen Li,<sup>1</sup> Bing Deng,<sup>1</sup> Mason B. Tomson,<sup>3</sup> Yimo Han,<sup>2</sup> Boris I. Yakobson,<sup>1,2,4\*</sup> and James M. Tour<sup>1,2,4,5,6\*</sup>

<sup>1</sup>Department of Chemistry, Rice University, 6100 Main Street, Houston, Texas 77005, USA

<sup>2</sup>Department of Materials Science and NanoEngineering, Rice University, 6100 Main Street, Houston, Texas 77005, USA

<sup>3</sup>Department of Civil and Environmental Engineering, Rice University, 6100 Main Street, Houston, Texas 77005, USA

<sup>4</sup>Smalley-Curl Institute, Rice University, 6100 Main Street, Houston, Texas 77005, USA

<sup>5</sup>NanoCarbon Center and the Welch Institute for Advanced Materials, Rice University, 6100 Main Street, Houston, Texas 77005, USA

<sup>6</sup>Applied Physics Program, Rice University, 6100 Main Street, Houston, Texas 77005, USA

\*Email: B.I.Y (biy@rice.edu); J.M.T (tour@rice.edu)

## Abstract

The staggering accumulation of end-of-life lithium-ion batteries (LIBs) and the growing scarcity of battery metal sources have triggered an urgent call for an effective recycling strategy. However, it is challenging to reclaim these metals with both high efficiency and low environmental footprint. We use here a pulsed direct current flash Joule heating (FJH) strategy that heats the black mass, the combined anode and cathode, to >2100 K within seconds, leading to ~1000-fold increase in

subsequent leaching kinetics. There are high recovery yields of all the battery metals, regardless of their chemistries, using even diluted acids like 0.01 M HCl, thereby lessening the secondary waste stream. The ultrafast high-temperature achieves thermal decomposition of the passivated solid-electrolyte-interphase and valance-state reduction of the hard-to-dissolve metal compounds, while mitigating diffusional loss of volatile metals. Life-cycle-analysis vs current recycling methods shows that FJH significantly reduces the environmental footprint of spent LIB processing, while turning it into an economically attractive process.

## **Main**

Battery metals are essential to produce cathode materials deployed in commercial secondary LIBs, especially for lithium, cobalt, nickel, and manganese<sup>1,2</sup>. Current strategies to collect battery metals from their natural reserves are resource- and pollution-intensive and unsustainable in the long term<sup>3-6</sup>. For example, excessive acid leaching of the cobalt ore, followed by biphasic solvent extraction, chemical precipitation, and electrowinning, has been the typical processing route for leaching weathered cobalt ore<sup>3</sup> due to the associated mineral impurities and intrinsically low concentrations of cobalt<sup>7-9</sup>. At the projected pace of nickel and cobalt mining, the world's reserves of these elements are predicted to be depleted by 2050 and 2030, respectively<sup>4,5,8</sup>. The ever-increasing demand and the foreseeable shortage of reserves have encouraged the reclaiming of battery metals from other resources such as spent LIBs. It is predicted that the global market of the battery metals in spent LIBs will reach ~\$22.8 billion in 2030 with a compound annual growth rate of ~20%<sup>10</sup>. The battery metals accounts for ~30 wt% of the battery<sup>11</sup>, which is far higher than those in natural resources<sup>8,9</sup>. Therefore, spent LIBs are a local and promising alternative resource for the supply of battery metals. A closed-loop raw material solution for spent LIBs will lessen the

need for mining of battery metals, diminish the environmental consequences of LIB disposal, and provide an economic incentive to recycle.

There have been several recycling strategies to collect the valuable metals contained in spent LIBs, including pyrometallurgy<sup>12-14</sup>, hydrometallurgy<sup>15-17</sup>, biometallurgy<sup>18</sup>, and electrochemical extraction<sup>19</sup>. Pyrometallurgy involves direct high-temperature smelting to reduce the transition metal oxidation states.<sup>12</sup> Although ~100% recovery of transition metals can be achieved, extra activation steps are required to recover lithium from the slag<sup>20</sup>. In addition, the pyrometallurgical method requires a high-temperature furnace that is highly energy-consuming<sup>19</sup>. The hydrometallurgical method also affords high yields by optimizing the leaching processes, including acid concentrations, additives, leaching temperature and time<sup>2</sup>. To achieve a high recovery yield of >95%, a large volume of concentrated inorganic acid and lengthy leaching steps are necessary, which produces problematic secondary wastes. The biometallurgical method involves the incubation of microbes and their metabolites to bioleach the metals, which can be economically and environmentally friendly<sup>18</sup>. But the long treatment period of several days to weeks can hinder its application on a large scale. Electrochemical extraction enriches the lithium from pretreated cathode materials with a lithium-selective membrane<sup>19</sup>. But a rapid and effective recycling method is desired that can achieve high extractability for all battery metals while maintaining a low environmental footprint.

Recent work has shown that electrical heating that is ultrafast, controllable, and energy-efficient can be used for materials synthesis and processing<sup>21-25</sup>. The carbothermal shock<sup>21,22</sup> and FJH<sup>23-25</sup> processes have been used to synthesize various nanomaterials with interesting structures and compositions, such as high-entropy alloys<sup>21</sup> and turbostratic graphene<sup>23,26</sup>. Programmable

heating and quenching further demonstrates the high selectivity, stability, and efficiency of ultrafast high-temperature reactions for C<sub>2</sub>-products and NH<sub>3</sub> synthesis<sup>27</sup>.

Here we show that the FJH process is used to activate diverse combinations of black mass, as it is known and routinely used in the industry, and which contains a mixture of cathode and anode. A rapid electrothermal process can raise the temperature to >2100 K with both fast heating and cooling rates of >10<sup>4</sup> K s<sup>-1</sup>, leading to the thermal decomposition of the hard-to-dissolve compact solid-electrolyte-interphase (SEI), and other impurities. FJH also achieves carbothermal reduction of the transition metal compounds to their lower oxidation state or metal(0) counterparts, making them far easier to extract by dissolution. The FJH activation process of black mass boosts the leaching kinetics by ~1000-fold, and enables an increase of recovery yields for battery metals to 286%, compared to the direct leaching by 1.0 M HCl. Simultaneously, the rapid electrothermal process alleviates the diffusional loss of volatile metals, such as lithium, compared with the continuous smelting process in the pyrometallurgical method<sup>12</sup>. Therefore, all battery metals can be recovered together from the FJH-activated black mass with a high leaching efficiency of ~98%. In addition, FJH activation shows the adaptability for black mass with distinct cathode compositions, structures, and states-of-health (Supplementary Table 1). The FJH activation strategy is scalable and energy-efficient with a low electrical energy consumption of ~234 kWh ton<sup>-1</sup> or \$9.4 ton<sup>-1</sup>. Life-cycle-analysis<sup>28</sup> comparisons to pyrometallurgy and hydrometallurgy methods indicates that the FJH activation can significantly reduce the total energy, water, acid consumption, and greenhouse gas (GHG) emissions, underscoring the favorable environmental and economic impact when applying FJH activation for spent battery recycling.

## Results

### **Acid-extractable battery metals in black mass.**

Seven types of black mass, named from BM-1 to BM-7, are used in this study (Table 1). The total content of battery metals from black mass, including lithium, cobalt, nickel, manganese, and iron, were quantified by the *aqua regia* analytical method<sup>29</sup>. For BM-1, the total amounts of lithium and transition metals are 36.1 g kg<sup>-1</sup>, and 409.5 g kg<sup>-1</sup>, respectively (Supplementary Fig. 1), which are much higher than the metals content from natural resources, underscoring that black mass is a preferred source for the supply of battery metals. Acid-leachable battery metals are extracted by 1.0 M HCl. Similar pH-dependent leachabilities are observed for all the black mass types. BM-1 shows the lowest recovery yield ( $Y_0$ ) of ~34.2% (Fig. 1a), therefore, unless otherwise specified, BM-1 is the test case upon which we apply FJH as described below. By changing the acid concentration from 0.01 M to 12.0 M, strong correlations between pH and  $Y_0$  are observed for both lithium and transition metals (Fig. 1b). There is a rapid incline in  $Y_0$  as the acid concentration increases, and only when the concentration is  $\geq 6.0$  M do the  $Y_0$  values of lithium and transition metals exceed 90% (Fig. 1b).

The low  $Y_0$  is attributed to limited thermodynamics and sluggish kinetics of dissolution. The black mass includes graphite and Li<sub>0.68</sub>CoO<sub>2</sub>, as shown in the X-ray diffraction (XRD) analysis (Supplementary Fig. 2). Compared to LiCoO<sub>2</sub>, partial delithiation causes the increase in the oxidation states<sup>30</sup> for cobalt from +3 to +(3+ $\delta$ ) ( $0 < \delta < 1$ ), as confirmed by high-resolution X-ray photoelectron spectroscopy (XPS) (Fig. 1c). However, there is a positive correlation between the oxidation state of metal and the Gibbs free energy change ( $\Delta G$ ) of the acid leaching reaction (Fig. 1d, Supplementary Table 2). Consequently, it becomes less thermodynamically favorable for the metallic compounds to dissolve in the acid solution as their oxidation state increases<sup>31</sup>. For

example<sup>2</sup>, the solubility of  $\text{Co}^{3+}$  is  $>10^8$  lower than that of  $\text{Co}^{2+}$  at the same pH. To compare the leachability, we used here 1.0 M HCl leaching as the standard protocol.

The repeated electrochemical cycling in LIBs incurs the accumulation of a compact SEI layer<sup>32-34</sup>. XPS analyses show that the layer includes various organic and inorganic salts that precipitate as surface films on the electrodes (Fig. 1e, Supplementary Fig. 3). Scanning electron microscopy (SEM) and corresponding elemental analyses confirm the presence of binder and conductive carbon as impurities to impede the contact with the solution (Fig. 1f, Supplementary Fig. 4). The SEI effectively passivates the surface and prevents direct contact between the active materials and electrolyte, leading to parasitic reactions<sup>32</sup>. The SEM images and corresponding elemental mappings verify the existence of partially etched microparticles with porous structures, even when extending leaching times to 24 h (Supplementary Fig. 5). The remaining crystalline materials include  $\text{Li}_{0.28}\text{CoO}_2$ ,  $\text{Co}_3\text{O}_4$  and graphite, as shown in the XRD analyses (Supplementary Fig. 6). The amorphous surface layer and intact cathode core structure of the black mass after acid leaching are observed from high-resolution transmission electron microscopy (HR-TEM) and corresponding fast Fourier transform (FFT) patterns (Supplementary Fig. 7). Hence, the SEI passivation layer of the black mass affects the acid leaching rate, leading to slow dissolution kinetics and low leachability.

To solve the kinetic and thermodynamic restrictions of the acid leaching process, the removal of the SEI and reduction of the battery metals are necessary. The 800 K-calcination method can effectively remove the passivating SEI layer and other impurities due to their thermal instability<sup>2</sup>, and further extended by the 2000 K-reduction of the transition metal oxides<sup>12,35</sup>. Carbonaceous components such as graphite and conductive carbon can lower the reduction temperature to  $\sim 1800$  K, as shown in the Ellingham diagram<sup>36</sup> (Fig. 1g, Supplementary Table 3). However, at this

temperature, some battery metals have high vapor pressures, including lithium and manganese (Fig. 1h), leading to diffusional loss during the prolonged calcination process. Therefore, a rapid and high-temperature treatment is proposed here to address this problem (Fig. 2a, Supplementary Note 1).

### **Improved recovery yield of battery metals from black mass by FJH activation.**

In the FJH activation process, the raw, non-thermally treated black mass is directly used as the reactant without further treatment. Safety notes<sup>37,38</sup> are listed in Supplementary Note 2. After loading the powdered sample inside a quartz tube between two graphite electrodes, the resistance of the sample is controlled by the compression on the electrodes (Fig. 2b, Supplementary Fig. 8). The capacitor banks are connected to provide electrothermal energy to the reactant. Compared to the graphite and conductive carbon in the mixture, the cathode particles and SEI layer are more resistive and experience a larger power dissipation as anticipated by Joule's law<sup>39</sup>. These local hotspots allow effective Joule heating and they trigger the thermal transformation to activate the black mass, leading to the improvement of leachability (Figs. 2b-c). Detailed flash parameters are listed in Table 2. For a typical FJH activation process with discharging voltage of 80 V, duration of 0.11 s and resistance of 1.5 ohm, the peak current reaches  $\sim 104$  A (Fig. 2d). The real-time temperature is recorded using a high-temperature infrared thermometer, showing a maximum temperature  $>2100$  K during the FJH activation process. The heating and cooling rate are ultrafast, at  $\sim 5.3 \times 10^4$  and  $\sim 1.1 \times 10^4$  K s<sup>-1</sup>, respectively (Fig. 2e). Since the FJH duration is short at  $\sim 0.11$  s and the specific energy density is high at  $\sim 840$  J g<sup>-1</sup>, the specific input power reaches 7.6 kW g<sup>-1</sup>, driving the rapid and high-temperature activation process. The product is called FJH-activated black mass. The recovery yields of battery metals from FJH-activated black mass ( $Y$ ) are calculated

and compared with those of the starting black mass ( $Y_0$ )<sup>31</sup> (Supplementary Note 3). To exclude any contamination from other parts of the FJH equipment, the battery metal contents from the quartz tube, copper wool, and graphite spacers, are measured and they show  $>10^3$  lower concentration of the measured elements (Supplementary Fig. 9). The metal contributions from the other parts are therefore ignored in the calculations.

As the flash voltage increases from 40 V to 80 V, the leachability of lithium and transition metals increase (Fig. 2f). Further increase of the flash voltage causes the loss of the metals and lowers  $Y$  from the FJH-activated black mass (Supplementary Fig. 10). Similar improvement can be observed when increasing the flash duration from 65 ms to 110 ms with flash voltage at 80 V (Fig. 2g). At  $\sim 80$  V and 110 ms, the 1.0 M HCl-extractable contents of lithium and transition metals are  $35.2 \text{ g kg}^{-1}$  and  $407.0 \text{ g kg}^{-1}$ , respectively, corresponding to the  $Y$  of both lithium and transition metals of  $\sim 98\%$ . This result indicates that there are notable increases of the recovery yield ( $Y/Y_0$ ) of lithium and transition metals to  $\sim 161\%$  and  $309\%$ , respectively, compared with  $Y_0$  of the black mass,  $\sim 62\%$  and  $\sim 33\%$  for lithium and transition metals, respectively, using 1.0 M HCl (Figs. 2g-h). The pH-dependent leaching results of FJH-activated black mass are investigated and compared to those of black mass (Supplementary Fig. 11). As the acid concentration declines by  $100\times$  to 0.01 M HCl (pH 2),  $Y$  of lithium and transition metals are  $\sim 74\%$  and  $\sim 70\%$  for FJH-activated black mass, substantially higher than those of black mass under the same leaching condition where  $Y_0 \sim 12\%$  and  $\sim 9\%$  for lithium and transition metals, respectively. These  $Y$  are even higher than  $Y_0 \sim 62\%$  and  $\sim 33\%$  for lithium and transition metals, respectively, at much higher acid concentration of 1.0 M HCl (pH 0). Even though extending the leaching time to 168 h,  $Y_0$  of black mass of  $\sim 40\%$  and  $\sim 24\%$  for lithium and transition metals, respectively, at 0.01 M HCl (pH 2) are not comparable to  $Y$  of FJH-activated black mass of  $\sim 89\%$  and  $\sim 93\%$  for lithium and

transition metals, respectively, using 0.01 M HCl (Supplementary Fig. 11). In addition, the acid leaching results of the black mass show the variation of transition metal to lithium atomic ratio in the leachates from 1.33 to 0.60 as the pH increases, while the atomic ratios are relatively constant at  $\sim 1.32$  for the FJH-activated black mass, thus making the latter preferable to prepare the resynthesized cathodes<sup>40</sup> (Supplementary Fig. 11, Supplementary Note 3). The leaching results of FJH-activated black mass, denoted by stars in Fig. 2i, are compared with hydrometallurgical<sup>1,15,16,29,41-51</sup> and pyrometallurgical<sup>12,13,36,52-54</sup> methods, highlighting the low acid concentrations required, high pulp density and superior leaching efficiencies obtained for the FJH activation strategy (Supplementary Fig. 12, Supplementary Table 4).

### **Mechanism of the improved battery metals extractability by the FJH activation.**

The acid leaching kinetics of FJH-activated black mass is studied and compared to those of black mass.  $Y$  of FJH-activated black mass increases at faster rates than  $Y_0$  of black mass. And even after  $\sim 25$  h,  $Y_0$  of lithium and transition metals are only  $\sim 76\%$  and  $\sim 44\%$ , respectively, using 1.0 M HCl (Fig. 3a, Supplementary Fig. 13), while nearly complete dissolution of the battery metals is achieved for FJH-activated black mass. The relationship between the acid leaching rate and the reaction progress for both lithium and transition metals are discussed and plotted (Figs. 3b-c, Supplementary Note 4). On average, the acid leaching rates of lithium and transition metals for FJH-activated black mass are  $\sim 100$ - and  $\sim 1000$ -fold faster, respectively, than those of black mass. Since most transition metals are cobalt ions for BM-1 (Supplementary Fig. 1), the distribution of cobalt ion in the leachates are determined by UV-vis absorbance spectra<sup>55</sup> (Supplementary Fig. 14), which demonstrates that the leaching efficiency improvements of

transition metals are mainly attributed to the increase of  $\text{Co}^{2+}$  in the leachates (Fig. 3d, Supplementary Fig. 15), indicating effective carbothermal reduction of the transition metals.

The FJH activation also increases the surface area of the black mass from  $\sim 3.3$  to  $\sim 7.1 \text{ m}^2 \text{ g}^{-1}$ , corresponding to an increase of  $\sim 115\%$  (Fig. 3e). A similar  $\sim 250\%$  increase in the concentration of nanopores is observed from the pore size distribution (Supplementary Fig. 16). The abundant surface area and nanopores allow direct contact between the black mass and the acid solution, promoting the high leaching efficiency liquid-solid reaction. The FJH-activated black mass includes metals(0), metal oxides and salts (Fig. 3f), which are the decomposition products of the SEI and the cathode particles.

First principle calculations show the energy preference,  $\Delta E$ , of the phase segregation between  $\text{LiCoO}_2$  and  $\text{Co}_3\text{O}_4 + \text{O}_2$  (Supplementary Fig. 17). Relatively low  $\Delta E$  are observed in cathodes with nearly stoichiometric composition compared to aged ones where a significant degree of delithiation is observed. This result indicates the increased effectiveness of the thermal decomposition during the FJH activation of heavily degraded cathode particles<sup>56,57</sup>. The microscale and nanoscale morphologies of FJH-activated black mass are shown in Figs. 3g-h. These crystalline materials, with primary particle sizes range from 10 nm to 50 nm, are contacted with carbon materials (Supplementary Fig. 18), which facilitates electrochemical etching during the leaching, enhancing dissolution kinetics. The partially graphitized carbon crust allows permeability of metal ions, which is also crucial for the leaching process. The simulation at high annealing temperature of  $\sim 2500 \text{ K}$  indicates an amorphous carbon structure with the density of  $0.9 \text{ g cm}^{-3}$  (Fig. 3i). First-principle calculations show significant effect of various structural elements within the amorphous carbon crust on the lithium-ion diffusion (Supplementary Figs. 19-20, Supplementary Note 5) due to the increased lithium binding to undercoordinated carbon atoms<sup>58</sup>. The annealing eliminates

unpassivated graphitic edges and point defects, thus improving lithium-ion permeability of the crust (see sample trajectory, Fig. 3i) and acid leaching kinetics, as observed in the experiment. Additionally, these nanoparticles stack together to form secondary particles with sizes up to 2  $\mu\text{m}$ . These secondary particles further aggregate to form larger microparticles of  $\sim 30 \mu\text{m}$  as shown in Fig 3j. The elemental mapping of the FJH-activated black mass confirms that the secondary particles (Fig. 3j) and the primary particles (Fig. 3k, Supplementary Fig. 21) consist of reduced transition metals due to the dispersive distribution of oxygen. The loosely formed hierarchical structure allows for the infiltration of acid during the leaching process and it accelerates the liquid-solid reaction. After the same acid leaching process for FJH-activated black mass, there are only graphite microparticles with few if any metal micro- or nanoparticles (Supplementary Fig. 22). Only graphite patterns without the metal oxides or salts are detected as shown in the XRD spectrum (Supplementary Fig. 23), indicating the nearly complete collection of the battery metals from the powder mixture. In conclusion, the improvement of the leachability is attributed to transition metal reduction, passivation layer decomposition, surface area increases together with a hierarchical structure change.

### **Economic and environmental analysis of the FJH activation recycling process.**

The prospective cradle-to-gate life cycle analysis (LCA) is considered using GREET 2020 and Everbatt 2020<sup>59,60</sup>, software developed by Argonne National Laboratory, which consists of the economic and environmental impacts from the collection of battery metals from spent LIBs (cradle) through all reaction processing involving the production of  $\sim 0.35 \text{ kg}$  cathode materials at the factory (gate). A cradle-to-gate life cycle analysis does not consider the use of the cathode materials nor their disposal (grave) since it is assumed that new cathodes and recycled cathodes

have the same usage and recycling stages. Three methods are analyzed and compared (Supplementary Note 6), including the hydrometallurgical (Fig. 4a), pyrometallurgical (Fig. 4b) and FJH activation recycling methods (Fig. 4c). A cut-off approach is employed in these methods, and the environmental impacts of the spent batteries are associated with the prior product, and they are considered as battery waste without their related burdens<sup>28</sup>.

The life cycle inventories with detailed parameters regarding the inputs and outputs of each individual step for the above methods are listed in Supplementary Table 5. Thus, the cradle-to-gate LCA (Fig. 4d-h) reflects that the FJH activation recycling method decreases the consumption of concentrated HCl by ~87%, water consumption by ~26%, energy consumption by ~15% and GHG emissions by ~23%, compared to the hydrometallurgical method. These values are attained by the optimization of the pretreatment, including the thermal treatment and its duration, and the leaching processes (Supplementary Fig. 24). Therefore, the estimated cost in treating 1 kg of spent batteries to produce ~0.35 kg of cathode materials is calculated to be ~49% lower than the hydrometallurgical method. Larger improvements are observed when comparing the FJH activation recycling method with the pyrometallurgical method. The FJH activation recycling method reduces the usage of concentrated HCl by ~59%, water consumption by ~52%, energy consumption by ~26% and GHG emissions by ~38%, reflecting the decrease in the environmental footprint and leading to the decrease in estimated cost by ~28% (Fig. 4d-h) compared to the pyrometallurgical method.

## **Discussion**

Since the post syntheses of the cathode materials from the leachates are well studied in the hydrometallurgical method<sup>40</sup>, the preparation of the resynthesized cathodes can be achieved using

the leachates collected from FJH-activated black mass by following the same procedures, including co-precipitation and high-temperature sintering<sup>40</sup>. The separation of the battery metals from the leachates is energy-intensive and not necessarily required, because the battery compositions are shifting to the multicomponent transition metal oxides with layered or rocksalt-like structures for high energy densities<sup>61,62</sup>.

The adaptability of the FJH activation recycling strategy is demonstrated here using seven different types of the black mass, from BM-1 to BM-7. Each show distinct structures, chemistries, and state-of-health (Table 1, Supplementary Note 7). Similar carbothermal reduction and formation of the simple oxides, salts and metals are observed for BM-1 to BM-7 (Supplementary Figs. 25-30), leading to large improvements of the leaching efficiencies. The average  $Y/Y_0$  are ~138% and ~202% with 1.0 M HCl (Fig. 1a, Fig. 2h) and 0.1 M HCl (Supplementary Fig. 31), respectively.

The potential scalability of the FJH activation strategy is discussed in Supplementary Note 8. To maintain the specific energy density, several general strategies are listed, including increasing the capacitance, flash repetitions and voltages. Here, the gram-scale experiment can be carried out. The programmed heating and cooling strategy is applied by variable frequency drive (VFD) to better control the electrothermal reaction (Table 2). The real-time current with on/off status and peak current ~215 A are shown in Supplementary Fig. 32. Since the production rate of >10 kg day<sup>-1</sup> flash graphene has been achieved in our laboratory *via* an automated system, the conceptual design of a continuous FJH reactor for black mass activation is further shown in Supplementary Fig. 33. Therefore, the FJH process can presumably be integrated into a continuous system for future production. In addition, the FJH method for making graphene is being industrially scaled up to 1 ton per day by mid-2023 and eventually targeted for 100 tons per day per factory<sup>63</sup>, and

that requires even a higher temperature ( $>3000$  K) and a larger energy density ( $\sim 3.6$  kJ g<sup>-1</sup>) than the LIB recycling described here. The graphitic solid residue from the acid bath can be further used for recycled anodes as we demonstrate previously<sup>64</sup>, thereby increasing the economic viability of this FJH approach.

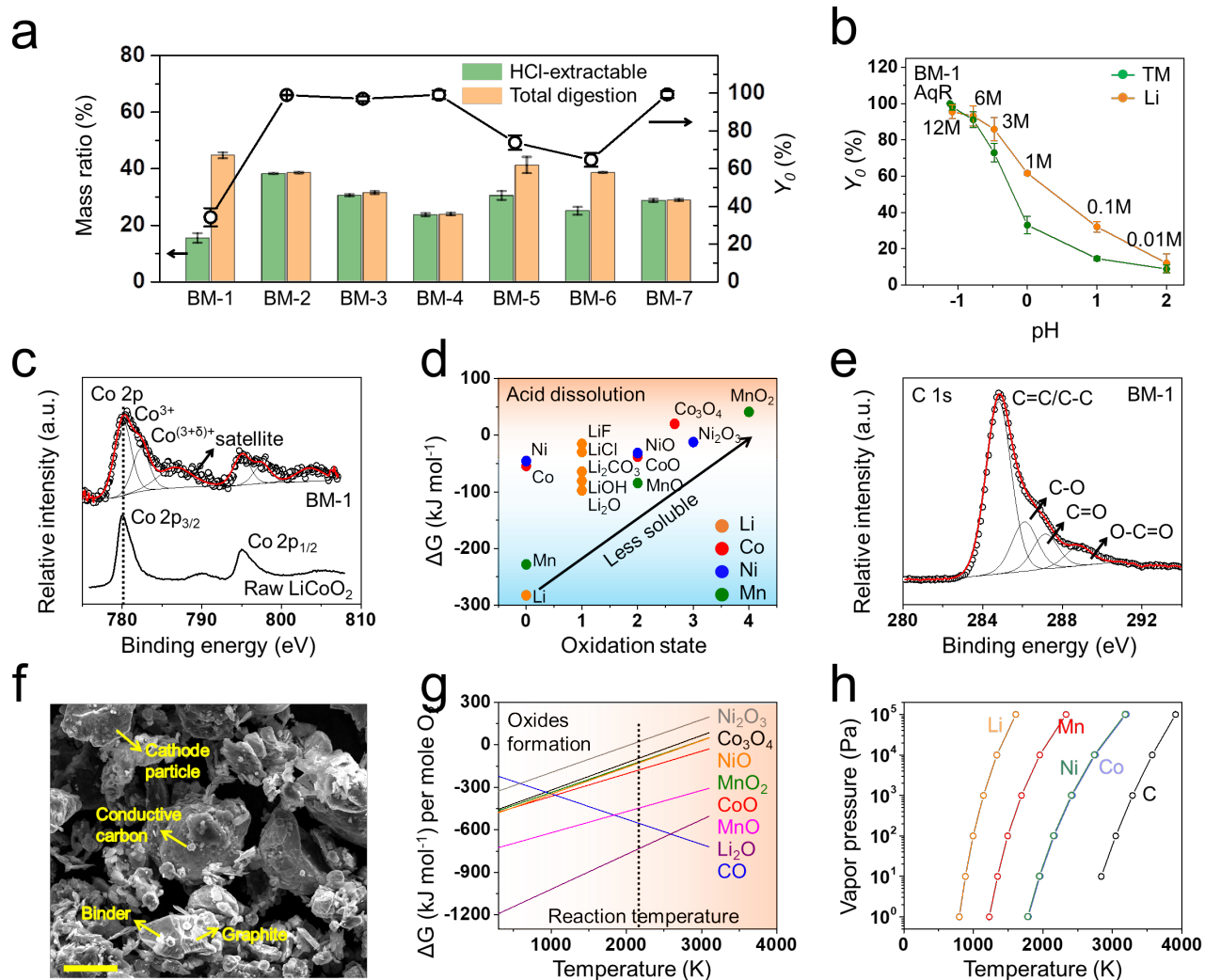


**Fig. 1 | Acid-extractable battery metals in black mass.** **a**, The HCl-extractable battery metal contents (1 M HCl, 50 °C) and the total quantification of battery metals (*aqua regia*, 50 °C) in various black mass types (BM-1 to BM-7, Table 1), and the recovery yield ( $Y_0$ ) of the battery metals from black mass by 1 M HCl. The error bars reflect the standard deviations from at least three individual measurements. The same below. **b**, pH-dependent leachability of lithium and transition metals (HCl(aq), 50 °C) from BM-1. **c**, High resolution Co 2p spectra of BM-1 and raw LiCoO<sub>2</sub>. The dashed line shows the position of the Co peak in LiCoO<sub>2</sub> for comparison. **d**, Gibbs free energy of dissolution for metals and their corresponding metal compounds in 1 M HCl. **e**,

High resolution C 1s spectrum of BM-1. **f**, SEM image of BM-1. The scale bar is 10  $\mu\text{m}$ . **g**, Ellingham diagram of carbon monoxide and various metal oxides. The dashed line denotes the FJH temperature at  $\sim 2120$  K. **h**, Vapor pressure-temperature relationship of various battery metals and carbon. AqR: *aqua regia*. TM: transition metals.

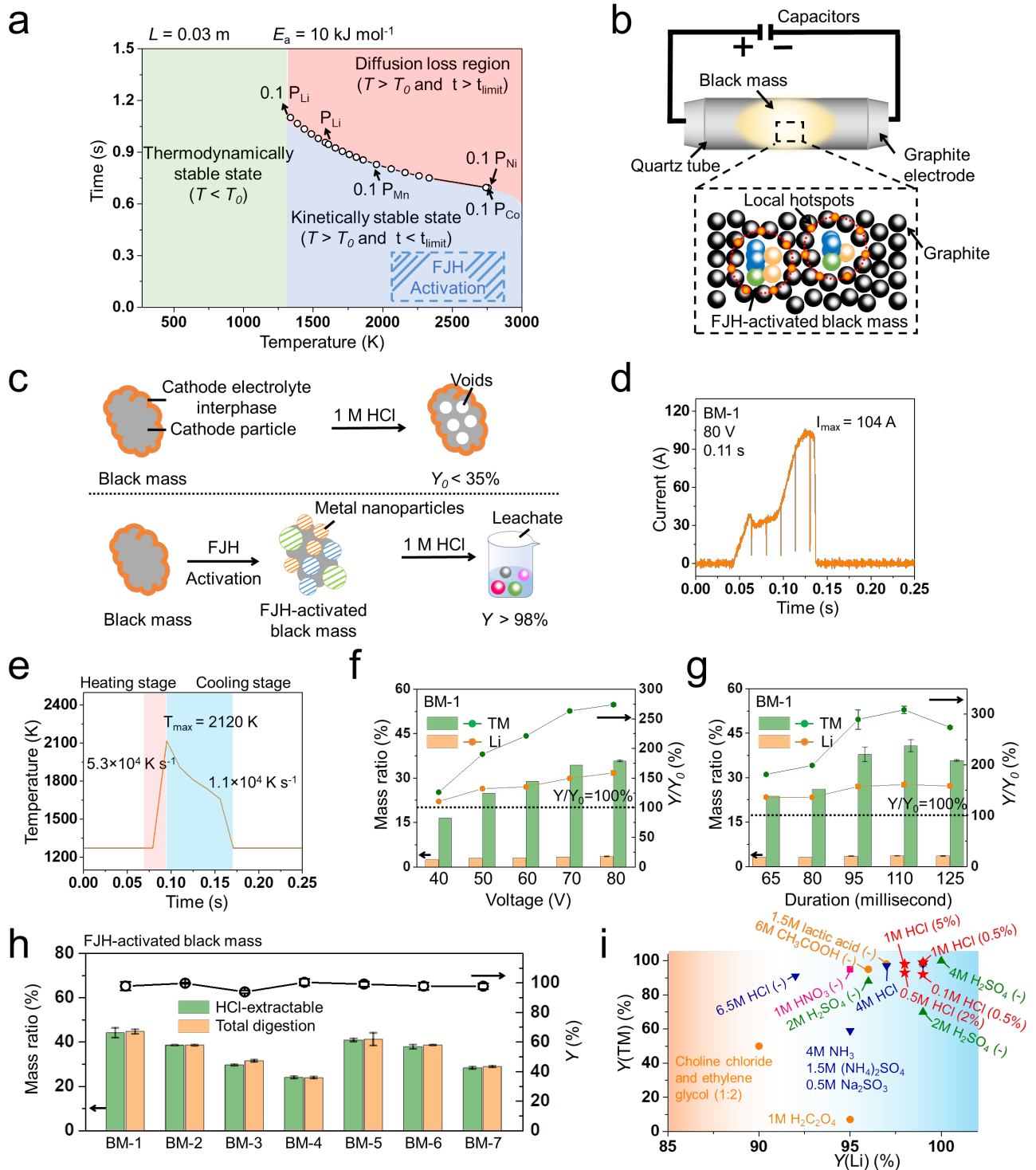


**Fig. 2 | Improved recovery yield of battery metals from different black mass by FJH activation.** **a**, The time- and temperature-dependent diagram underscoring the FJH activation process. **b**, Schematic of the FJH activation of black mass, the local hotspots of resistive cathode

particles, and **c**, the acid leaching results with and without FJH activation. **d**, Current vs time curve with the FJH activation condition of 80 V and 0.11 s. **e**, Real-time temperature measurement with the FJH activation condition of 80 V and 0.11 s. Heating and cooling stages noted by color. **f**, Relationship between the HCl-extractable battery metal contents (1 M, 50 °C) from FJH-activated BM-1, increase in recovery yield ( $Y/Y_0$ ), and the FJH voltages. The dashed line represents  $Y/Y_0 = 100\%$ , indicating the recovery result of BM-1. The error bars reflect the standard deviations from at least three individual measurements. The same below. **g**, Relationship between the HCl-extractable battery metal contents (1 M, 50 °C) from FJH-activated BM-1, increase in recovery yield ( $Y/Y_0$ ), and the FJH durations. **h**, The HCl-extractable battery metal contents (1 M, 50 °C) from FJH-activated black mass and the total quantification of battery metals (*aqua regia*, 50 °C) in various types of black mass, and the recovery yield ( $Y$ ) of the battery metals from various FJH-activated black mass by 1 M HCl. **i**, Comparison of recovery yields of lithium and transition metals by different leaching reagents, with concentration noted. The (-) indicates the usage of the reducing reagents. The red stars reflect the result from our work. Detailed parameters can be found in Supplementary Table 4. AqR: *aqua regia*. TM: transition metals.

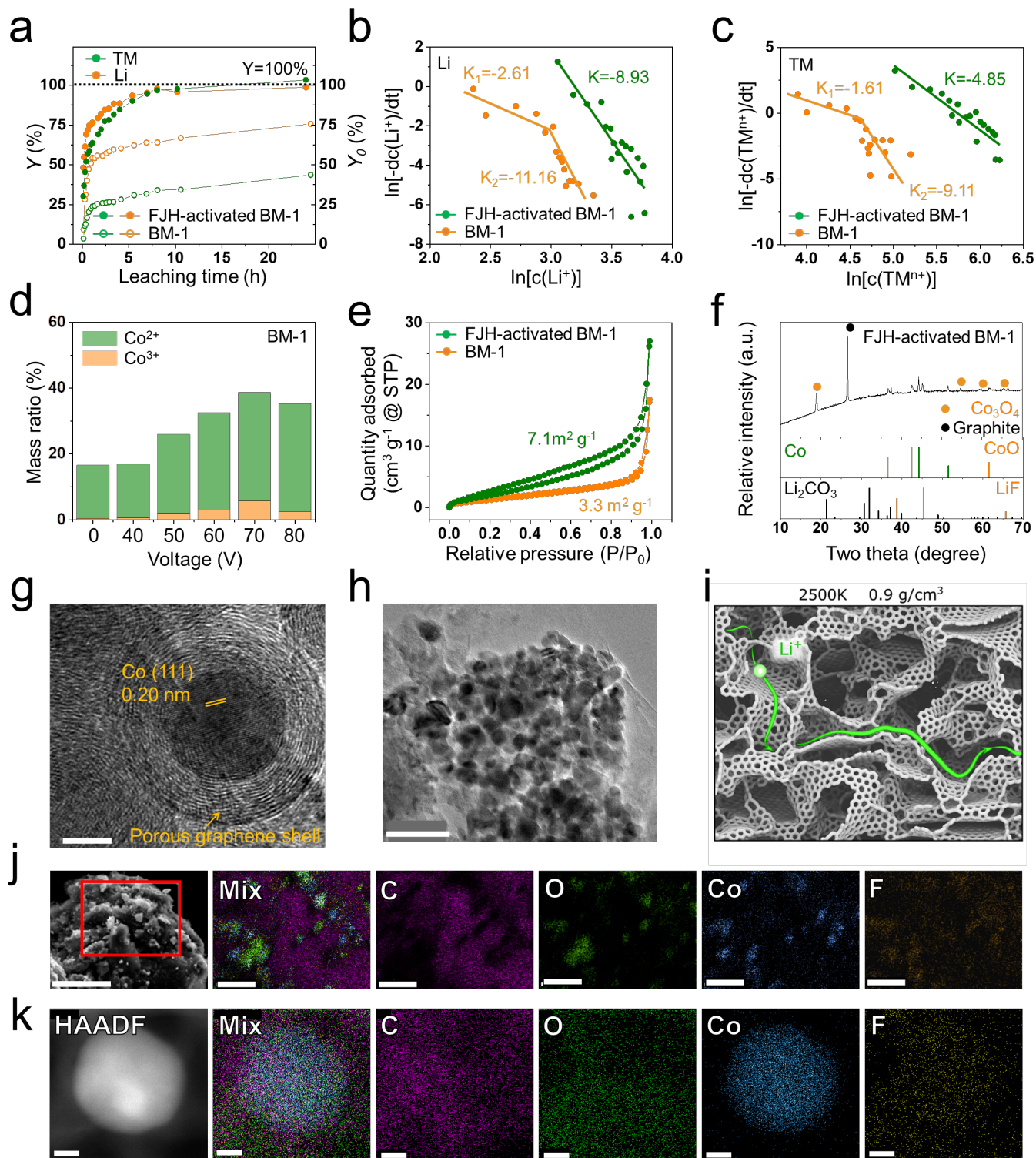


**Fig. 3 | Mechanism of the improved battery metals extractability by the FJH activation. a,** The kinetic leaching recovery yield of the BM-1 ( $Y_0$ ) and FJH-activated BM-1 ( $Y$ ) with 1 M HCl

solution (50 °C). **b**, Relationship between kinetic lithium leaching rate and the concentration of  $\text{Li}^+$  in the leachate. The slopes of fitting lines are given for different leaching stages. The same below. **c**, Relationship between kinetic transition metal leaching rate and the concentration of total transition metal ions in the leachate. **d**, Relationship between the concentration of  $\text{Co}^{2+}$ ,  $\text{Co}^{3+}$  from the HCl-extractable battery metal contents of FJH-activated BM-1 (1 M HCl, 50 °C) and the flash voltages. **e**, Nitrogen adsorption and desorption curves reporting the surface areas of the raw and FJH-activated BM-1. **f**, XRD pattern of FJH-activated BM-1. Powder Diffraction File 00-056-0159, Graphite. 00-015-0806, Co. 04-005-4912, CoO. 04-020-7500,  $\text{Co}_3\text{O}_4$ . 04-007-3587, LiF. 04-010-5115,  $\text{Li}_2\text{CO}_3$ . **g**, HR-TEM of the FJH-activated BM-1. The scale bar is 5 nm. **h**, TEM images of the FJH-activated BM-1. The scale bar is 100 nm. **i**,  $\text{Li}^+$  permeating partially graphitized amorphous carbon structure at the end of 9 ns annealing at 2500 K, where the green line indicates the calculated  $\text{Li}^+$  trajectory. **j**, Microscale morphology and corresponding element distributions about secondary particles of FJH-activated BM-1. The scale bars for elemental mapping results are 2  $\mu\text{m}$ . **k**, Nanoscale morphology and corresponding element distributions in primary particles of FJH-activated BM-1. The scale bars for elemental mapping results are 10 nm.

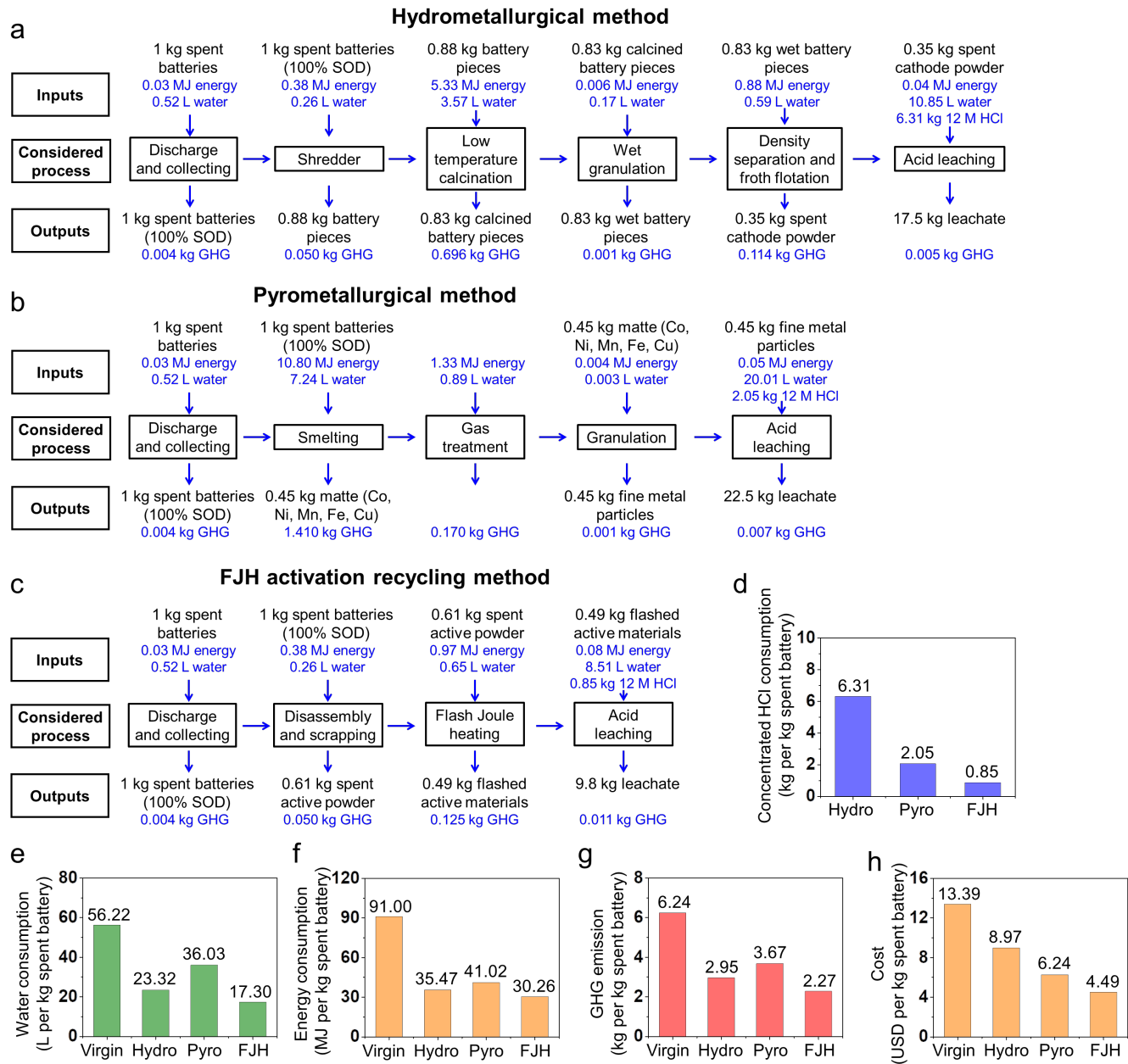


**Fig. 4 | Economic and environmental analysis of the FJH activation recycling process. a-c,** Process flow diagrams of various spent lithium-ion battery recycling routes, displaying the lifecycle inventory including all considered inputs and outputs. Incidental inputs and outputs are shown in blue font to differentiate them from explicit inputs and outputs. **a,** Hydrometallurgical method. **b,** Pyrometallurgical method. **c,** FJH activation recycling method. **d,** Concentrated 12 M HCl consumption in treating 1 kg of spent batteries. **e-h,** Water consumption, energy consumption, GHG emission, and cost, respectively, for each recycling route.

greenhouse gas emission, and cost analysis in treating 1 kg of spent batteries followed by producing ~0.35 kg cathode materials from the leachate. The effects of producing the same amount of cathode materials from mining the virgin ores are given as a comparison and it is labelled as “Virgin”. Hydro: hydrometallurgical method. Pyro: Pyrometallurgical method. FJH: Flash Joule heating activation recycling method.

## Experimental Details

### Materials

The lithium cobalt oxide ( $\text{LiCoO}_2$ , 99.8% trace metals basis, 442704-100G-A) was purchased from Millipore-Sigma. Cathode nickel-manganese-cobalt ( $\text{LiNi}_{0.8}\text{Mn}_{0.1}\text{Co}_{0.1}$ , EQ-Lib-LNCM811) powder was purchased from MTI Corporation. Lithium iron phosphate ( $\text{LiFePO}_4$ , battery grade, 0011512) was purchased from MTI Corporation. Lithium nickel cobalt aluminum oxide ( $\text{LiNi}_{0.8}\text{Co}_{0.15}\text{Al}_{0.05}$ , >98%, 760994-10G) was purchased from Millipore-Sigma. Spent commercial lithium batteries (LG Chem 112711, B052R785-9005A) were obtained from 5-year-old Lenovo laptop computers. The cobalt(II) nitrate hexahydrate ( $\text{Co}(\text{NO}_3)_2 \cdot 6\text{H}_2\text{O}$ , > 98%, ACS reagent, 239267-5G) was purchased from Millipore-Sigma. The cobalt(II) chloride ( $\text{CoCl}_2$ , 97%, 232696-5G) was purchased from Millipore-Sigma. The ammonium thiocyanate ( $\text{NH}_4\text{SCN}$ , > 97.5%, ACS reagent, 221988-100G) was purchased from Millipore-Sigma. The lithium carbonate ( $\text{Li}_2\text{CO}_3$ , 99.99% trace metals basis, 431559-50G) was purchased from Millipore-Sigma. The cobalt(II,III) oxide ( $\text{Co}_3\text{O}_4$ , 99.5% trace metals basis, 637025-25G) was purchased from Millipore-Sigma. Carbon black (CB, APS 10 nm, Black Pearls 2000) was purchased from Cabot Corporation. Quartz tubing (ID = 8 mm, L = 6 cm) was used for small batches (200 mg per batch) and quartz tubing (ID = 16 mm, L = 10 cm) was used for larger batches (2.0 g per batch) in the experiments. The standard solutions for ICP-OES tests included cobalt standard ( $1000 \pm 2$  mg/L, 30329-100ML-F), lithium standard ( $998 \pm 4$  mg/L, 12292-100ML), manganese standard ( $1003 \pm 5$  mg/L, 74128-100ML), nickel standard ( $998 \pm 4$  mg/L, 28944-100ML-F), and iron standard ( $1001 \pm 2$  mg/L, 43149-100ML-F), all of which were purchased from Millipore-Sigma. The nitric acid ( $\text{HNO}_3$ , trace metal grade, 1120060) was purchased from Fisher Chemical and hydrochloric acid ( $\text{HCl}$ , 99.999% trace metals basis, 339253-100ML) was purchased from Millipore-Sigma. Water (HPLC

Plus, 34877-4L) was purchased from Millipore-Sigma. Millipore Express PES membrane filter unit (0.22  $\mu\text{m}$ ) was purchased from Millipore-Sigma. In the work, seven different types of black mass were tested based on their chemistries and structure as listed in Table 1.

### **FJH reaction**

The FJH system was detailed in our previous publications.<sup>23</sup> A circuit diagram of the FJH setup and the FJH reaction box used in the experiments were shown in Supplementary Fig. 8 with essential safety precautions (Supplementary Note 2) for the FJH system.<sup>23</sup> The spent LIBs were discharged on a circuit until the voltage was below 2.5 V and then the electrodes were collected by manually disassembling the spent batteries. The black mass is prepared by mixing the cathode and anode wastes directly collected from the spent electrodes. The raw black mass was mixed evenly by grinding with a mortar and pestle for  $\sim 10$  min. The reactants were loaded into a quartz tube with an inner diameter of 8 mm. The mass loads in 8-mm tube were 200 mg. Graphite rods and copper wool were used as electrodes and spacers, respectively. They were used to compress the reactants as shown in Fig. 2b. The graphite rods were in contact with the sample in the quartz tube. The electrical energy was provided by a capacitor bank in the circuit with a total capacitance of 60 mF (8 mm tube). The capacitor bank was charged by a d.c. supply that could reach 400 V. The flash duration was controlled by an Arduino controller relay in the circuit acting as a high-speed switch. Various black mass materials, as listed in Table 1, were also used to demonstrate the versatility of the FJH activation method. After the FJH reaction, the reaction was permitted to cool for 3 min. For the scale-up trials, the VFD was used, which is a type of controller that drives an electric switch by varying the frequencies and durations of its power supply. The mass loads in

16-mm tube were 2.0 g. Here, 10% duty cycle for 1 s followed by 20% duty cycle for 4 s was used. The FJH voltage and capacitance were 120 V and 624 mF, respectively.

### **Low temperature lithium cobalt oxide (LT-LiCoO<sub>2</sub>) synthesis**

The lithiated spinel LT-LiCoO<sub>2</sub> samples were synthesized by a solid-state reaction as shown in previous literature.<sup>65</sup> Stoichiometric amount of Li<sub>2</sub>CO<sub>3</sub> and Co<sub>3</sub>O<sub>4</sub> were homogeneously mixed by grinding with a mortar and pestle for ~10 min. In the experiment, we used ~1.11 g Li<sub>2</sub>CO<sub>3</sub> and 2.41 g Co<sub>3</sub>O<sub>4</sub>, respectively. Then, the powder mixture was heated at 400 °C with a heating rate of 5 °C/min under air. The temperature was kept at 400 °C for 120 h, followed by the slow furnace cooling. The commercial LiCoO<sub>2</sub> samples has a layered structure and belongs to the high temperature lithium cobalt oxide (HT-LiCoO<sub>2</sub>).

### **Characterization**

The reactant and FJH products were characterized through scanning electron microscopy (SEM) using a FEI Helios NanoLab 660 DualBeam SEM at 5 kV with a working distance of 4 mm. Transmission electron microscopy (TEM) images and selected area electron diffraction (SAED) patterns were taken with a JEOL 2100F field emission gun transmission electron microscope at 200 kV. Atomic resolution high-resolution TEM (HR-TEM) and high angle annular dark-field scanning transmission electron microscopy (HAADF-STEM) images were taken with FEI Titan Themis S/TEM instrument at 80 keV after accurate spherical aberration correction. X-ray photoelectron spectroscopy (XPS) data were collected with a PHI Quantera SXM Scanning X-ray Microprobe with a base pressure of  $5 \times 10^{-9}$  Torr. Survey spectra were recorded using 0.5 eV step sizes with a pass energy of 140 eV. Elemental spectra were recorded using 0.1 eV step sizes

with a pass energy of 26 eV. All the XPS spectra were corrected using the C 1s peaks (284.8 eV) as reference. For the depth analysis, an Ar<sup>+</sup> ion sputtering source was used to etch the surface layer. The average etching rate was calibrated and was ~7 nm min<sup>-1</sup> in the experiment that can be further used to estimate the depth.<sup>11</sup> X-ray diffraction (XRD) measurements were done by a Rigaku SmartLab Intelligent XRD system with filtered Cu K $\alpha$  radiation ( $\lambda = 1.5406 \text{ \AA}$ ). The reactants and FJH products were analyzed on solid, dried samples using a Thermo Scientific Nicolet 6700 attenuated total reflectance Fourier-transform infrared (ATR-FTIR) spectrometer (Waltham, MA). TGA was performed on a Mettler Toledo TGA/DSC 3+ system. TGA and DSC data were collected at a heating rate of 10 °C/min under air. The air flow was set to 80 mL/min.

### **Sample digestion, leaching and ICP-OES measurement**

For all the black mass and FJH-activated black mass samples, the contents of acid-extractable battery metals, including lithium, cobalt, nickel, manganese, and iron were measured. The aqueous HCl and total battery metals quantification were conducted. For total battery metals quantification, ~20 mg black mass samples were digested in 3.0 mL *aqua regia* at 50 °C for 90 min. The *aqua regia* was prepared by mixing the nitric acid and hydrochloric acid in a molar ratio of ~1:3. The samples were filtered with PES membrane (0.22  $\mu\text{m}$ ) and diluted using HPLC plus grade water for inductively coupled plasma optical emission spectroscopy (ICP-OES) measurement. For HCl leaching, ~20 mg black mass samples were digested in ~5.0 mL 1.0 M HCl solution at 50 °C for 90 min. The samples were filtered with PES membrane (0.22  $\mu\text{m}$ ) and diluted using HPLC plus grade water for ICP-OES measurement. The standard procedure for leaching is with 1.0 M HCl solution at 50 °C for 90 min as shown above if not mentioned specifically.

The pH-dependent leaching dynamics were investigated by using HCl solutions with various concentrations, including 0.01, 0.1, 1.0, 3.0, 6.0, and 12.0 M, respectively as the leaching agents. The acid amounts were excess ( $\sim 10\times$  compared to the total metal amounts) to avoid obvious pH changes during the leaching tests. The leaching time and temperature were controlled the same as the total battery metals quantification tests for comparison.

For the kinetical leaching tests,  $\sim 100$  mg black mass samples were digested in 25.0 mL 1.0 M HCl solution at 50 °C.  $\sim 0.20$  mL solutions were collected after the respective leaching time. They were filtered with PES membrane (0.22  $\mu\text{m}$ ) and diluted using HPLC plus grade water for the ICP-OES measurement.

The metal content in the samples was quantified using a PerkinElmer Optima 8300 ICP-OES system. The samples were diluted with a 2% aqueous solution of nitric acid, and calibration curves were generated using 7 ICP standard solutions (blank solution, 1, 2, 5, 10, 25 and 50 ppm solutions), with the only results used from correlation coefficients that were greater than 0.999. The gas nebulizer flow rate range was set between 0.45 and 0.75 L  $\text{min}^{-1}$ , and two wavelengths per element were used in the axial mode unless otherwise stated: cobalt (228.616 and 230.786 nm), lithium (670.784 nm—radial mode—and 610.362 nm), nickel (231.604 and 341.476 nm), manganese (257.610 and 259.372 nm) and iron (238.204 and 239.562 nm).

#### **Determination of $\text{Co}^{2+}$ and $\text{Co}^{3+}$ via UV-vis measurement**

Various concentrations of the  $\text{Co}(\text{NO}_3)_2$  solutions were prepared (blank solution, 0.001, 0.002, 0.005, 0.010, 0.020 mol  $\text{L}^{-1}$ ) to generate the calibration curves. Stoichiometric amounts of 2 mol  $\text{L}^{-1}$   $\text{NH}_4\text{SCN}$  was add dropwise in the above standard solutions and solutions prepared from FJH-activated samples to enhance the sensitivity of the solutions. UV-vis (Shimadzu UV-3600 plus)

was used to collect the spectra of these standard solutions. The calibration curve (Supplementary Fig. 14) was used to calculate the concentration of  $\text{Co}^{2+}$  in the samples. The amount of  $\text{Co}^{3+}$  was calculated based on equation 1,

$$n(\text{Co}^{3+}) = n(\text{Co}^{total}) - n(\text{Co}^{2+}) \quad (1)$$

$n(\text{Co}^{3+})$ ,  $n(\text{Co}^{total})$ , and  $n(\text{Co}^{2+})$  was the amount of  $\text{Co}^{3+}$ , total cobalt ions and the amount of  $\text{Co}^{2+}$ , respectively. The total amount of cobalt ions was calculated based on the ICP-OES results.

### **Economic and environmental analysis**

The GREET 2020 and EverBatt 2020 software,<sup>58,59</sup> developed through Argonne National Laboratories, was used to estimate the cost and environment impact in adopting different recycling processes. For comparison, the cathode materials derived from virgin sources were also analyzed. Our analysis was focused on the cumulative energy use, GHG production and the potential net profit during the various recycling processes. More detailed discussion can be seen in Supplementary Note 6.

### **Atomistic first principle calculations**

Partially graphitized carbon structures were obtained by simulated annealing of a large periodic cell containing 30000 atoms with average density of  $0.9 \text{ g cm}^{-3}$ . Simulations were carried out with LAMMPS software package employing AIREBO potential for interatomic interaction. After initial annealing at 400 K for  $2 \times 10^{-9}$  s, structures were heated to the target annealing temperature with a heating rate of  $0.5 \times 10^{-12} \text{ K s}^{-1}$  using a Nose–Hoover thermostat (canonical NVT ensemble) with a temperature damping parameter of  $0.025 \times 10^{-12}$  s. The structures were held at the target annealing temperatures for  $9 \times 10^{-9}$  s.

Theoretical simulations were performed using first-principles density functional theory (DFT) calculations, as realized in the VASP software package. PAW potentials are employed for all species and the wave functions were expanded in a plane wave basis with energy cutoff of 400 eV. All calculations are spin-polarized and employ the Perdew–Burke–Ernzerhof (PBE) exchange–correlation functional. Spin–orbit coupling was included in all the calculations. Rotationally invariant variant of the LSDA+U was employed. All structures underwent unrestrained structural relaxation until the forces on all atoms were less than  $10^{-3}$  eV Å<sup>-1</sup>.

**Table 1.** The categories of black mass used in our work

Name	Materials and sources
BM-1	<ul style="list-style-type: none"><li>• Raw black mass collected from spent commercial lithium batteries (LG Chem 112711, B052R785-9005A)</li><li>• Cathode chemistry was not given</li></ul>
BM-2	<ul style="list-style-type: none"><li>• Simulated black mass prepared from <math>\text{LiNi}_{0.8}\text{Mn}_{0.1}\text{Co}_{0.1}\text{O}_2</math> cathode (NMC811)</li><li>• Mass ratio between <math>\text{LiNi}_{0.8}\text{Mn}_{0.1}\text{Co}_{0.1}\text{O}_2</math> and conductive carbon is ~2:1</li></ul>
BM-3	<ul style="list-style-type: none"><li>• Simulated black mass prepared from <math>\text{LiNi}_{0.8}\text{Co}_{0.15}\text{Al}_{0.05}\text{O}_2</math> cathode (NCA) and graphite anode</li><li>• Mass ratio between <math>\text{LiNi}_{0.8}\text{Co}_{0.15}\text{Al}_{0.05}\text{O}_2</math> and graphite is ~2:1</li></ul>
BM-4	<ul style="list-style-type: none"><li>• Simulated black mass prepared from <math>\text{LiFePO}_4</math> cathode (LFP) and graphite anode</li><li>• Mass ratio between <math>\text{LiFePO}_4</math> and graphite is ~2:1</li></ul>
BM-5	<ul style="list-style-type: none"><li>• Simulated black mass prepared from HT-<math>\text{LiCoO}_2</math> cathode (HT-LCO) and graphite anode</li><li>• Mass ratio between HT-<math>\text{LiCoO}_2</math> and graphite is ~2:1</li></ul>
BM-6	<ul style="list-style-type: none"><li>• Simulated black mass prepared from LT-<math>\text{LiCoO}_2</math> cathode (LT-LCO) and graphite anode</li><li>• Mass ratio between LT-<math>\text{LiCoO}_2</math> and graphite is ~2:1</li></ul>
BM-7	<ul style="list-style-type: none"><li>• Simulated black mass prepared from multiple cathodes (<math>\text{LiNi}_{0.8}\text{Mn}_{0.1}\text{Co}_{0.1}\text{O}_2</math>, HT-<math>\text{LiCoO}_2</math>, and <math>\text{LiFePO}_4</math> cathode)</li><li>• Mass ratio between the multiple cathodes and graphite is ~2:1</li><li>• Mass ratio of the cathodes, <math>\text{LiNi}_{0.8}\text{Mn}_{0.1}\text{Co}_{0.1}\text{O}_2</math>, HT-<math>\text{LiCoO}_2</math>, and <math>\text{LiFePO}_4</math>, is 1:1:1</li></ul>

**Table 2.** The optimized FJH activation conditions of different black mass materials

	FJH-activated BM-1	FJH-activated BM-1 (gram scale)	FJH-activated BM-2 (NMC811 cathode)
Reactant component	BM-1	BM-1	BM-2
Mass (mg)	200	2000	200
Reaction atmosphere	1 atm Ar	1 atm air	1 atm Ar
Reactant resistance (ohm)	1.5	0.6	1.5
Voltage (V)	80	120	80
Reaction time (millisecond)	110	VFD*	125
Capacitance (mF)	60	624	60
Flash repetitions	2 flashes	1 flash	2 flashes

	FJH-activated BM-3 (NCA cathode)	FJH-activated BM-4 (LFP cathode)	FJH-activated BM-5 (HT-LCO cathode)
Reactant component	BM-3	BM-4	BM-5
Mass (mg)	200	200	200
Reaction atmosphere	1 atm Ar	1 atm Ar	1 atm Ar
Reactant resistance (ohm)	0.7	1.0	0.7
Voltage (V)	80	80	80
Reaction time (millisecond)	110	110	110
Capacitance (mF)	60	60	60
Flash repetitions	2 flashes	3 flashes	2 flashes

	FJH-activated BM-6 (LT-LCO cathode)	FJH-activated BM-7 (Cathode mixtures)
Reactant component	BM-6	BM-7
Mass (mg)	200	200
Reaction atmosphere	1 atm Ar	1 atm Ar
Reactant resistance (ohm)	0.7	0.7
Voltage (V)	80	80
Reaction time (millisecond)	110	110
Capacitance (mF)	60	60
Flash repetitions	1 flash	2 flashes

Note: \*VFD is a type of controller that drives an electric switch by varying the frequencies and durations of its power supply. Here, 10% duty cycle for 1s followed by 20% duty cycle for 4 s was used.

## **Acknowledgements**

The funding of the research was provided by Air Force Office of Scientific Research (FA9550-22-1-0526) and the US Army Corp of Engineers, ERDC (W912HZ-21-2-0050). Theory and computations work (K.V.B. and B.I.Y.) was supported by the Department of Energy, BES (DE-SC0012547). Y.H. acknowledges the support from Welch Foundation (C-2065-20210327). The characterization equipment used in this project is from the Shared Equipment Authority (SEA) at Rice University. The authors acknowledge the use of the Electron Microscopy Center (EMC) at Rice University. We thank Dr. Bo Chen for helpful discussion of the XPS results, and Dr. Chris Pennington for method development of the ICP-OES methods.

## **Author contributions**

W.C. and J.M.T. conceived of the FJH process for black mass activation. W.C. conducted the FJH reaction and characterizations with the help of J.T.L. and N.L. R.V.S. helped with the design of experiments and discussion. C.K. helped with the sample digestion before ICP-OES and battery disassembly. G.G., C.H.C. and Y.H. assisted with the TEM and HAADF-STEM. J.C. and P.S. helped with standard solutions preparation. B.D. offered useful experiment suggestion. K.V.B. under the direction of B.I.Y. performed the theoretical calculation and wrote that section of the manuscript. X.W. and M.B.T. offered useful suggestions regarding the solubility of transition metals. K.W. helped with the BET. L. E. helped with the scaling trials. W.C., R.V.S and J.M.T. wrote the manuscript. All aspects of the research were overseen by J.M.T. All authors discussed the results and commented on the manuscript.

## **Disclosures—Conflict of Interest**

Rice University owns intellectual property on the flash recycling process disclosed here. That intellectual property is currently unlicensed. The authors claim no current conflicts of interest.

## References

- 1 Tran, M. K., Rodrigues, M.-T. F., Kato, K., Babu, G. & Ajayan, P. M. Deep eutectic solvents for cathode recycling of Li-ion batteries. *Nat. Energy* **4**, 339-345 (2019).
- 2 Lv, W. *et al.* A critical review and analysis on the recycling of spent lithium-ion batteries. *ACS Sustain. Chem. Eng.* **6**, 1504-1521 (2018).
- 3 Moats, M. S. & Davenport, W. G. *Treatise on process metallurgy: Industrial processes.* **3**, 625-669 (Elsevier, 2014).
- 4 Natarajan, S. & Aravindan, V. Recycling strategies for spent Li-ion battery mixed cathodes. *ACS Energy Lett.* **3**, 2101-2103 (2018).
- 5 Jacoby, M. It's time to get serious about recycling lithium-ion batteries. *Chem. Eng. News* **97** (2020). <https://cen.acs.org/materials/energy-storage/time-serious-recycling-lithium/97/i28>.
- 6 Recycle spent batteries. *Nat. Energy* **4**, 253-253 (2019).
- 7 Rao, G. V. Reference module in chemistry, molecular sciences and chemical engineering. 3491-3500 (Elsevier, 2000).
- 8 Elshkaki, A., Reck, B. K., Graedel, T. E. Anthropogenic nickel supply, demand, and associated energy and water use. *Resour. Conserv. Recycl.* **125**, 300-307 (2017).
- 9 Dehaine, Q. *et al.* Geometallurgy of cobalt ores: A review. *Miner. Eng.* **160**, 106656 (2021).

- 10 Velázquez, M., Valio, Santasalo, A., Reuter & Serna, G. A critical review of lithium-ion battery recycling processes from a circular economy perspective. *Batteries* **5**, 68 (2019).
- 11 Salvatierra, R. V., Chen, W. & Tour, J. M. What can be expected from “anode-free” lithium metal batteries? *Adv. Energy Sustain. Res.* **2**, 2000110 (2021).
- 12 Hu, X., Mousa, E., Tian, Y. & Ye, G. Recovery of Co, Ni, Mn, and Li from Li-ion batteries by smelting reduction - Part I: A laboratory-scale study. *J. Power Sources* **483**, 228936 (2021).
- 13 Tang, Y. *et al.* Recovery and regeneration of LiCoO<sub>2</sub>-based spent lithium-ion batteries by a carbothermic reduction vacuum pyrolysis approach: Controlling the recovery of CoO or Co. *Waste Manag.* **97**, 140-148 (2019).
- 14 Zhou, M., Li, B., Li, J. & Xu, Z. Pyrometallurgical technology in the recycling of a spent lithium ion battery: Evolution and the challenge. *ACS EST Engg.* **1**, 1369-1382 (2021).
- 15 Li, L. *et al.* Sustainable recovery of cathode materials from spent lithium-ion batteries using lactic acid leaching system. *ACS Sustain. Chem. Eng.* **5**, 5224-5233 (2017).
- 16 He, L.-P., Sun, S.-Y., Mu, Y.-Y., Song, X.-F. & Yu, J.-G. Recovery of lithium, nickel, cobalt, and manganese from spent lithium-ion batteries using l-tartaric acid as a leachant. *ACS Sustain. Chem. Eng.* **5**, 714-721 (2016).
- 17 Chagnes, A. & Pospiech, B. A brief review on hydrometallurgical technologies for recycling spent lithium-ion batteries. *J. Chem. Technol. Biotechnol.* **88**, 1191-1199 (2013).
- 18 Sethurajan, M. & Gaydardzhiev, S. Bioprocessing of spent lithium ion batteries for critical metals recovery – A review. *Resour. Conserv. Recycl.* **165**, 105225 (2021).
- 19 Xu, J. *et al.* A green and sustainable strategy toward lithium resources recycling from spent batteries. *Sci. Adv.* **8**, eabq7948 (2022).

- 20 Li, N. *et al.* Aqueous leaching of lithium from simulated pyrometallurgical slag by sodium sulfate roasting. *RSC Adv.* **9**, 23908-23915 (2019).
- 21 Yao, Y. *et al.* Carbothermal shock synthesis of high-entropy-alloy nanoparticles. *Science* **359**, 1489-1494 (2018).
- 22 Wang, C. *et al.* A general method to synthesize and sinter bulk ceramics in seconds. *Science* **368**, 521-526 (2020).
- 23 Luong, D. X. *et al.* Gram-scale bottom-up flash graphene synthesis. *Nature* **577**, 647-651 (2020).
- 24 Deng, B. *et al.* Phase controlled synthesis of transition metal carbide nanocrystals by ultrafast flash Joule heating. *Nat. Commun.* **13**, 262 (2022).
- 25 Chen, W. *et al.* Millisecond conversion of metastable 2D materials by flash Joule heating. *ACS Nano* **15**, 1282-1290 (2021).
- 26 Chen, W. *et al.* Heteroatom-doped flash graphene. *ACS Nano* **16**, 6646-6656 (2022).
- 27 Dong, Q. *et al.* Programmable heating and quenching for efficient thermochemical synthesis. *Nature* **605**, 470-476 (2022).
- 28 Wyss, K. M. *et al.* Upcycling end-of-life vehicle waste plastic into flash graphene. *Comms. Eng.* **1**, 3 (2022).
- 29 Zhang, P. *et al.* Hydrometallurgical process for recovery of metal values from spent lithium-ion secondary batteries. *Hydrometallurgy* **47**, 259-271 (1998).
- 30 Zhu, Z. *et al.* Gradient-morph LiCoO<sub>2</sub> single crystals with stabilized energy density above 3400 Wh L<sup>-1</sup>. *Energy Environ. Sci.* **13**, 1865-1878 (2020).
- 31 Deng, B. *et al.* Rare earth elements from waste. *Sci. Adv.* **8**, eabm3132 (2022).

- 32 Chen, W. *et al.* Brushed metals for rechargeable metal batteries. *Adv. Mater.* **34**, 2202668 (2022).
- 33 Han, B. *et al.* Additive stabilization of SEI on graphite observed using cryo-electron microscopy. *Energy Environ. Sci.* **14**, 4882-4889 (2021).
- 34 Zhang, Q. *et al.* In situ TEM visualization of LiF nanosheet formation on the cathode-electrolyte interphase (CEI) in liquid-electrolyte lithium-ion batteries. *Matter* **5**, 1235-1250 (2022).
- 35 Assefi, M., Maroufi, S., Yamauchi, Y. & Sahajwalla, V. Pyrometallurgical recycling of Li-ion, Ni–Cd and Ni–MH batteries: A minireview. *Curr. Opin. Green Sustain. Chem.* **24**, 26-31 (2020).
- 36 Li, J., Wang, G. & Xu, Z. Environmentally-friendly oxygen-free roasting/wet magnetic separation technology for in situ recycling cobalt, lithium carbonate and graphite from spent LiCoO<sub>2</sub>/graphite lithium batteries. *J. Hazard. Mater.* **302**, 97-104 (2016).
- 37 Algozeeb, W. A. *et al.* Flash graphene from plastic waste. *ACS Nano* **14**, 15595-15604 (2020).
- 38 Chen, W. *et al.* Ultrafast and controllable phase evolution by flash joule heating. *ACS Nano* **15**, 11158-11167 (2021).
- 39 Deng, B. *et al.* High-surface-area corundum nanoparticles by resistive hotspot-induced phase transformation. *Nat. Commun.* **13**, 5027 (2022).
- 40 Ma, X. *et al.* Recycled cathode materials enabled superior performance for lithium-ion batteries. *Joule.* **5**, 1-16 (2021).

- 41 Zheng, Y. *et al.* Lithium nickel cobalt manganese oxide recovery *via* spray pyrolysis directly from the leachate of spent cathode scraps. *ACS Appl. Energy Mater.* **2**, 6952-6959 (2019).
- 42 Barik, S. P., Prabakaran, G. & Kumar, L. Leaching and separation of Co and Mn from electrode materials of spent lithium-ion batteries using hydrochloric acid: Laboratory and pilot scale study. *J. Clean. Prod.* **147**, 37-43 (2017).
- 43 Lee, C. K. & Rhee, K. -I. Reductive leaching of cathodic active materials from lithium ion battery wastes. *Hydrometallurgy* **68**, 5-10 (2003).
- 44 Li, L. *et al.* Preparation of LiCoO<sub>2</sub> films from spent lithium-ion batteries by a combined recycling process. *Hydrometallurgy* **108**, 220-225 (2011).
- 45 Zhu, S. -G. *et al.* Recovery of Co and Li from spent lithium-ion batteries by combination method of acid leaching and chemical precipitation. *Trans. Nonferrous Met. Soc. China* **22**, 2274-2281 (2012).
- 46 Sun, L. & Qiu, K. Vacuum pyrolysis and hydrometallurgical process for the recovery of valuable metals from spent lithium-ion batteries. *J. Hazard. Mater.* **194**, 378-384 (2011).
- 47 Zheng, X. *et al.* Spent lithium-ion battery recycling – Reductive ammonia leaching of metals from cathode scrap by sodium sulphite. *Waste Manag.* **60**, 680-688 (2017).
- 48 Li, Q. *et al.* Process synthesis: Selective recovery of lithium from lithium-ion battery cathode materials. *Ind. Eng. Chem. Res.* **58**, 3118-3130 (2019).
- 49 Zou, H., Gratz, E., Apelian, D. & Wang, Y. A novel method to recycle mixed cathode materials for lithium ion batteries. *Green Chem.* **15**, 1183 (2013).

- 50 Huang, Y. *et al.* A stepwise recovery of metals from hybrid cathodes of spent Li-ion batteries with leaching-flotation-precipitation process. *J. Power Sources* **325**, 555-564 (2016).
- 51 Jha, M. K. *et al.* Recovery of lithium and cobalt from waste lithium ion batteries of mobile phone. *Waste Manag.* **33**, 1890-1897 (2013).
- 52 Li, M. *et al.* A SiCl<sub>4</sub>-assisted roasting approach for recovering spent LiCoO<sub>2</sub> cathode. *ACS Sustainable Chem. Eng.* **10**, 8305-8313 (2022).
- 53 Xiao, J., Li, J. & Xu, Z. Recycling metals from lithium ion battery by mechanical separation and vacuum metallurgy. *J. Hazard. Mater.* **338**, 124-131 (2017).
- 54 Xiao, J., Li, J. & Xu, Z. Novel approach for in situ recovery of lithium carbonate from spent lithium ion batteries using vacuum metallurgy. *Environ. Sci. Technol.* **51**, 11960-11966 (2017).
- 55 Ndalamo, J., Mulaba-Bafubiandi, A. F. & Mamba, B. B. UV/visible spectroscopic analysis of Co<sup>3+</sup> and Co<sup>2+</sup> during the dissolution of cobalt from mixed Co-Cu oxidized ores. *Int. J. Miner. Metall.* **18**, 260-269 (2011).
- 56 Sharifi-Asl, S. *et al.* Facet-Dependent Thermal Instability in LiCoO<sub>2</sub>. *Nano Lett.* **17**, 2165-2171 (2017).
- 57 Furushima, Y. *et al.* Thermal stability and kinetics of delithiated LiCoO<sub>2</sub>. *J. Power Sources* **196**, 2260-2263 (2011).
- 58 Liu, Y., Wang, M., Yakobson, B. I., Wood, B. C. Assessing carbon-based anodes for lithium-ion batteries: A universal description of charge-transfer binding. *Phys. Rev. Lett.* **113**, 028304 (2014).
- 59 M. Wang, *et al.* Summary of Expansions and Updates in GREET 2020, Lemont, IL, US,

- 2020 report.
- 60 Dai, Q., Gaines, L., Spangenberg, J., Kelly, J. C., Ahmed, S., and Wang, M. Everbatt: A closed-loop battery recycling cost and environmental impacts model. [www.Anl.Gov/egs/everbatt](http://www.Anl.Gov/egs/everbatt). (2019)
- 61 Zhu, Z. *et al.* Gradient Li-rich oxide cathode particles immunized against oxygen release by a molten salt treatment. *Nat. Energy* **4**, 1049-1058 (2019).
- 62 Lee, J. *et al.* Determining the criticality of Li-excess for disordered-rocksalt Li-ion battery cathodes. *Adv. Energy Mater.* **11**, 2100204 (2021).
- 63 Scaleup of FJH for graphene synthesis, see: <https://www.universalmatter.com/> (accessed 17 October 2022).
- 64 Chen, W. *et al.* Flash recycling of graphite anodes. *Adv. Mater.* DOI: 10.1002/adma.202207303. (2022).
- 65 Maiyalagan, T.; Jarvis, K. A.; Therese, S.; Ferreira, P. J.; Manthiram, A spinel-type lithium cobalt oxide as a bifunctional electrocatalyst for the oxygen evolution and oxygen reduction reactions. *Nat. Commun.*, **2014**, *5*, 3949.

## Supplemental Information

### Battery metals recycling by flash Joule heating

Weiyin Chen,<sup>1</sup> Ksenia V. Bets,<sup>2</sup> Rodrigo V. Salvatierra,<sup>1</sup> Xin Wang,<sup>3</sup> John Tianci Li,<sup>1</sup> Carter Kittrell,<sup>1,2,4</sup> Guanhui Gao,<sup>2</sup> Chi Hun Choi,<sup>2</sup> Nghi La,<sup>1</sup> Jinhang Chen,<sup>1</sup> Kevin Wyss,<sup>1</sup> Lucas Eddy,<sup>1,6</sup> Phelecia Scotland,<sup>2</sup> Bowen Li,<sup>1</sup> Bing Deng,<sup>1</sup> Mason B. Tomson,<sup>3</sup> Yimo Han,<sup>2</sup> Boris I. Yakobson,<sup>1,2,4\*</sup> and James M. Tour<sup>1,2,4,5,6\*</sup>

<sup>1</sup>Department of Chemistry, Rice University, 6100 Main Street, Houston, Texas 77005, USA

<sup>2</sup>Department of Materials Science and NanoEngineering, Rice University, 6100 Main Street, Houston, Texas 77005, USA

<sup>3</sup>Department of Civil and Environmental Engineering, Rice University, 6100 Main Street, Houston, Texas 77005, USA

<sup>4</sup>Smalley-Curl Institute, Rice University, 6100 Main Street, Houston, Texas 77005, USA

<sup>5</sup>NanoCarbon Center and the Welch Institute for Advanced Materials, Rice University, 6100 Main Street, Houston, Texas 77005, USA

<sup>6</sup>Applied Physics Program, Rice University, 6100 Main Street, Houston, Texas 77005, USA

\*Email: B.I.Y (biy@rice.edu); J.M.T (tour@rice.edu)

## Abbreviations

BM	Black mass
CB	Carbon black
CEI	Cathode electrolyte interphase
FJH	Flash Joule heating
GHG	Greenhouse gas
HT	High temperature
Hydro	Hydrometallurgical
LCA	Life cycle analysis
LCO	Lithium cobalt oxide ( $\text{LiCoO}_2$ )
LCP	Lithium cobalt phosphate ( $\text{LiCoPO}_4$ )
LFP	Lithium iron phosphate ( $\text{LiFePO}_4$ )
LIB	Li-ion battery
LT	Low temperature
NCA	Lithium nickel-cobalt-aluminum oxide ( $\text{LiNi}_{0.8}\text{Co}_{0.15}\text{Al}_{0.05}\text{O}_2$ )
NMC	Lithium nickel-manganese-cobalt oxide ( $\text{LiNi}_x\text{Mn}_y\text{Co}_z\text{O}_2$ , normally referred as $\text{NMC}_{xyz}$ , such as NMC811)
Pyro	Pyrometallurgical
SEI	Solid electrolyte interphase

## **Supplementary Note 1. Diffusion loss and fast reaction kinetics during the FJH activation process.**

### 1. Qualitative explanation

The evaporation and diffusion of the reactant can cause the loss of the battery metals, especially the metals with high vapor pressure at the reduction temperature ( $>1800$  K), such as lithium (Fig. 1h). Therefore, after the high temperature smelting, the concentration of the lithium in the remaining solid, without the formation of the slag, is always lower compared to other transition metals. The gasification of the compounds is related to the reaction temperature, while the diffusion of the gas can be controlled based on the reaction duration. A short duration can effectively reduce the diffusion loss of the volatile compounds, like the FJH activation process.

A fast carbothermal reduction can be achieved during the FJH reaction, which takes place generally in a short time domain, here  $\sim 110$  ms for the small batch trials. The diffusion of the gas is controlled by the average kinetic energy of the molecules ( $\sim 1.5RT$ ). The diffusion length  $L$  of a diffusing species is  $(2Dt)^{1/2}$ , while the diffusion coefficient ( $D$ ) is temperature ( $T$ ) dependent ( $\exp(-Ea/RT)$ ) (ref. 1). Therefore, a higher temperature can increase the average kinetic energy of the gas proportionally and increase the diffusion coefficient. Generally,  $D$  of the gas is  $10^{-6}$  to  $10^{-5}$   $\text{m}^2 \text{s}^{-1}$ . (ref. 2) Therefore, the diffusion of the gas can be negligible at the time domain of the FJH process ( $\sim 110$  ms). In addition, the dense packing of the reactant in the quartz tube and the sealed FJH jig design as shown in Supplementary Fig. 8 also facilitate the trapping of the volatiles formed during the FJH activation process. In conclusion, the diffusion loss is negligible based on the current FJH setup.

### 2. Model analysis

The time and temperature-dependent relationships with the evaporation of the volatile metals are analyzed based on the tube in Supplementary Fig. 8. In the model, we assume the activation energy of the gas diffusion  $E_a = 10 \text{ kJ mol}^{-1}$ . The shortest distance between the reactant and the environment  $S = 0.03 \text{ m}$ , which is the smallest diffusion length ( $L$ ) to cause the diffusional loss of the volatile metals. The temperature ( $T_0$ ) is the point where the vapor pressure ( $P$ ) reached 0.1 saturated vapor pressure of the most volatile metal, lithium in our case ( $P_{\text{Li}}$ ), and the evaporation becomes noticeable. The time ( $t_{\text{limit}}$ ) is the point where the  $L = S$ , which is the longest time to keep the constant temperature ( $T$ ) without the diffusional loss of the volatile metals. Based on the model,  $t_{\text{limit}}$  is within 2 s (Fig. 2a). Although larger  $S$  can increase the  $L$ , resulting in a larger  $t_{\text{limit}}$ , the total time is still impossible to expand to several minutes or hours. Besides, a smaller activation energy  $E_{a2} = 1 \text{ kJ mol}^{-1}$  is also considered, which makes the diffusion coefficient less dependent to the temperature change and makes no difference to the above discussion.

Below, we consider three different situations, according to different system temperature and reaction duration for the black mass activation process.

- (1) If the system temperature ( $T$ ) is lower than  $T_0$ , there is no obvious evaporation of the volatile metals, and extended reaction time ( $t$ ) will not cause any diffusional loss. This region is called as thermodynamically stable state. There is also no thermal reduction of the battery metals (Fig. 1g), while the decomposition of the organic compounds can happen at this temperature range. The low-temperature calcination treatment in the hydrometallurgical methods<sup>8</sup> is in this region.
- (2) If the system temperature ( $T$ ) is higher than  $T_0$  and the reaction time ( $t$ ) is longer than  $t_{\text{limit}}$ , the thermal reduction of the battery metals and evaporation of the volatile metals can

happen, which results in the diffusional loss of the volatile metals. This region is called the diffusion loss region. The high-temperature calcination treatment in the pyrometallurgical methods<sup>8</sup> is in this region.

- (3) If the system temperature ( $T$ ) is higher than  $T_0$  while the reaction time ( $t$ ) is shorter than  $t_{\text{limit}}$ , the evaporation of the volatile metals can happen within the system, and there is no diffusional loss of the volatile metals. This region is called the kinetically stable region. The FJH-activation method is in this region.

### **Supplementary Note 2. SAFETY NOTES<sup>3,4</sup>**

**FJH involves high currents and voltages, which has a risk of electrical shock or even electrocution, so these features should be implemented. This list is not intended to be comprehensive, but demonstrative of the protocols needed to minimize risk.**

1. Enclose or carefully insulate all wire connections.
2. All connections, wires and components must be suitable for the high voltages and currents.
3. Be aware that component failure could cause high voltage to appear in unexpected places, such as heat sinks on the switching transistors.
4. Control wires should have opto-isolators rated for high voltage.
5. Provide a visible charge indicator. A 230 V clear glass incandescent light bulb is a good choice as the glow on the filament also provides an approximate indicator of the amount of charge on the capacitor bank. Bright light = danger!
6. Do not use toggle switches with metal toggles. If an arc develops, the metal toggle could become charged.

7. One hand rule. Use only one hand when working on the system, with the other hand not touching any grounded surface.
8. Install bleed resistors in the range of 100,000 ohms on each capacitor so that charge will always bleed off in ~1 h.
9. Provide a mechanical discharge circuit breaker switch connected to a power resistor of a few hundred ohms to rapidly bleed off the capacitor charge.
10. Provide a "kill" circuit breaker switch to disconnect the sample holder from the capacitor bank.
11. Provide an AC disconnect circuit breaker switch.
12. Post a high voltage warning signs on the apparatus.
13. Use of circuit breakers as switches. Circuit breakers have built-in arc suppression that can interrupt 1000 amps or more. Conventional switches do not have such a high level of arc suppression and can burn out or weld closed due to the high current pulses.
14. Use circuit breakers rated for DC voltage. Most AC circuit breakers have a DC rating 1/2 the voltage or less since DC arcs are much more difficult to suppress. Circuit breakers designed for DC solar power systems are a good choice.
15. When choosing circuit breakers, choose by the time curves typical for 0.1 s, rather than the steady state current rating. K-type DC circuit breakers will have ~10× higher trip current at 0.1 s compared to their rated current, and Z-type breakers will have ~4× higher trip current at 0.1 s. This "delayed trip" designed into most circuit breakers will allow much higher pulse currents than the steady state rating of the breaker.

16. Include a small amount of inductance in the discharge circuit to limit the rise time to a millisecond or more. Extremely fast discharges can damage components and cause RF interference with other lab apparatus.
17. Keep in mind that the system can discharge many thousands of Joules in milliseconds, which can cause components such as relays or even capacitors to explode. These components should be enclosed to protect against both high voltage and possible flying debris.
18. Keep a voltmeter with high voltage test leads handy at all times. When working on the capacitor bank, always check the voltage on each. A broken wire or loose connection could leave the capacitor in a charged state.
19. Wear electrically approved thick rubber gloves extending to the elbows when using the apparatus to protect from electrocution.
20. All users should be properly trained by an experienced electrical technician.
21. Have a qualified electrical engineer inspect the instrument for safety before its use and have it reinspected weekly.

### **Supplementary Note 3. Acid leaching result analysis**

#### 1. Leaching efficiency of battery metals

To evaluate the recovery yield of the acid leaching from various materials, several parameters are defined in this section.<sup>5</sup>

The total mass of the black mass is  $m$ . The total amounts of battery metals, including lithium, cobalt, nickel, manganese, and iron,  $N_{total}$ , are measured by the *aqua regia*, corresponding to the total mass  $m_{total}$ . The HCl-extractable battery metals from raw black mass,  $N_0$ , are measured by 1.0 M HCl, corresponding to the mass  $m_0$ .

The battery metal contents are evaluated by the mass ratios of the battery metals from the black mass. Therefore, the total mass ratios ( $R_{total}$ ) of the battery metals from the *aqua regia* are calculated as,

$$R_{total}(M) = \frac{m_{total}(M)}{m} \quad (1)$$

$M$  refers to the studied metal element. The recoverable mass ratios ( $R_0$ ) of the battery metals from the raw black mass by 1.0 M HCl are calculated as,

$$R_0(M) = \frac{m_0(M)}{m} \quad (2)$$

The recovery yields of battery metals from the raw black mass ( $Y_0$ ) in 1.0 M HCl are calculated as,

$$Y_0(M) = \frac{N_0(M)}{N_{total}(M)} \quad (3)$$

The HCl-extractable battery metals from FJH-activated black mass,  $N$ , are measured by 1.0 M HCl as well, corresponding to the mass  $m$ .

The recoverable mass ratio ( $R$ ) of the battery metals from the FJH-activated black mass in 1.0 M HCl is calculated as,

$$R(M) = \frac{m(M)}{m} \quad (4)$$

The recovery yields of battery metals from the FJH-activated black mass ( $Y$ ) in 1.0 M HCl are calculated as,

$$Y(M) = \frac{N(M)}{N_{total}(M)} \quad (5)$$

The increases of the recovery yields from FJH-activated black mass over the raw black mass ( $Y/Y_0$ ) by using the same leaching procedure are calculated below,

$$Y/Y_0(M) = \frac{N(M)}{N_0(M)} \quad (6)$$

If (1)  $Y/Y_0 > 1$ , the FJH activation improves the leachability of raw black mass. (2)  $Y/Y_0 = 1$ , the FJH activation does not make the difference about the leachability. (3)  $Y/Y_0 < 1$ , the FJH activation reduce the improves the leachability of raw black mass.

The same method is used to analyze the leaching efficiency ( $R$ ,  $Y$  and  $Y/Y_0$ ) by the acid with other concentrations (e.g., 0.1 M and 0.01 M HCl) as shown in Supplementary Figs. 11 and 31.

## 2. TM/Li atomic ratio

The TM/Li indicates the atomic ratio between transition metals and lithium from the leachate, which can be used to evaluate the selectivity of the recycling method and to adjust the additions when the purified leachate was used to prepare the resynthesized cathode materials.<sup>6</sup> If (1) TM/Li is  $\sim 0$ , the method is specifically used to reclaim the lithium, for example, the electrochemical extraction. (2) TM/Li is  $> 100$ , the method is specifically used to reclaim the transition metal, like the traditional pyrometallurgical method.

Ideally, a close-loop solution of the spent LIBs relies on the recycling of the lithium and transition metals simultaneously. The recovered  $\text{TM/Li} = (\text{TM/Li})_{\text{total}}$ ,  $(\text{TM/Li})_{\text{total}}$  is the ratio collected from raw black mass by *aqua regia*. During the post-synthesis process, this TM/Li ratio is generally controlled at  $\sim 1/1.05$  (Ref. 6). Therefore, a controllable and complete leaching process can be beneficial for the adjustment of the TM/Li ratio before the post-synthesis process. Previous work<sup>6</sup> has shown that the direct post-synthesis of the cathode materials from the leachates have been well developed. And the resynthesized cathode materials demonstrate the comparable electrochemical performance as the new cathode materials.

**Supplementary Note 4. Mechanism of the improved battery metals extractability by the FJH activation**

### 1. Kinetic of the acid leaching process

The reaction between the battery metals and acid can be expressed as



The factor  $n$  is dependent on the valance states of anions. Specifically,  $n = 1$ , if X is monovalent anion, like F<sup>-</sup>.  $n = 2$ , if X is divalent anion, like O<sup>2-</sup>, CO<sub>3</sub><sup>2-</sup>. The reaction kinetics can be expressed as the consumption amount of H<sup>+</sup>,  $n(H^+)$ , which is equal to the production amount of the Li<sup>+</sup>,  $n(Li^+)$ , from the above equation.

$$-\frac{dn(H^+)}{dt} = \frac{dn(Li^+)}{dt} \quad (8)$$

In order to study the effect of the FJH activation process towards the black mass, the concentration of H<sup>+</sup> is controlled to be excess (~10×) compared to the amount of the battery metals from the black mass for the kinetic study. Therefore, it is assumed that the concentration of proton [H<sup>+</sup>] is constant during the acid leaching reaction. Instead, the concentration of lithium ion [Li<sup>+</sup>] can be used to reflect the reaction progress. The reaction rate  $v$  can be expressed as,

$$v = \frac{d[Li^+]}{dt} \quad (9)$$

### 2. Kinetic equations and descriptions

The rate equation of the elementary reaction describes the relationship between the reaction rate and the change of the reactant concentration.

$$\ln\left(-\frac{dc(reactant)}{dt}\right) = k \ln c(reactant) + \ln b \quad (10)$$

The slope  $k$  reflects the order of the reaction and indicates the degree of association between the reaction rate and the concentration of the specific reactant. A larger slope  $k$  means a stronger association between the reaction rate and the concentration of the specific reactant, and *vice versa*. Here, we use the similar equation to analyze the relationship between the acid leaching

reaction rate and the concentration of the battery metals, which can also reflect the evolution of the reaction rate during the reaction progress. By using  $\text{Li}^+$  as an example, the equation can be expressed as,

$$\ln\left(-\frac{dc(\text{Li}^+)}{dt}\right) = k \ln c(\text{Li}^+) + \ln b \quad (11)$$

Since  $k < 0$ , a larger slope  $|k|$  means, as the reaction proceeds, there is a larger decrease of the leaching reaction rate, which is undesired for the fast-leaching kinetics in our case. As the reaction proceeds, the reaction rates decrease for all the battery metals. However, the decrease in the acid leaching rate of lithium and transition metals are  $\sim 10$  and  $\sim 70$  times slower for FJH-activated black mass, as indicated by the slope ( $k$ ) of the curves (Figs. 3b-c).

### **Supplementary Note 5. Atomistic simulations**

High temperature annealing during FJH activation was simulated for large amorphous carbon structure containing over 30000 atoms using AIREBO interatomic potential. Initial configurations included small graphitic domains of arbitrary shape in the 8 - 22 Å size range and up to 3 layers thick that were misaligned by up to 50 degrees and randomly positioned within the periodic cell. The remaining 65% of the atoms were provided as individual carbon atoms randomly positioned within the unit cell.

The resulting configurations were pre-annealed and slowly heated up to the target temperature. For comparison, we provide results of annealing at 700 K, 1000 K, 1500 K, 2000 K and 2500 K (Supplementary Fig. 19).

Using first principle calculations (see Methods Section of the main text), we compared diffusion of  $\text{Li}^+$  ion over various features of carbon structures to identify the effect of annealing of  $\text{Li}^+$  permeability of carbon crust. Particularly important role is played by elimination of

unpassivated graphitic edges during annealing. As demonstrated on Supplementary Fig. 20, the diffusion barrier over these structural elements can reach 1.5 eV in comparison with 0.34 eV barrier for perfect graphitic plane. Furthermore, unpassivated edges present a potential energy trap that would capture Li-ions negatively affecting leaching performance. In-plane diffusion over reconstructed di-vacancy is characterized with a 0.5 eV barrier like that seen in a graphitic plane. Additionally, larger octagonal defects allow for transmission through the surface but large barrier of 1.6 eV must be overcome. Finally, fully reconstructed graphitic edges, forming a bulb like shape<sup>14</sup> and do not obstruct Li<sup>+</sup> diffusion, acting as a smooth surface continuation with diffusion barrier of 0.4 eV.

## **Supplementary Note 6. Life cycle analysis**

### 1. Goal and scope.

The goal of the life cycle analysis is to consider and compare the potential economic and environmental effects<sup>7</sup> in collection, reaction, and post-treatment of the black mass from the spent commercial lithium-ion batteries. In particular, the GHG emission, energy consumption and water consumption are considered for the current waste management of spent lithium-ion batteries (traditional hydrometallurgical method and pyrometallurgical method) and the FJH activated hydrometallurgical method as discussed in the work. The material transportation and GHG disposal cost are outside the scope of this limited study. The cost includes raw materials cost, manufacturing cost and fixed annual capital investment. The average energy cost is \$0.04 per kWh and the cost of water is \$0.005 per gallon. The wastewater discharge fee is \$0.007 per gallon.<sup>8,9</sup> The fixed annual capital investment includes the operating labor, direct supervisory, laboratory charge, maintenance, and repairs. The manufacturing cost contains water and energy

cost, the cost of GHG emission and wastewater discharge (~30% of fixed annual capital investment) and general expense (~20% of manufacturing cost). Overhead costs (~20% of product cost) are also considered.

## 2. Scenario description, system boundaries, and inventory analysis.

Three scenarios, hydrometallurgical method, pyrometallurgical method, and FJH activation recycling method were considered in this part (Fig. 4). In all the scenarios, treating 1 kg of spent lithium-ion batteries was used to evaluate and normalize the material and energy flow according to the life cycle inventory, which is summarized in Supplementary Table 5.

**Scenario 1 Hydrometallurgical method:** In this scenario, the spent lithium-ion batteries (1 kg) were crushed and shredded after discharge pretreatment for the safety considerations. Then, the battery pieces were calcined at 873 K for 2 h to decompose the binders, electrolytes, and the formed impurities during electrochemical cycling, which was mainly the organic SEI components atop the cathode particles. The compact SEI layer could hinder the kinetics of the acid leaching process. The energy consumption for low temperature calcination was estimated based on the commercial furnace reported in previous work, whose temperature, power, and mass loading were ~873 K, 84 kW and 100 kg, respectively. The wet granulation, density separation and froth flotation were used to remove other battery components and to collect the spent cathode powder. Note that the acid amount used in the leaching step was calculated based on the mass of the solid and the pulp density (~2%). The concentration of the acid was set as 4 mol L<sup>-1</sup> (HCl solution) due to the low efficiencies with dilute acid as demonstrated in Supplementary Table 4. The separation treatment can reduce the water consumption and total

acid amounts in the acid leaching step. The GHG emission and energy consumption for individual steps were estimated from the Everbatt 2020 software and Argonne GREET model, the same below.

**Scenario 2 Pyrometallurgical method:** In this scenario, the spent batteries were directly smelted after discharge pretreatment. The temperature could be  $\sim 1873$  K and the duration is  $\sim 3$  h. The purpose of high temperature smelting is to decompose all the organic impurities and thermally reduce the transition metal oxides to their metal counterparts. The Li salts would result in the formation of the slag with Al and Ca as the byproduct. Recent work has shown the Li species can be recycled by post-treating/activating the slag or evaporating the Li species during the temperature smelting process. Here, the second strategy was applied since it has become the mainstream in the literatures. The energy consumption for high temperature smelting was estimated based on the commercial furnace, whose temperature, power, and mass loading were  $\sim 1873$  K, 16 kW and 12 kg, respectively. The exhaust gas could be toxic to the crew and harmful to the environment, therefore a gas treatment was applied followed by the high temperature smelting process. Note that the acid amount used in the leaching step was calculated based on the mass of the solid and the pulp density ( $\sim 2\%$ ). The Li species could be collected from the flue dust as  $\text{Li}_2\text{CO}_3$  by direct water-leaching as demonstrated in the recent work, and the pulp density for collecting the Li salts was  $\sim 2\%$ . Note that the manual collecting of the flue dust was not considered in the process. Therefore, the extra amount of water used to collect the Li salts was estimated as 10.57 L. The reduced transition metal chunks could dissolve in dilute acids with a high leaching efficiency as shown in Fig. 1d, therefore the concentration of the acid was set as  $1 \text{ mol L}^{-1}$  (HCl solution).

**Scenario 3 FJH activation recycling method:** In this scenario, the spent batteries were disassembled and scrapped to collect the spent active materials. The disassembly step can be achieved by a commercial core drill with a silicon carbide blade, which can reduce the manual disassembly cost. The mixed spent active materials can be directly used as the reactants for the FJH activation process without any pretreatment. The energy consumption was estimated based on the total energy output from the capacitors. Here the specific energy density was 0.44 kWh kg<sup>-1</sup>. Note that the acid amount used in the leaching step was calculated based on the mass of the solid and the pulp density (~5%). Flashed active materials include ~63 wt% cathode materials (reduced transition metals and corresponding oxides with lower valence states) compared to the feedstock used in hydrometallurgical method. Based on the leaching efficiency as shown in Supplementary Table 4, the concentration of the acid was set as 1 mol L<sup>-1</sup> (HCl solution).

Current work has shown that final leachate can be used to prepare the recycled NMC111 cathode materials by the co-precipitation and sintering. And the recycled NMC111 cathode materials demonstrated similar performance as the virgin NMC111 cathode materials. Therefore, we assumed that the synthesis of the cathode materials and the application of the synthesized cathode materials were the same for all these three scenarios. The weight of the final cathode was ~0.35 kg. Based on Everbatt 2020 software,<sup>8</sup> the water consumption, energy consumption and the GHG emissions for the cathode production step were 7.36 L, 28.80 MJ and 2.083 kg, respectively. The prospective cradle-to-gate LCA was used for each scenario to consider the economic and environmental impacts from the recycling of the spent lithium-ion batteries to all reaction processes involving the production of ~0.35 kg cathode materials from spent lithium-ion batteries.

The economic and environmental effects of producing the same amount of ~0.35 kg cathode materials from mining the virgin ores are considered as a comparison. Based on the Everbatt 2020 software,<sup>8</sup> the water consumption, energy consumption and the GHG emissions for the cathode production were 56.22 L, 91.00 MJ and 6.24 kg, respectively. And the estimated cost was ~\$13.39. A cradle-to-gate LCA does not consider the use of the cathode materials nor their disposal (grave) since it was assumed that new cathode materials and recycled cathode materials had the same, if not better, usage and recycling stages.

### 3. Life cycle impact assessment.

In this study, the environmental impacts were categorized into 5 midpoint indicators, including water consumption (Fig. 4e), GHG emissions (Fig. 4g), and energy consumptions (Fig. 4f), concentrated 12 M HCl consumption (Fig. 4d) and the estimated cost (Fig. 4h) in treating 1 kg of spent lithium-ion batteries.

### 4. Sensitivity and uncertainty.

Due to the data availability, the energy consumption, GHG emission and water consumption values for various process involved in this study were from different sources, which could introduce some uncertainty. Secondly, several assumptions were made in this study with regard to the low temperature calcination or high temperature smelting process, the production of recycled cathode materials. Thirdly, even though we proposed the scalability of the FJH activation process and calculate the energy based on 0.44 kWh kg<sup>-1</sup>, the FJH process realized in this work was on the gram scale; hence, there might be uncertainty in energy consumption when scaling up the FJH activation method to ton scale.

## Supplementary Note 7. The general applicability of FJH activation method

The diversity of the cathode chemistries on the market brings in a challenge for the adaptability of the current recycling methods, especially the hydrometallurgical method. In general, there are several different types of the cathode materials deployed in commercial lithium-ion batteries. Their materials properties and estimated market shares are provided in Supplementary Table 1.

Therefore, six different types of black mass with distinct cathode chemistries (from BM-1 to BM-6) and their mixtures (BM-7) are used as the reactants to justify the general applicability of the FJH activation method. The detailed information on these seven reactants is provided in Table 1. For these seven groups of the black mass, we demonstrate the following,

- (1) (From BM-2 to BM-5) The FJH activation method can be used to activate all these different types of cathode materials with distinct chemistries, even though there is some difference in the thermal stability between different cathode materials.
- (2) (BM-5 and BM-6) The structure difference of the cathode materials can affect the acid leaching efficiency, such as the HT-LiCoO<sub>2</sub> and the LT-LiCoO<sub>2</sub> cathode as shown in Supplementary Fig. 1. The former has a layered structure, while the latter has a spinel structure. However, it does not affect the FJH activation process, since both FJH-activated BM-5 and BM-6 show improved leaching efficiencies with  $Y/Y_0$  of ~133% and ~148%, respectively, for all the battery metals.
- (3) (BM-1 and BM-5) The battery metals are harder to recovered from the black mass collected from the spent lithium-ion battery, compared to the simulated black mass prepared from the new cathode materials. Therefore, the direct acid leaching results in lower leaching efficiencies for all the battery metals from BM-1. This is attributed to the

compact layer formed as the protective coating, which contributes to the kinetic restrictions of the acid leaching process. However, the FJH activation process can be used to solve this, since both FJH-activated BM-5 and BM-1 show improved leaching efficiencies with  $Y/Y_0$  of ~133% and ~288%, respectively, for all the battery metals.

(4) (BM-7) FJH activation method can be applied to the black mass with cathode mixtures, even though there is some difference in the thermal stability between different cathode materials.

### **Supplementary Note 8. Scaling up the FJH activation recycling method**

The scalability of the FJH process has been demonstrated by using the carbon materials as the example in our previous work. In this part, the energy consumption for the current experiment was firstly calculated as the benchmark for the scaling rule. Then, we applied this relationship to larger batch samples and demonstrated the feasibility of trials with gram size per batch. Our initial scaling up experiments demonstrated the productivity up to kg scale could be achieved in the current research lab. Since the FJH method is being industrially scaled up to 1 ton per day by Q2 2023 and continued scaling from there for flash graphene by Universal Matter, Inc. (<https://www.universalmatter.com/>, ref. 10), flash recycling has the potential to address the daunting accumulation of spent LIBs.

#### 1. Scaling rule of FJH process by theoretical analysis.

The temperature of the sample increases rapidly when the current goes through the resistive samples, and the total heat ( $Q$ ) can be expressed as

$$Q = \int I^2 R dt \tag{12}$$

$I$  is the current passing through the sample,  $R$  is the resistance, and  $t$  is the discharge time. The summation of the heat for the entire FJH process produces the total heat ( $Q$ ). Since (1) the energy conversion efficiency from the electrical energy to the thermal energy of the system can be 100% and (2) the resistance from the circuit and reaction box is far less than the reactants, therefore, the total electrothermal energy can be estimated to the electrical energy loss from the capacitor banks ( $\Delta E$ ).

$$Q = \alpha \Delta E \quad (\alpha \approx 1) \quad (13)$$

The electrical energy of the capacitor banks can be calculated based on the voltage drop as shown below,

$$\Delta E = \sum \frac{1}{2} C (V_2^2 - V_1^2) \quad (14)$$

$C$  is the capacitance of the capacitor banks,  $V_2$  and  $V_1$  are the final and initial voltage of the capacitor banks. The summation of the electrical energy loss is required if multiple flashes are involved. For the FJH activation process, the highest temperature determines whether the carbothermal reduction of the transition metal oxides and the decomposition of the other impurities can happen. Therefore, the specific electrothermal energy ( $Q_m$ ), which is used to raise the sample temperature and drive the above reactions, is critical when considering the scalability of FJH activation process.

$$Q_m = \frac{Q}{m} = \frac{\alpha \sum C (V_2^2 - V_1^2)}{2m} \quad (15)$$

$m$  is the mass of the reactant. Therefore, to maintain the same specific electrothermal energy  $Q_m$ , when the mass  $m$  increases, there are four general strategies include

- (1) increasing the capacitance  $C$  of the capacitor banks.
- (2) increasing the initial voltage  $V_1$  of the capacitor banks.
- (3) decreasing the final voltage  $V_2$  of the capacitor banks.

(4) increasing the flash repetitions  $n$ .

## 2. Energy calculation for gram-scale trials.

For the small batch (~200 mg per batch) experiments, the capacitance  $C$  was 60 mF. Based on the optimized results, the initial voltage  $V_1$  was 80 V and the final voltage  $V_2$  was ~60 V when the flash duration was 110 ms. The flash time was 2. The specific electrothermal energy  $Q_m$  can be calculated based on eq 4 above. For small batch, the  $Q_m$  is ~840 J g<sup>-1</sup>, which is equal to ~234 kWh ton<sup>-1</sup>.

For the large batch (~2 g per batch) experiments, the capacitance  $C$  was 624 mF. Based on the preliminary results, the initial voltage  $V_1$  was 120 V and the final voltage  $V_2$  was ~95 V when the variable frequency drive (VFD) was used. The flash parameter included 10% duty cycle for 1 s followed by 20% duty cycle for 4 s. For the large batch, the  $Q_m$  is ~838 J g<sup>-1</sup>, which is equal to ~234 kWh ton<sup>-1</sup>. The result indicated that the general strategies in part 1 works well to guide the scaling of the FJH activation recycling process.

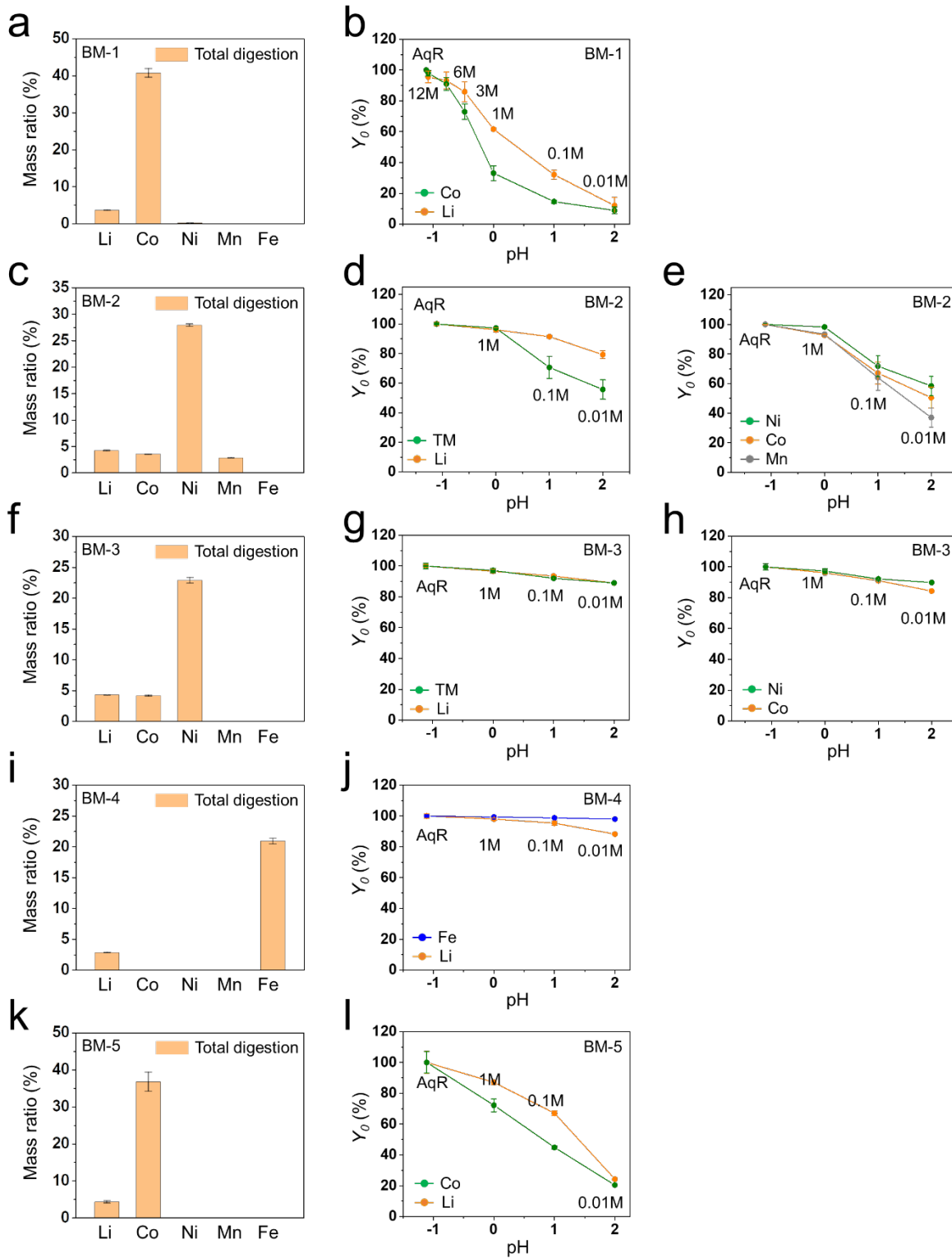
Since the production rate of >10 kg day<sup>-1</sup> flash graphene has been achieved in our laboratory *via* a continuous system. The temperature during the flash process can reach ~3400 K for the graphene conversion reaction.<sup>3,11</sup> The temperature for FJH activation recycling process is ~2200 K as we measured in Fig. 2e. The temperature was within the range of the continuum system. Therefore, the same system could potentially be applied to activate the black mass for the battery recycling.

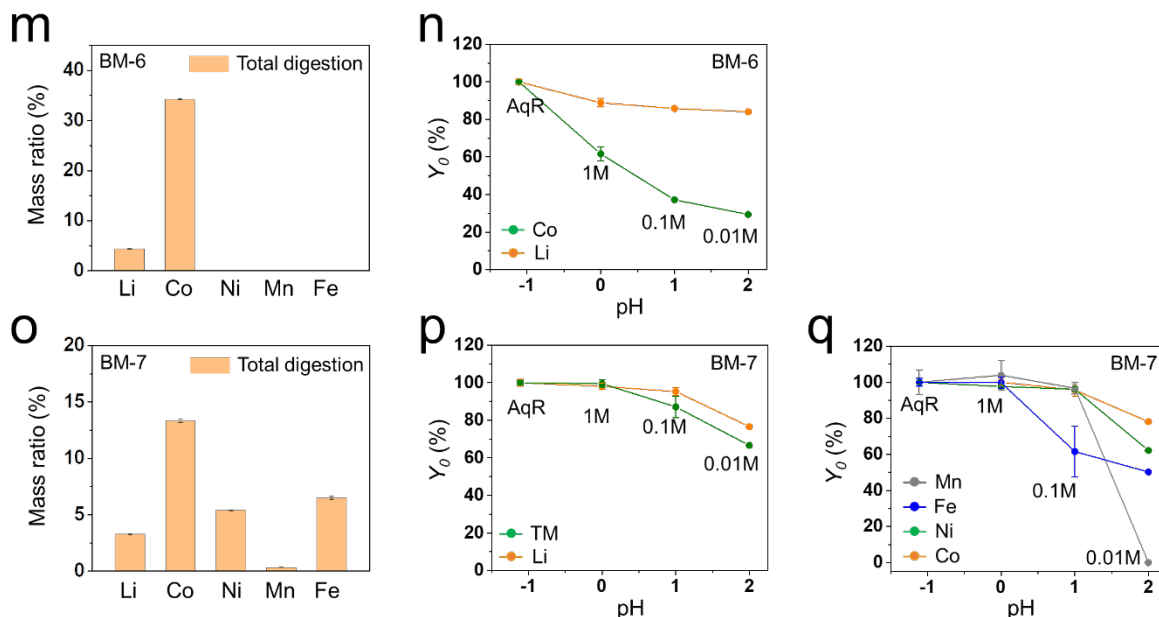
## 3. Proposed design for the FJH activation recycling process.

The FJH process could be integrated with the industrially available process for continuous running. In this part, we proposed a design combine the FJH activation process and the belt roller

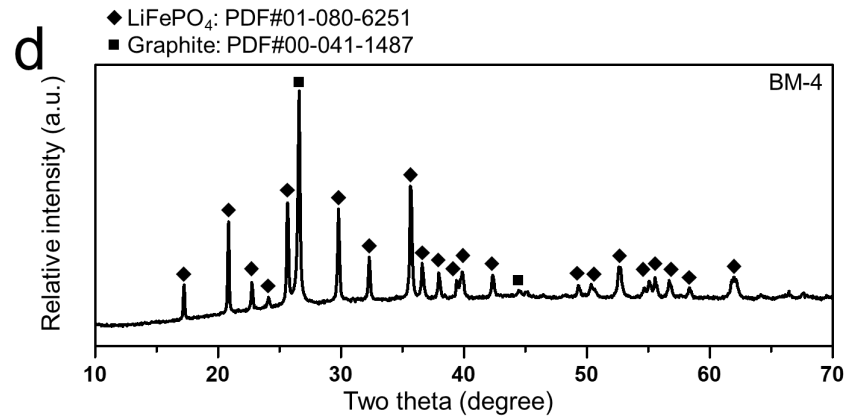
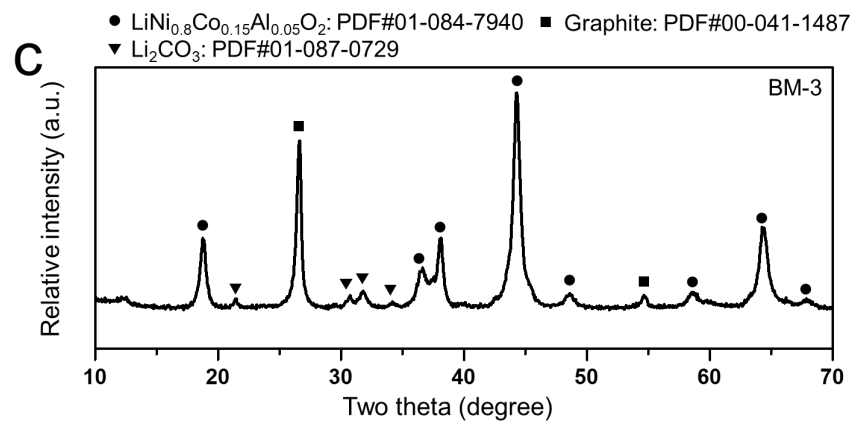
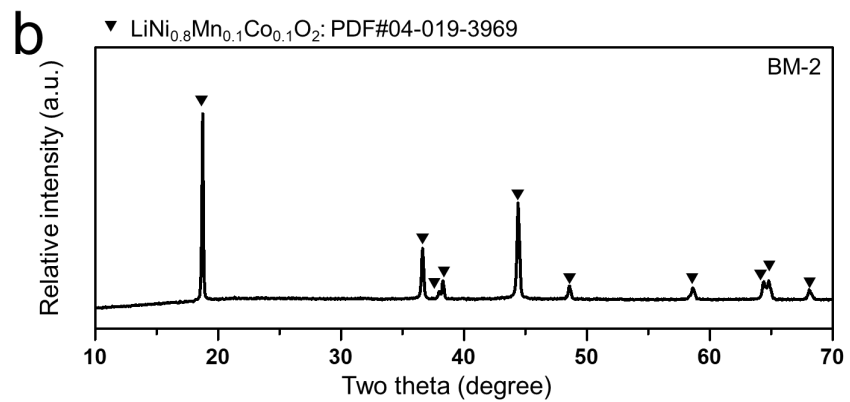
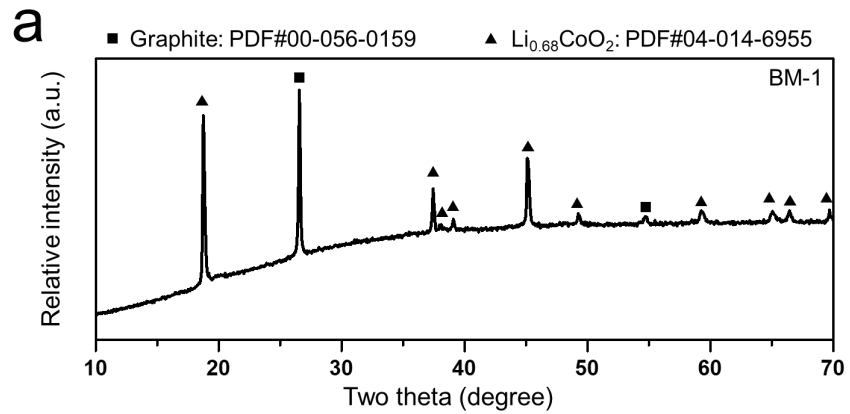
(Supplementary Fig. 33). The raw black mass material can be transferred by the sheet metal belt, which is controlled by the tensioning roller. The doctor blade can be used to control the thickness, which is related to the batch mass for the FJH reaction. The graphite electrodes from the top and bottom could be controlled to press the raw black mass until the optimized resistivity. During the FJH reaction, the electrothermal energy would be concentrated at the reactant since there is a low resistivity of the metal sheet along the electrodes by Joule's law. The vacuum chamber is used to collect the exhausted gas from the decomposition of the impurities. The FJH activated black mass is treated with dilute acid bath to collect the battery metals in the form of the mixed metal ion solution. After removing the impurities and adjusting the ion ratio to meet the stoichiometry needs, the precursors can be used to prepare the regenerated cathode materials by the co-precipitation and sintering process. The remaining solid waste from the dilute acid bath can be used to prepare the flash recycled anode as demonstrated in our current work.<sup>37</sup>

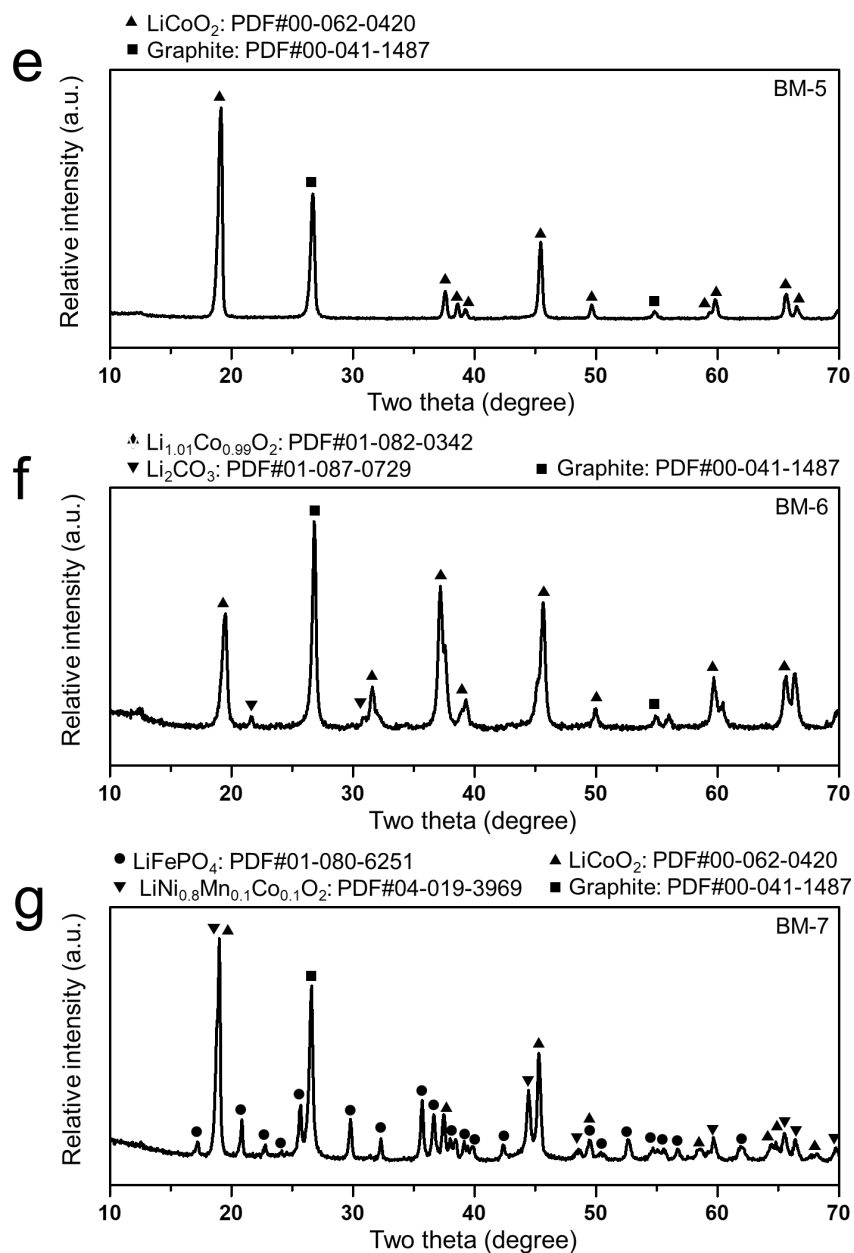
## Acid-extractable battery metals in black mass



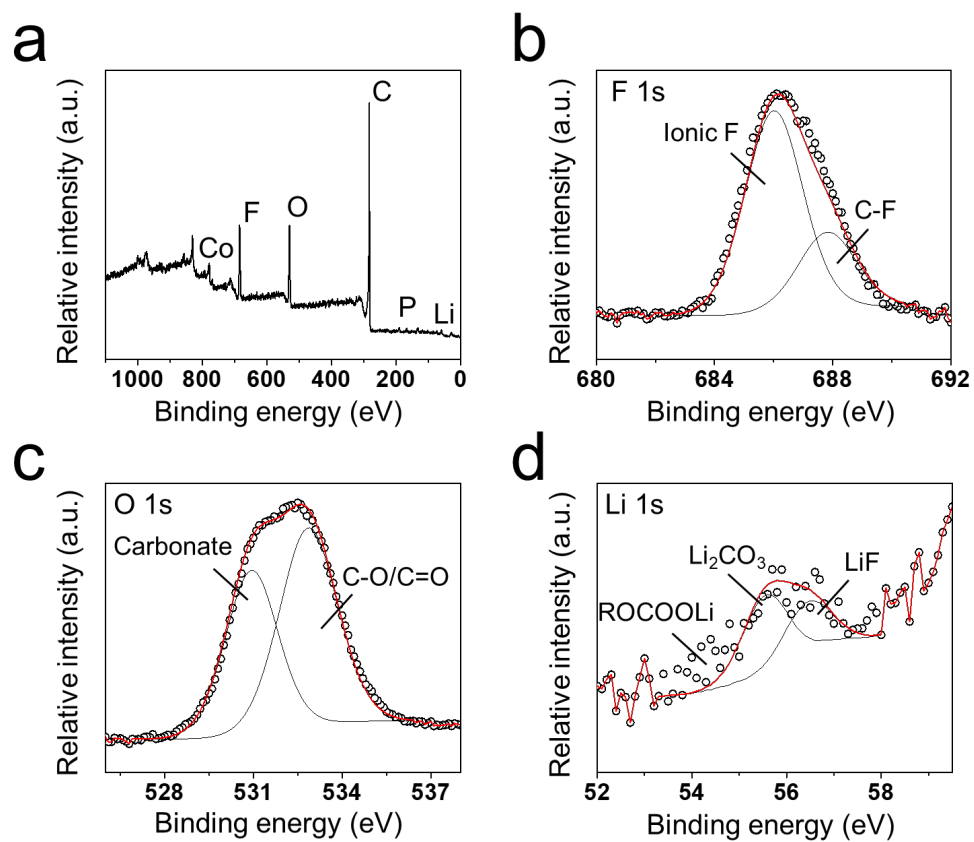


**Supplementary Fig. 1. The pH-dependent leachability of various black mass with different chemistries. a-b, BM-1. c-e, BM-2. f-h, BM-3. i-j, BM-4. k-l, BM-5. m-n, BM-6. o-q, BM-7. a, c, f, i, k, m, o, The total quantification of battery metals (*aqua regia*, 50 °C, 90 min) in various black mass materials. The error bars reflect the standard deviations from at least three individual measurements. The same below. b, d, g, j, l, n, p, pH-dependent leachability of lithium and transition metals (50 °C, 90 min) from various black mass. e, h, q, pH-dependent leachability of cobalt, nickel, manganese, and iron (50 °C, 90 min) from various black mass. AqR: *aqua regia*.**

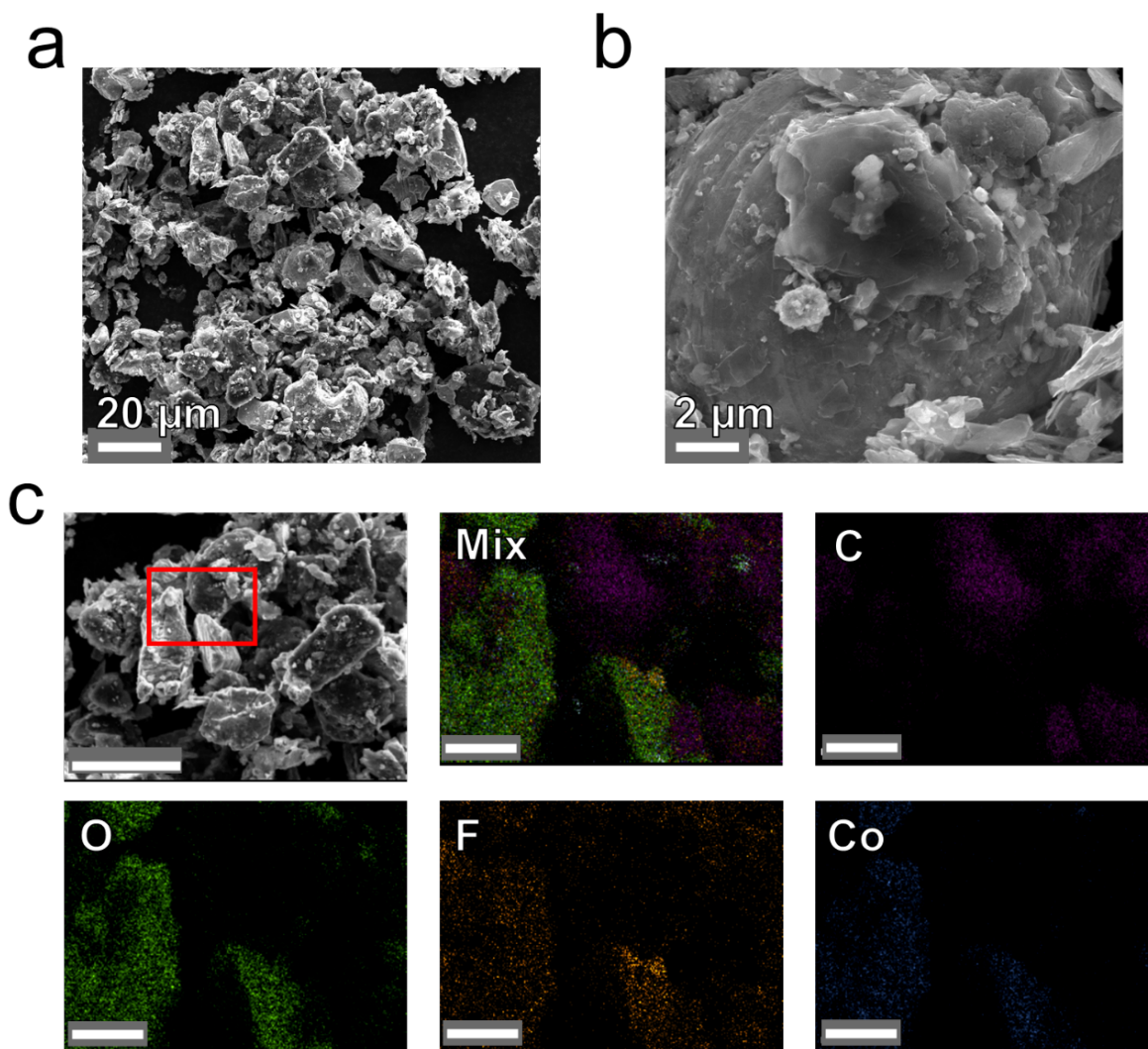




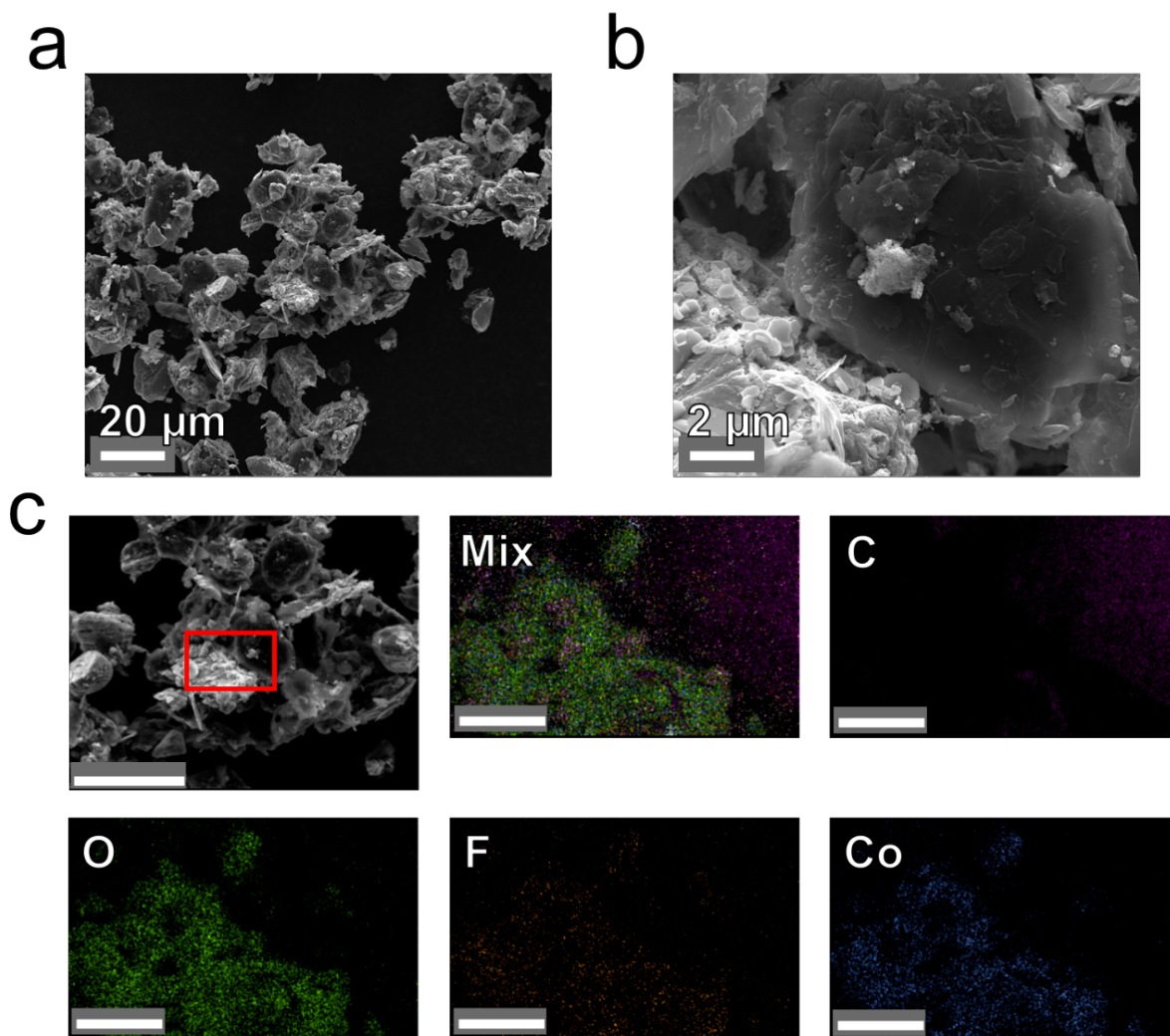
**Supplementary Fig. 2. The XRD patterns of raw black mass with distinct chemistries. a, BM-1. b, BM-2. c, BM-3. d, BM-4. e, BM-5. f, BM-6. g, BM-7. BM-7 is the mixture of the black mass, and the cathode includes oxide-type  $\text{LiCoO}_2$  and  $\text{LiNi}_{0.8}\text{Mn}_{0.1}\text{Co}_{0.1}\text{O}_2$ , as well as the phosphate-type  $\text{LiFePO}_4$ . The analyses of these XRD patterns are given and the attributions of the XRD peaks are provided atop each graph.**



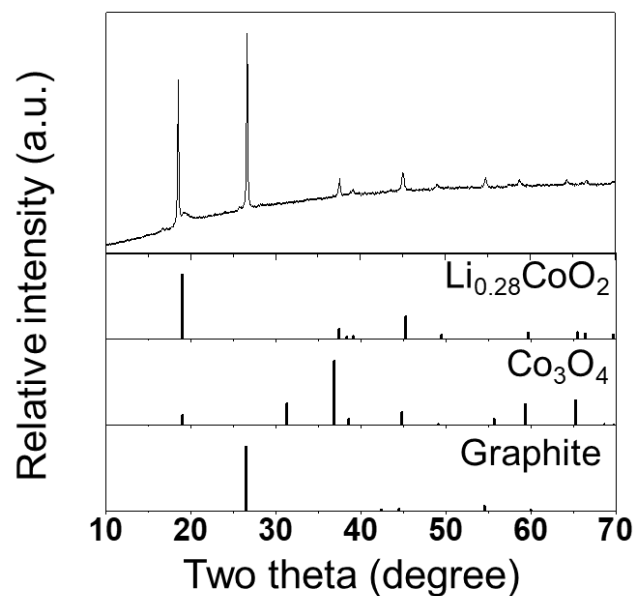
**Supplementary Fig. 3. The high-resolution elemental analysis of raw black mass BM-1. a,** The full spectrum of the black mass **BM-1. b-d,** High resolution F 1s, O 1s and Li 1s spectra of black mass **BM-1.**



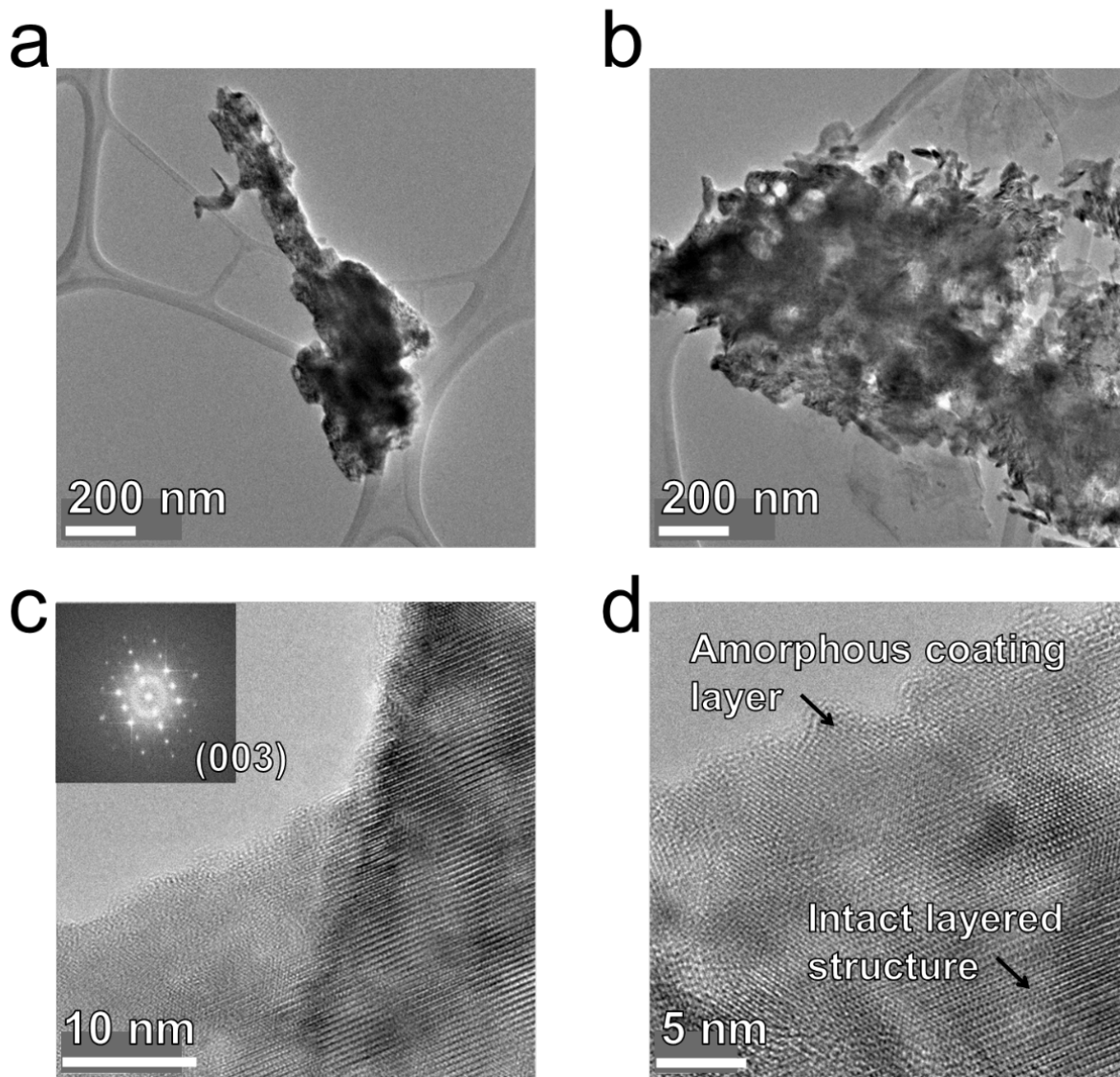
**Supplementary Fig. 4. The morphology of raw black mass BM-1. a-b,** Morphology of the raw black mass. **c,** SEM image and corresponding elemental distributions of the raw black mass BM-1. The scale bars for the SEM image and the elemental distributions are 10 μm and 2 μm, respectively. The red rectangle shows the area for elemental analysis.



**Supplementary Fig. 5. The morphology of raw black mass BM-1 after acid leaching treatment. a-b,** Morphology of the raw black mass BM-1 after acid leaching treatment (1 M, 50 °C, 24 h). **c,** SEM image and corresponding elemental distributions of the raw black mass BM-1 after acid leaching treatment. The scale bars for the SEM image and the elemental distributions are 10  $\mu\text{m}$  and 2  $\mu\text{m}$ , respectively. The red rectangle shows the area for elemental analysis.

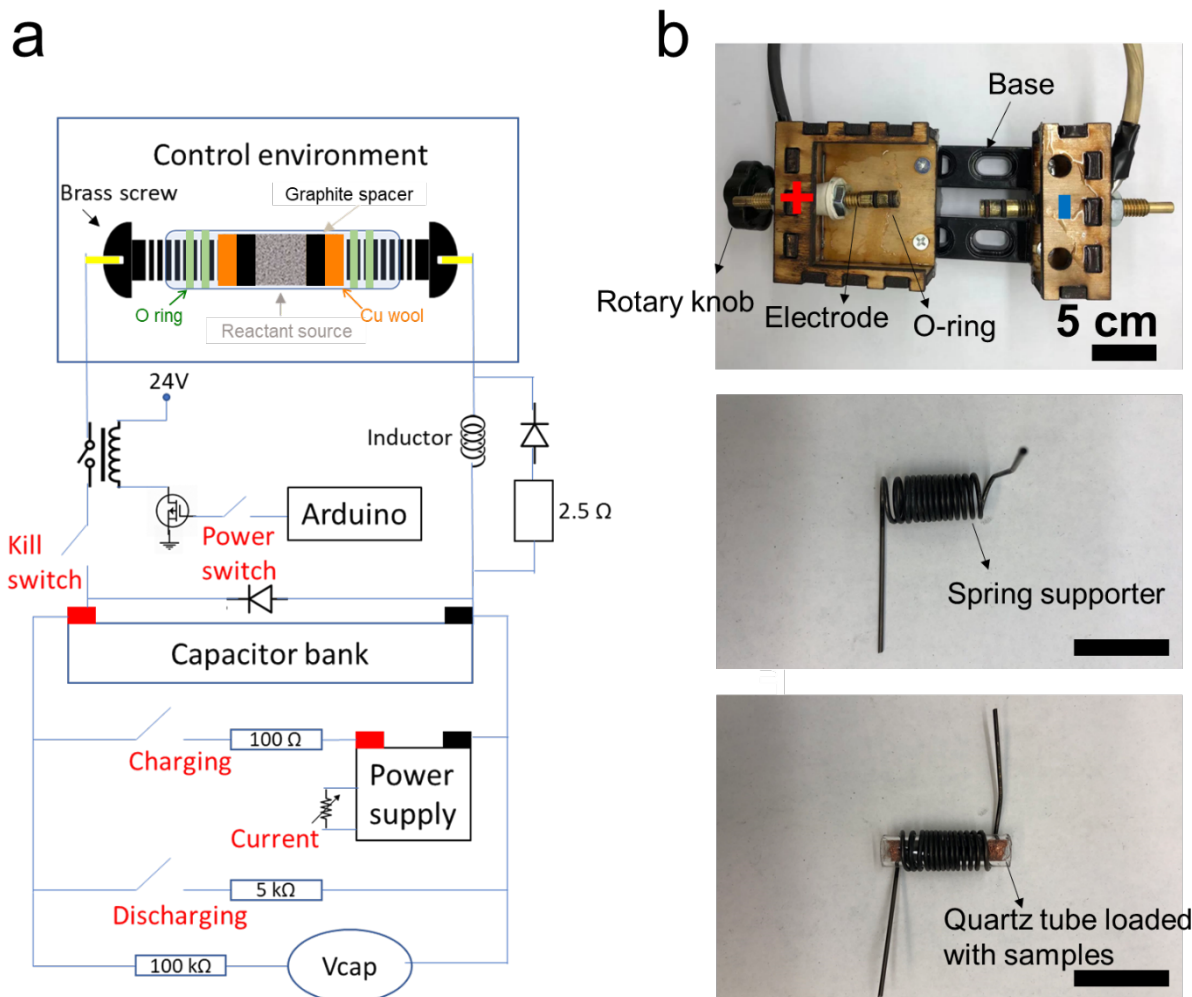


**Supplementary Fig. 6. The crystal structure of raw black mass BM-1 after acid leaching treatment.** Powder Diffraction File 00-069-0015,  $\text{Li}_{0.28}\text{CoO}_2$ . 04-022-7118,  $\text{Co}_3\text{O}_4$ . 00-056-0159, Graphite. The existence of transition metal oxides as shown from TEM images (Supplementary Fig. 7) and XRD pattern (Supplementary Fig. 6) confirms that the low leaching efficiency of lithium and transition metals with acid leaching treatment (1 M, 50 °C, 24 h) is caused by the incomplete dissolution of the cathode materials from the raw black mass.



**Supplementary Fig. 7. The crystal structure of raw black mass BM-1 after acid leaching treatment. a-b,** Microscale morphology of the raw black mass BM-1 after acid leaching treatment (1 M, 50 °C, 24 h), showing the existence of the unreacted transition metal oxide cathode materials. **c-d,** High-resolution crystal structures of the unreacted cathode materials, reflecting the coexistence of the intact layer structure and the amorphous coating layer, which is the compact SEI protective layer. The inset of the Supplementary Fig. 7c demonstrates the FFT result of the corresponding HR-TEM images.

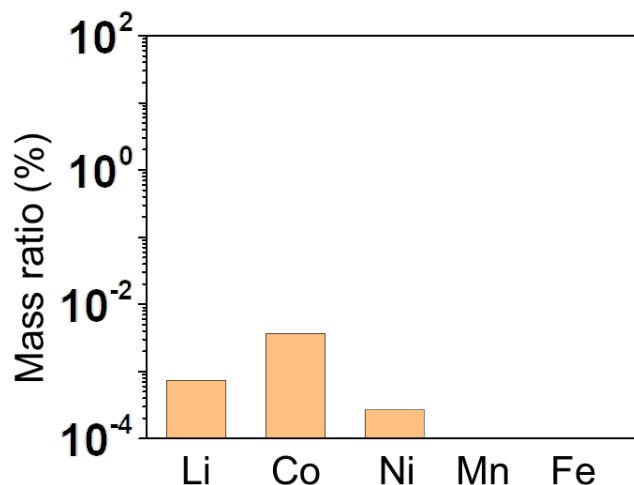
## Flash Joule Heating Setup



**Supplementary Fig. 8. The scheme of FJH system.** a, Electrical schematic of the FJH system. b, Photographs of the sealable FJH reaction box, the spring protector, and the quartz tube loaded with samples and surrounded by the spring supporter, respectively (From top to bottom). The scale bars in the photos are 5 cm.

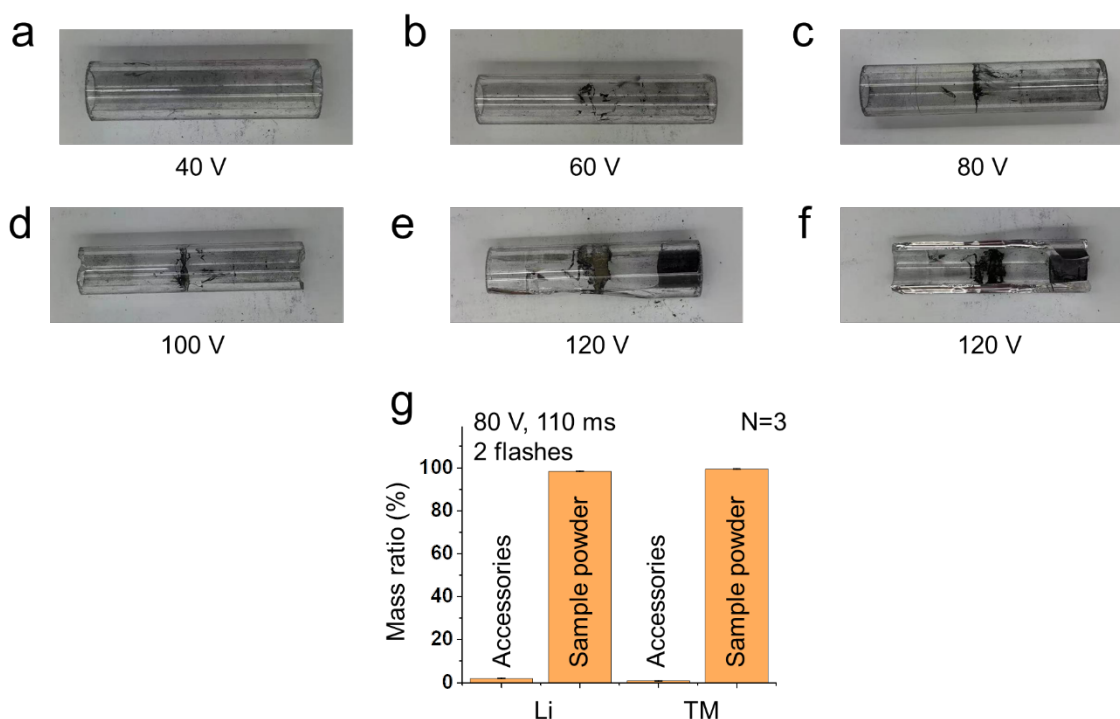
10 aluminum electrolytic capacitors (450V, 6 mF, Mouser #80-PEH200YX460BQU2) with a total capacitance of 60 mF were used for charging in the small batch (~200 mg per batch). The brass screw electrodes were modified with two grooves at each side for the O-rings, which fit

snugly into the quartz tube. The introduction of the O-rings alleviated the loss of the battery metals from the system during the flash process. To enhance the strength and avoid the explosion of the reaction tube, a spring supporter was used as shown in Supplementary Fig. 8b. An Arduino controller relay with programmable millisecond-level delay time is used to control the discharge time, and the electric energy is provided by the capacitor bank. Safety glasses designed for welding are generally suitable and recommended during the flash reaction because they effectively block infrared as well as ultraviolet light. More safety guidelines can be found in Supplementary Note 2 (Ref. 3). The FJH reaction box was shown in Supplementary Fig. 8b, and it was mainly comprised of a metal base, a rotary knob and two electrodes connected with wires in the circuit. By rotating the knob of the FJH reaction box, the distance between two electrodes can be adjusted. The prepared sample is placed between the two electrodes and compressed until the desired conductivity is reached. See the Experimental Section for details.

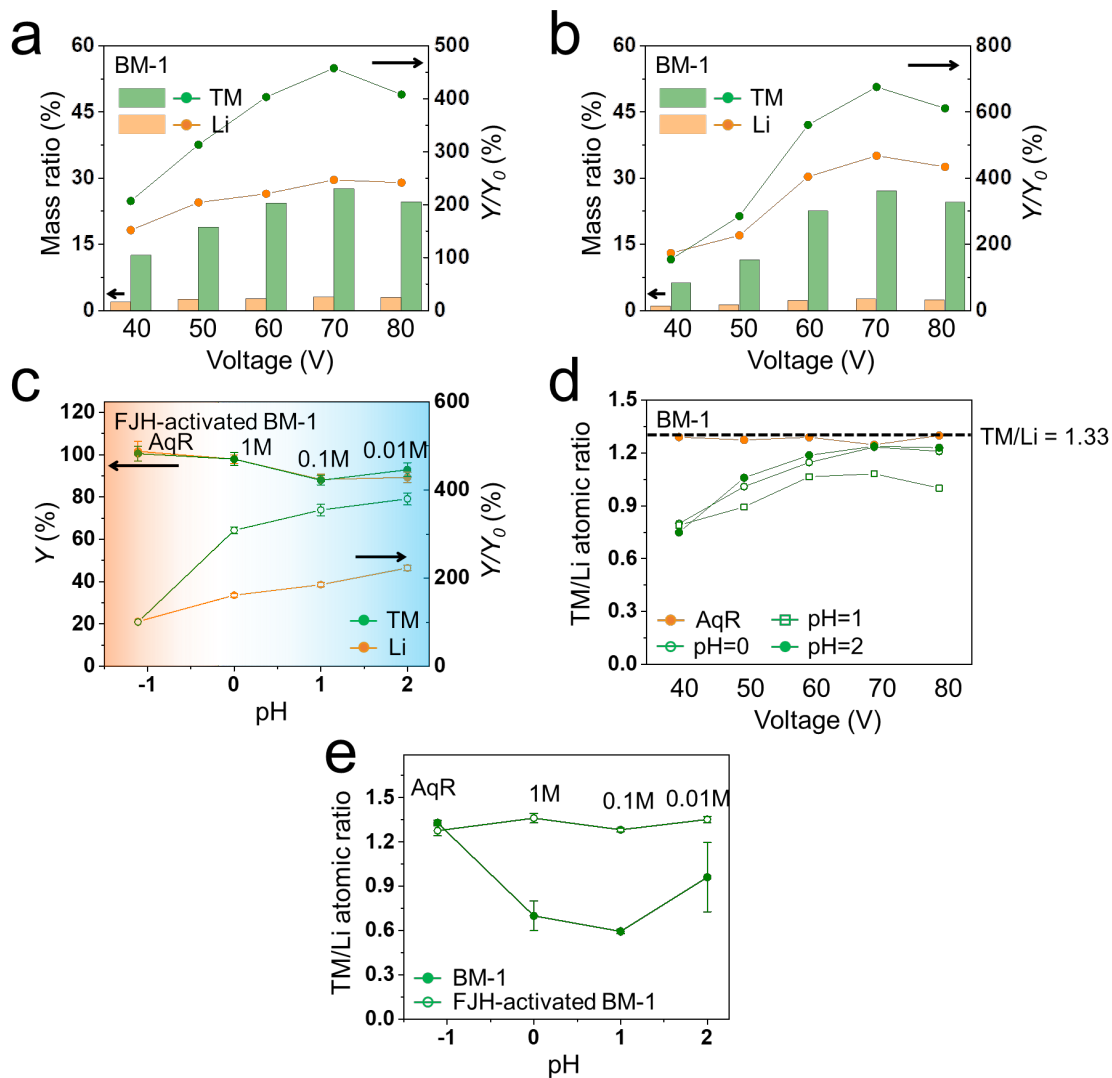


**Supplementary Fig. 9. The HCl-extractable battery metals from the accessories.** Quartz tube, copper wools, and graphite spacers were included in the blank test. The same acid leaching

procedure (1 M, 50 °C, 90 min) is applied. Compared to the mass ratios of battery metals in the black mass from spent lithium-ion batteries, the mass ratio in the accessories is 1000× to 10000× lower, which would not affect the measurement of the samples.

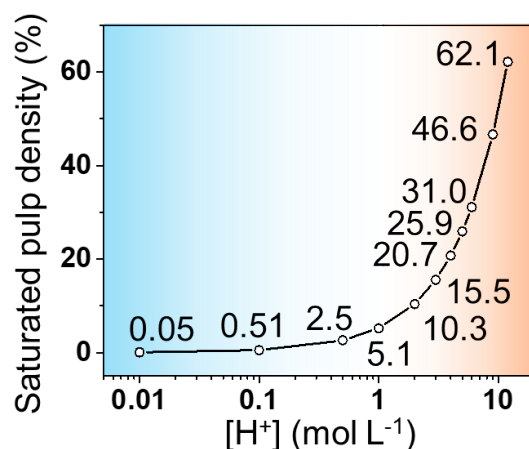


**Supplementary Fig. 10. The distribution of the battery metals after FJH activation under different voltages.** a-f, The photograph of quartz tubes after the FJH activation with various flash voltages. g, The distribution of battery metals from the FJH-activated BM-1 sample powder and the accessories (tube, graphite spacers, and copper wools). The error bars reflect the standard deviations from three individual measurements. ~98.3% of Li and ~99.3% of transition metals were remained within the FJH-activated BM-1. There was a very small standard deviations for the element distribution.



**Supplementary Fig. 11. The pH-dependent leachability of FJH-activated BM-1. a,** Relationship between the HCl-extractable battery metal contents (0.1 M, 50 °C, 90 min) from FJH-activated BM-1, increase in recovery yield ( $Y/Y_0$ ), and the FJH voltages. The dashed line represents  $Y/Y_0 = 100\%$ , indicating the recovery result of BM-1. The same below. **b,** Relationship between the HCl-extractable battery metal contents (0.01 M, 50 °C, 90 min) from FJH-activated BM-1, increase in recovery yield ( $Y/Y_0$ ), and the FJH voltages. **c,** pH-dependent leachability ( $Y$ ) of lithium and transition metals (50 °C) and increase in recovery yield ( $Y/Y_0$ ) from FJH activated BM-1. To compare the leaching results near the equilibrium, the leaching

duration for 0.1 M and 0.01 M HCl are 24 h and 168 h, respectively in Supplementary Fig. 11c and 11e. **d**, Relationship between atomic ratio of transition metals from FJH activated BM-1 and the FJH voltages. The dashed line represents the atomic ratio of BM-1 as determined by *aqua regia*. **e**, pH-dependent atomic ratio of transition metals to lithium from raw and FJH-activated BM-1.



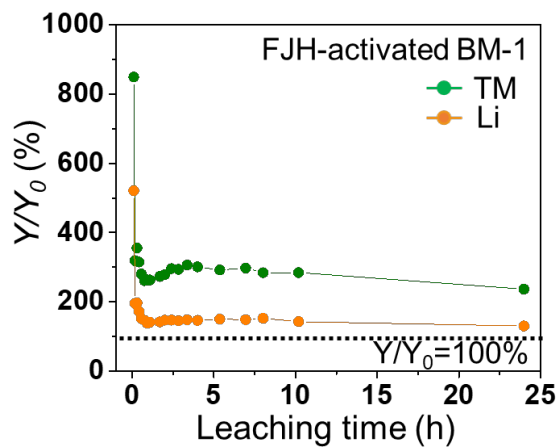
**Supplementary Fig. 12. The relationship between saturated pulp density and the concentration of [H<sup>+</sup>] for the leaching solutions.**

The pulp density is related to the acid concentration and the saturated pulp density is calculated based on the stoichiometric relationships between battery metals and the [H<sup>+</sup>] as determined below,

$$n[Li^+] + 2 \times n[TM^{2+}] + 3 \times n[TM^{3+}] = n[H^+] \quad (16)$$

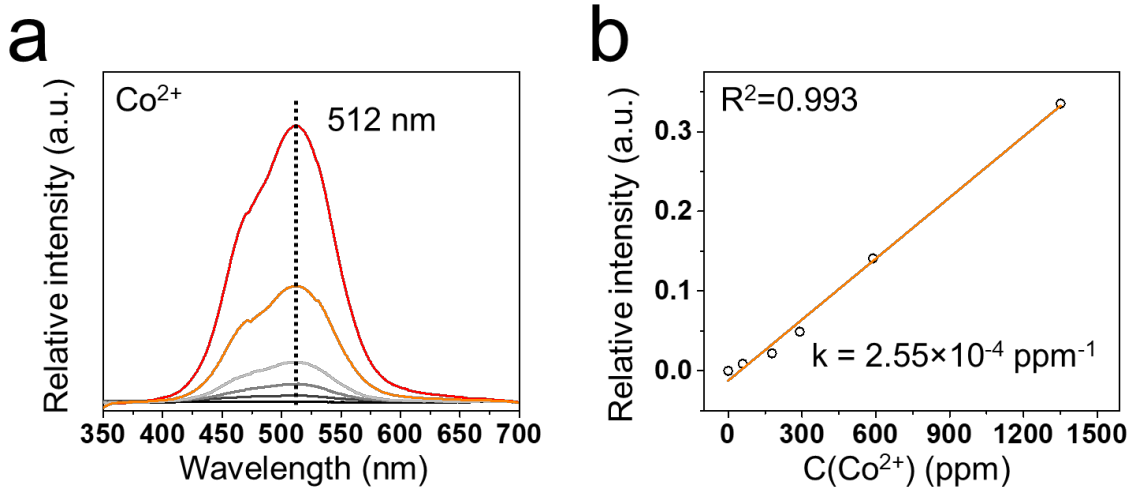
Here,  $n[Li^+]$ ,  $n[TM^{2+}]$ ,  $n[TM^{3+}]$ , and  $n[H^+]$  mean the molar amounts of Li<sup>+</sup>, divalent transition metal ions TM<sup>2+</sup>, trivalent transition metal ions TM<sup>3+</sup>, and H<sup>+</sup>, respectively. The high valence (>3) is not thermodynamically favorable to form under the leaching condition, therefore only divalent and trivalent transition metal ions are considered above. The relationship between

saturated pulp density and the acid concentration is shown in Supplementary Fig. 12. The amounts of battery metals of black mass from this work are used to calculate the amounts of  $H^+$ .

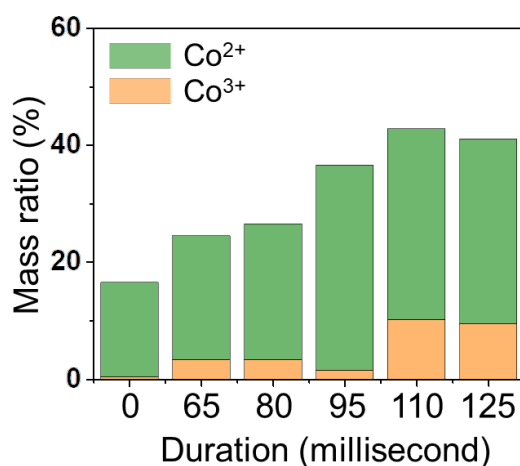


**Supplementary Fig. 13. The kinetic leaching results.** Increase in recovery yield ( $Y/Y_0$ ) of the FJH-activated BM-1 over the raw black mass BM-1 with 1.0 M HCl solution (50 °C) after different leaching durations.

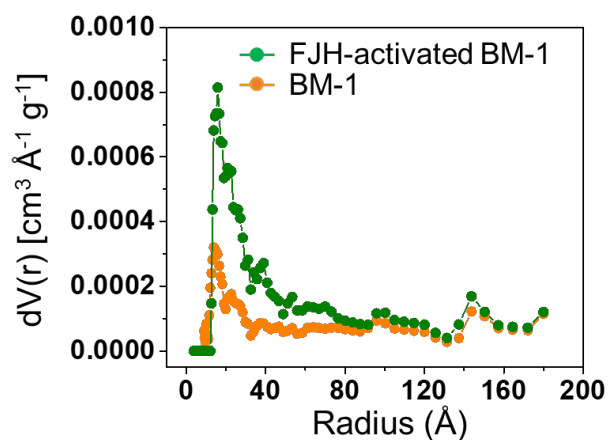
#### Determination of $Co^{2+}$ and $Co^{3+}$ in the leachates



**Supplementary Fig. 14. The calibration of [Co<sup>2+</sup>] in the solutions.** **a**, The UV-vis absorbance spectra of various standard solutions with the [Co<sup>2+</sup>] from 0 to 0.020 mol L<sup>-1</sup> (blank solution, 0.001, 0.002, 0.005, 0.010, 0.020 mol L<sup>-1</sup>). **b**, The calibration curve of [Co<sup>2+</sup>] in the standard solutions followed the Beer–Lambert law.  $R^2$  is calculated based on linear regression equation and  $k$  is the slope of the fitting line. To enhance the absorbance, NH<sub>4</sub>SCN is added to the solution to form the coordination complex with Co<sup>2+</sup> (ref. 12).

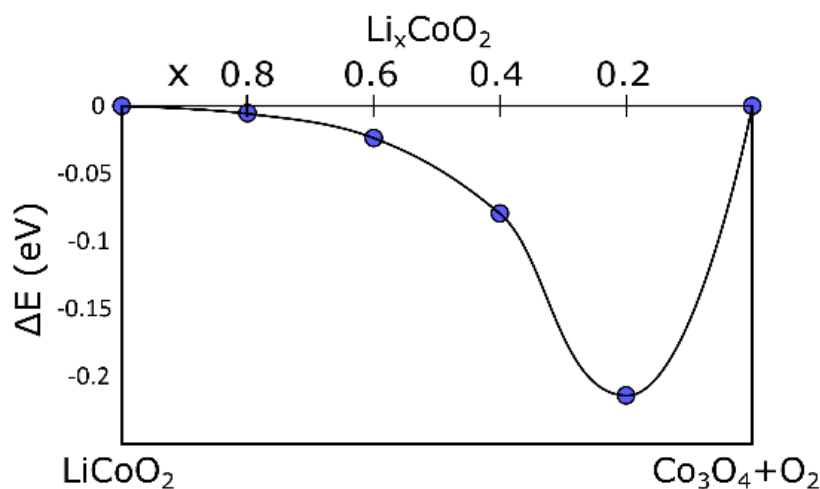


**Supplementary Fig. 15. Relationship between the concentration of Co<sup>2+</sup>, Co<sup>3+</sup> from the HCl-extractable battery metal contents (1 M, 50 °C, 90 min) for FJH-activated BM-1 and the flash durations.**



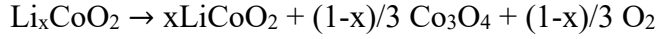
Supplementary Fig. 16. The pore size distribution of the raw black mass BM-1 and FJH-activated BM-1.

#### First principle simulations of FJH activation of black mass



Supplementary Fig. 17 Energy preference towards phase segregation of partially delithiated lithium cobalt oxide.

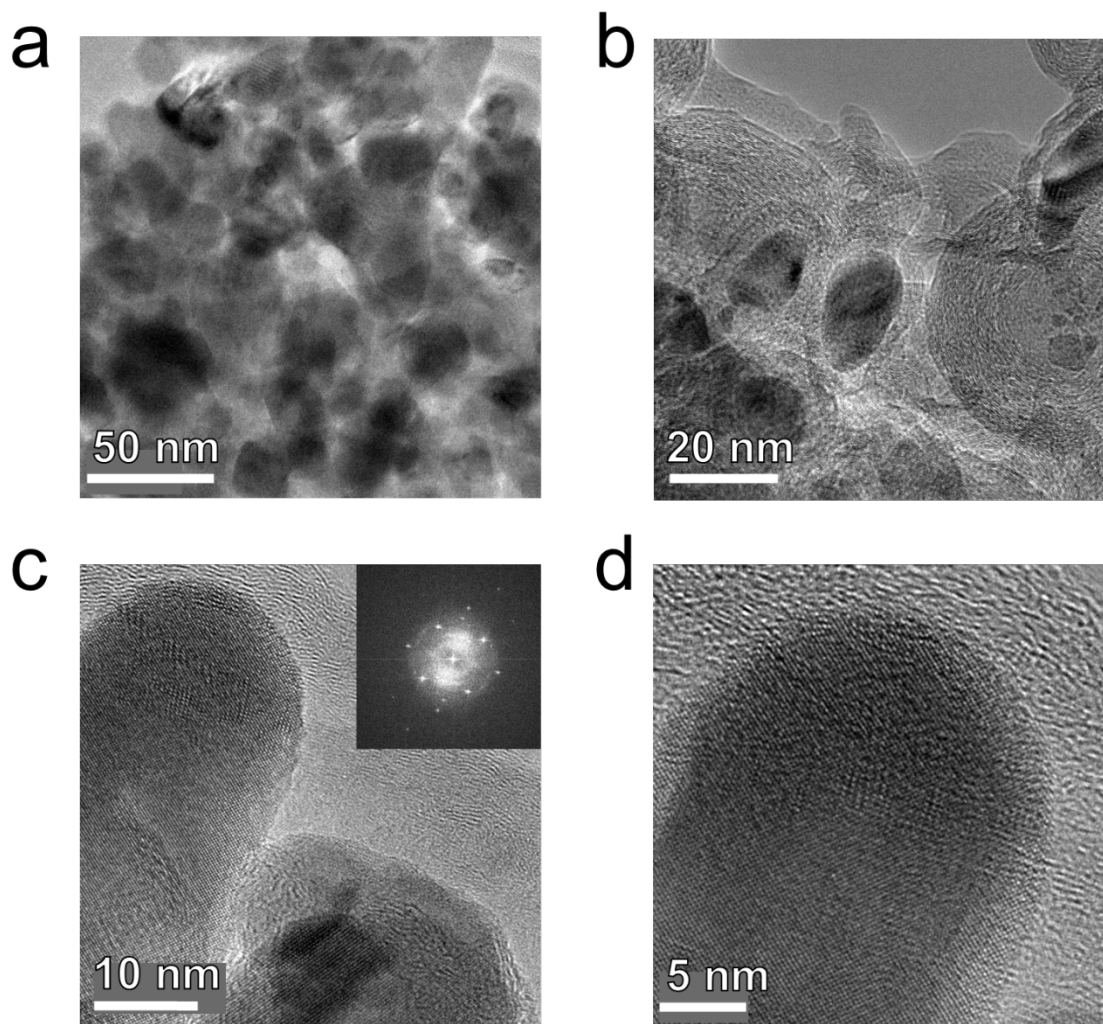
First principle calculations allowed us to demonstrate a possible route for FJH activation process of partially delithiated  $\text{Li}_x\text{CoO}_2$  through phase segregation to form the crystalline  $\text{LiCoO}_2$ ,  $\text{Co}_3\text{O}_4$  and release of  $\text{O}_2$  gas:<sup>13</sup>



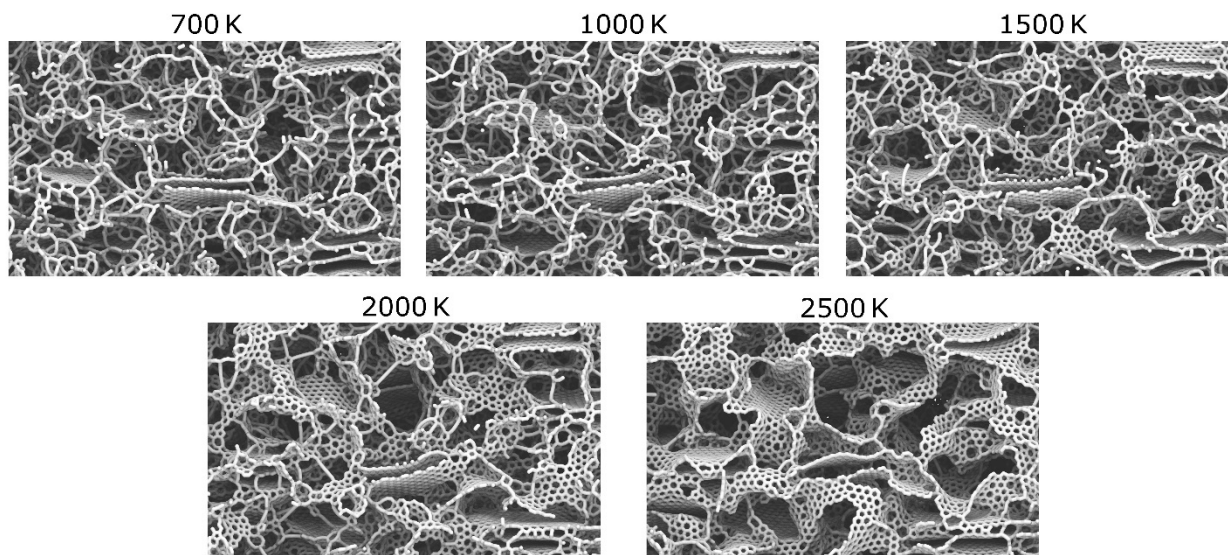
Reaction energy ( $\Delta E$ ) is calculated as,

$$\Delta E = E(\text{LiCoO}_2) + E(\text{Co}_3\text{O}_4) + E(\text{O}_2) - E(\text{Li}_x\text{CoO}_2) \quad (17)$$

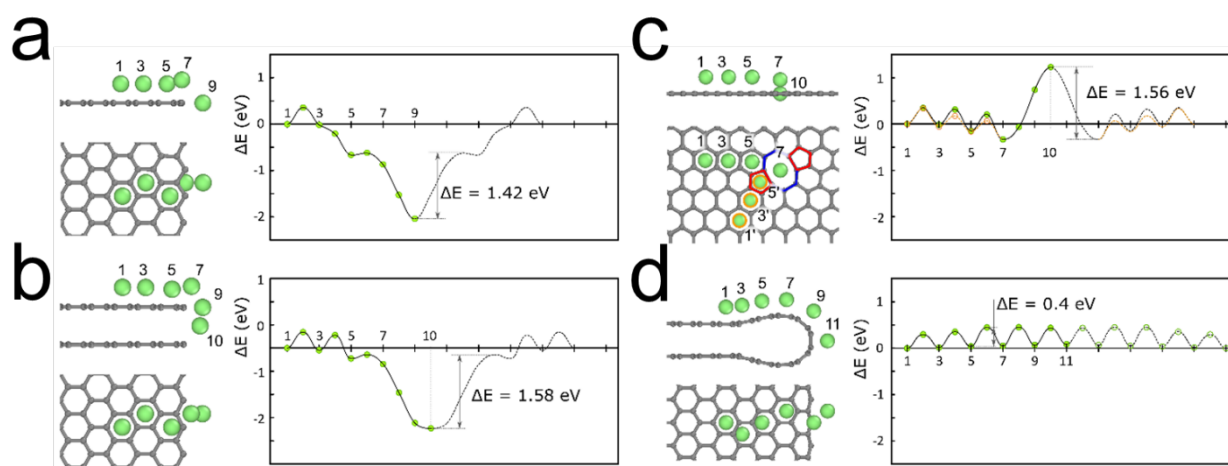
Reaction energy ( $\Delta E$ ) for various values of  $x$  is plotted on Supplementary Fig. 17 and indicates energetic preference towards phase segregation. It is interesting to note that at low-to-moderate delithiation levels, energy preference towards segregation is minimal. The crystalline  $\text{LiCoO}_2$  and  $\text{Co}_3\text{O}_4$  can further react with carbonaceous components, like graphite, and conductive carbon to form simple metal and metal oxides as demonstrated in the Ellingham diagram (Fig. 1g, Supplementary Table 3). These compounds show enhanced thermodynamic and kinetic leaching performance compared with the partially delithiated lithium cobalt oxide as discussed in Figs. 2-3.



**Supplementary Fig. 18. The crystal structure of the FJH-activated BM-1. a-b,** Morphology of FJH-activated BM-1. **c-d,** High-resolution TEM images of FJH-activated BM-1. The inset shows the FFT patterns of the FJH-activated BM-1.

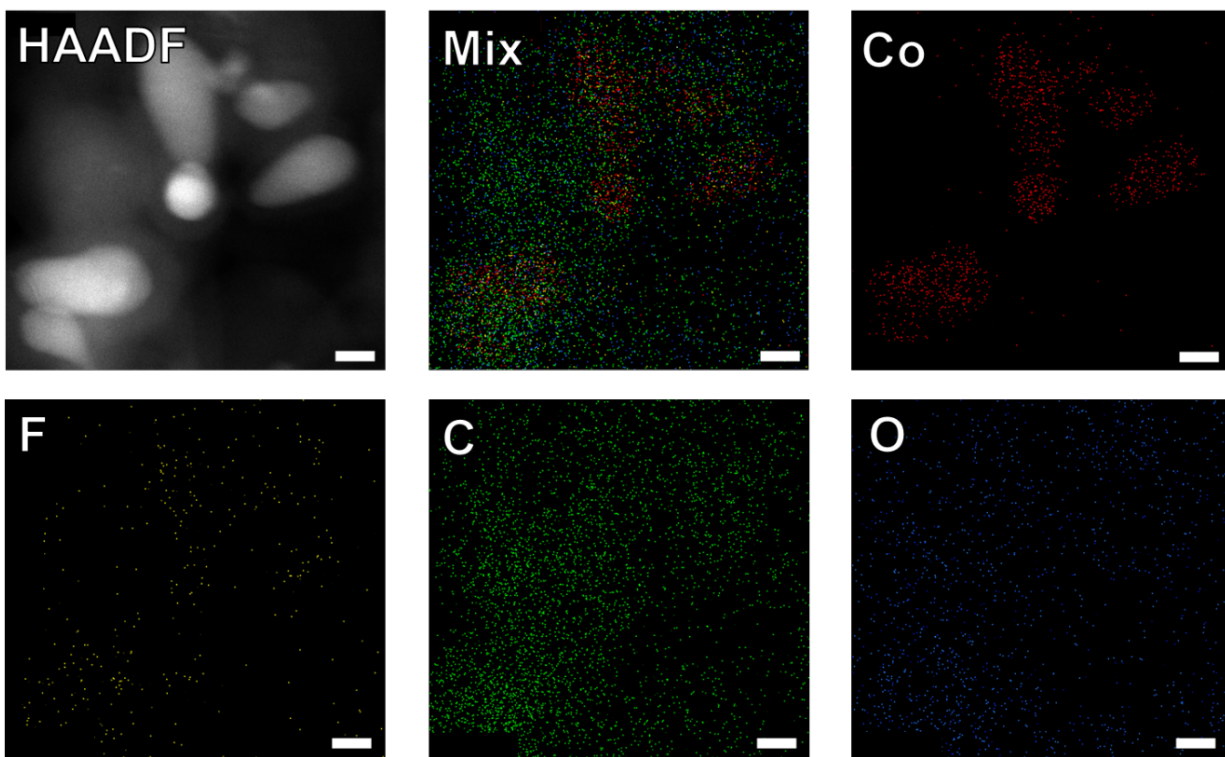


**Supplementary Fig. 19. Carbon crust configuration after annealing at various temperatures for 9 ns.**

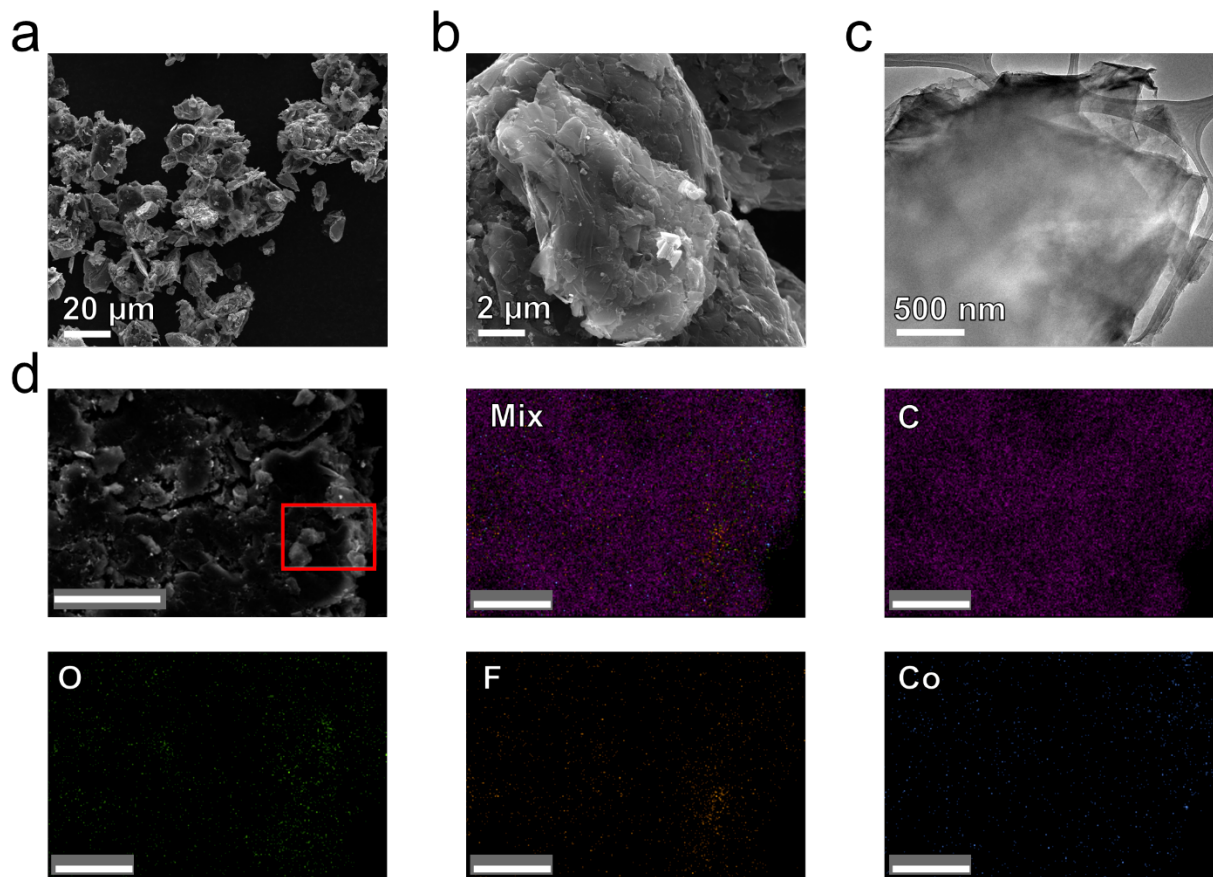


**Supplementary Fig. 20 Diffusion barrier for  $\text{Li}^+$  on various features within amorphous carbon shell.** **a**, Unpassivated single-layer graphene edge; **b**, unpassivated double-layer graphene edge; **c**, over the reconstructed di-vacancy forming 5-8-5 defect (largest barrier corresponds to diffusion through the 8-ring defect to the other side of the plane, steps 7-10); **d**,

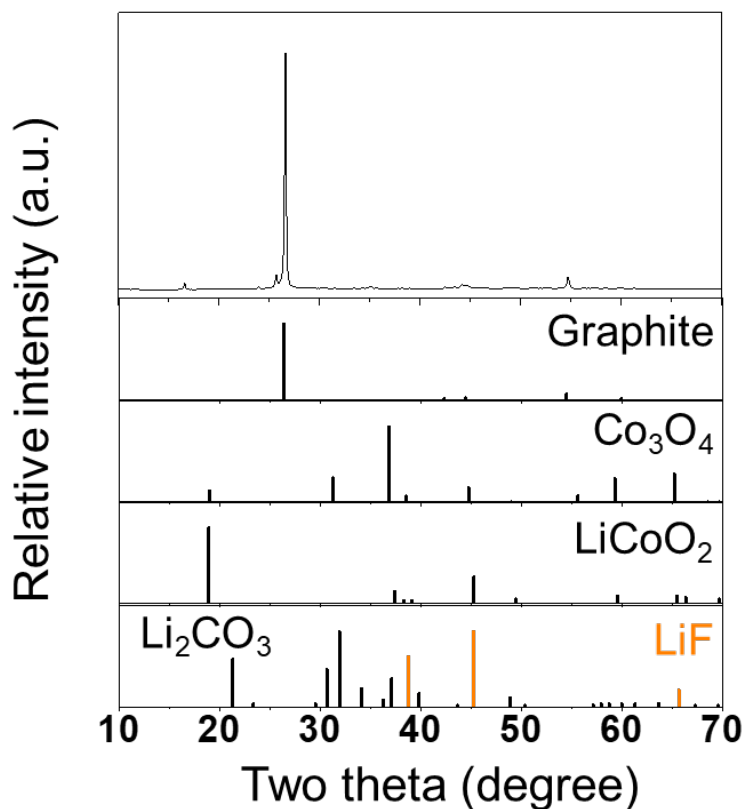
diffusion over the reconstructed edge of double-layer graphene shows barrier almost identical to that for diffusion on the plane graphene  $\sim 0.34$  eV.



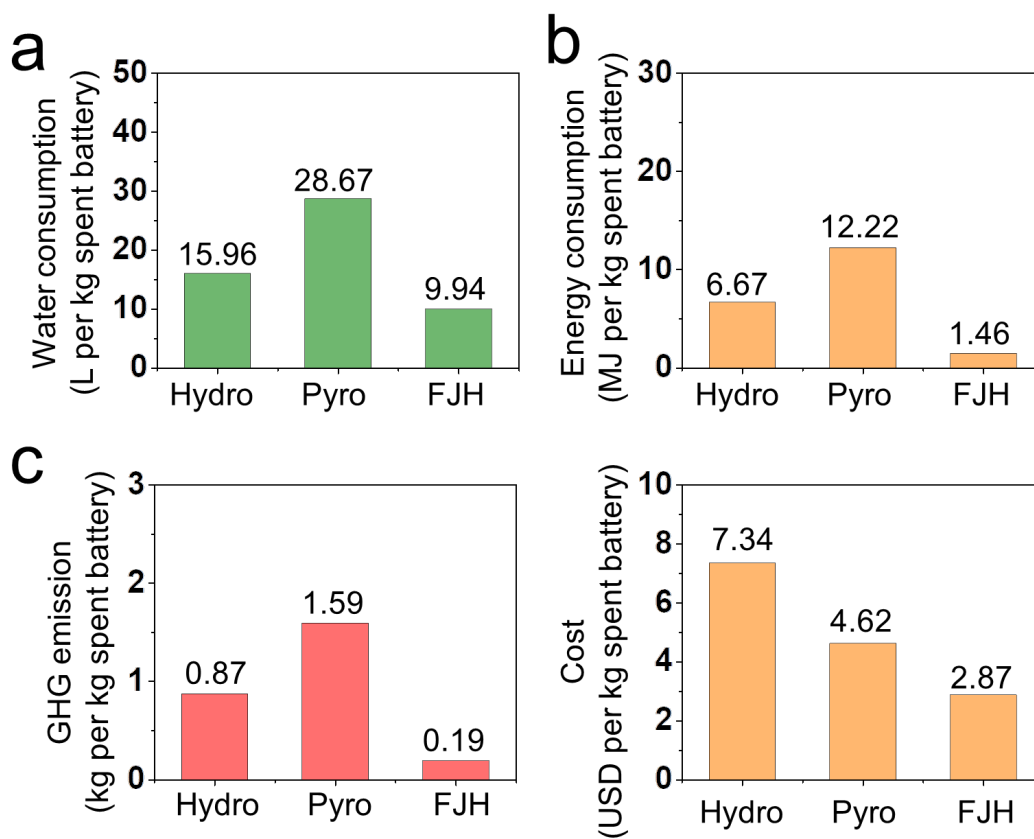
**Supplementary Fig. 21.** The energy dispersive analysis element mapping of the **FJH-activated BM-1**. The as-formed primary particles are the reduced transition metal since the dispersive distribution of oxygen and fluorine around the particles, which are different from the metal.



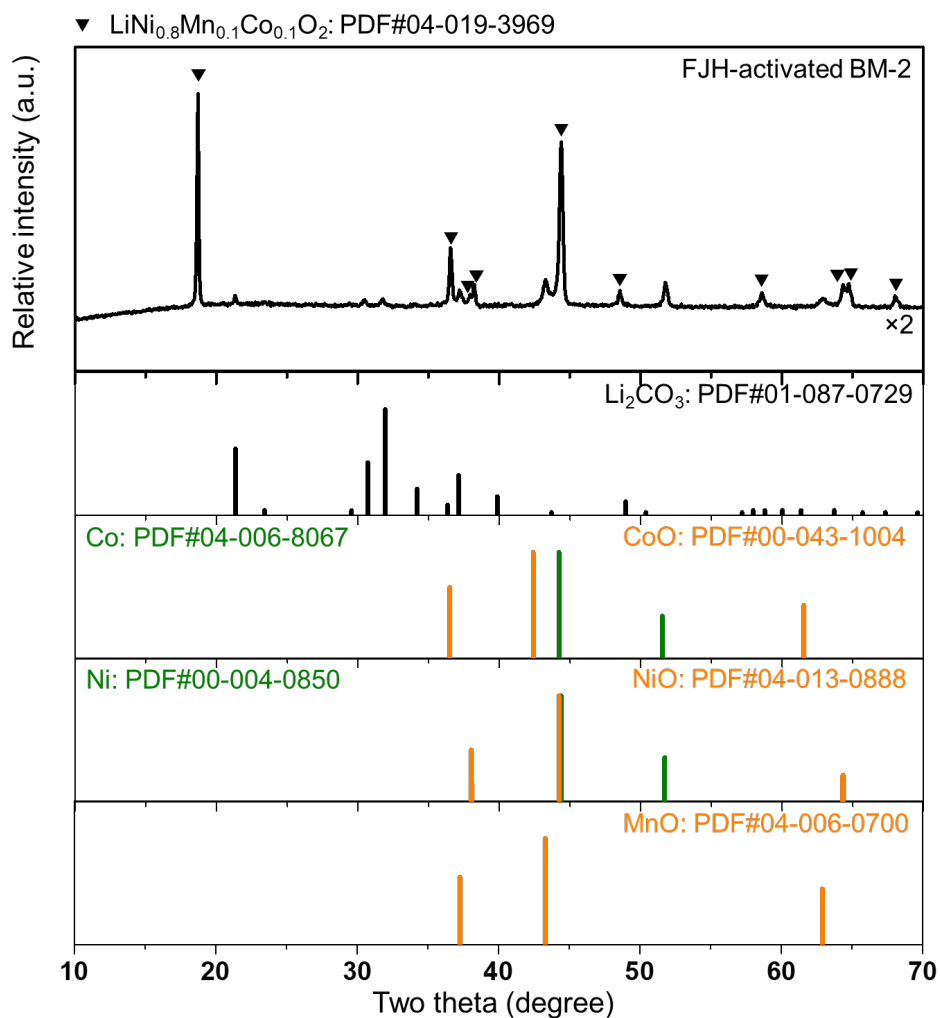
**Supplementary Fig. 22. The morphology of the FJH-activated BM-1 after the acid wash. a-**  
**b,** Morphology of the FJH-activated BM-1 after acid leaching treatment (1 M, 50 °C). **c,**  
Morphology of a single FJH-activated BM-1 particle after acid leaching treatment. **d,** SEM  
image and corresponding elemental distributions of the FJH-activated BM-1 after acid leaching  
treatment. The scale bars for the SEM image and the elemental distributions are 50 μm and 10  
μm, respectively. The red rectangle shows the area for elemental analysis.



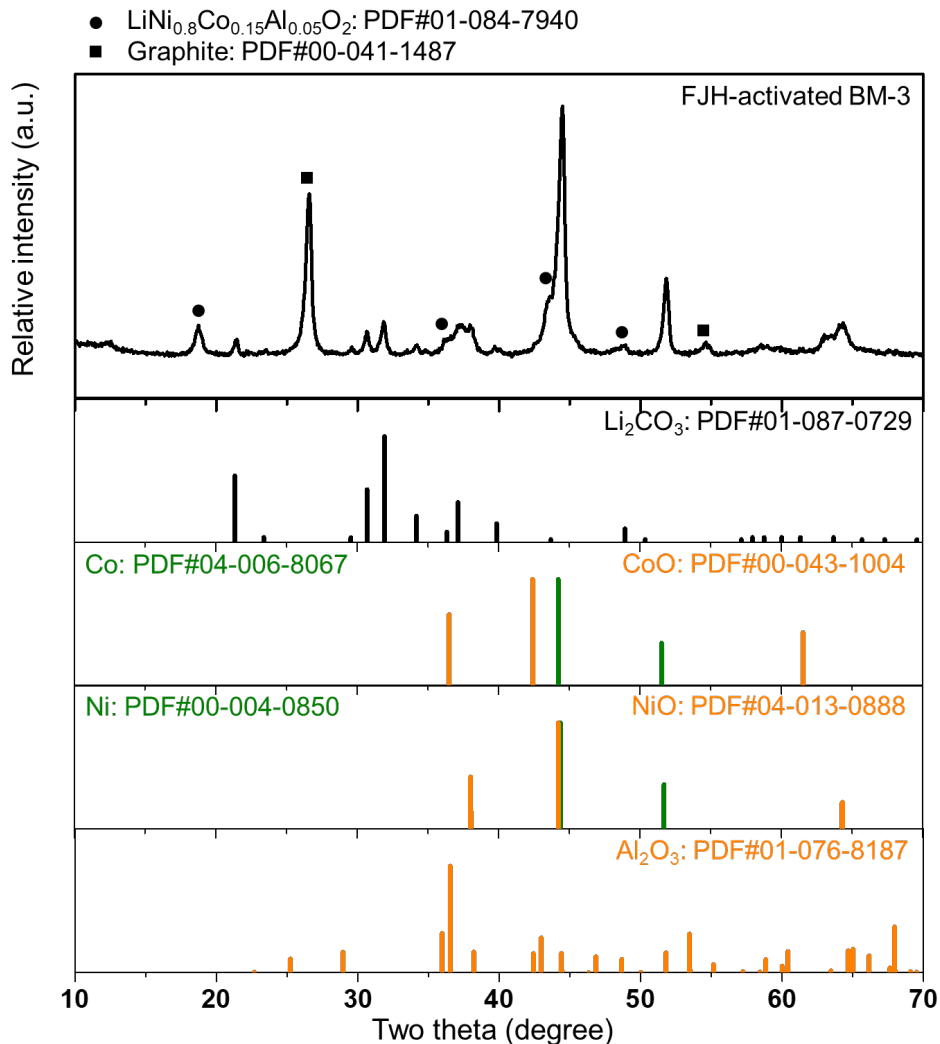
**Supplementary Fig. 23. The crystal structure of the FJH-activated BM-1 after the acid wash.** Powder Diffraction File 00-056-0159, Graphite. 04-020-7500,  $\text{Co}_3\text{O}_4$ . 04-007-3587, LiF. 04-010-5115,  $\text{Li}_2\text{CO}_3$ . 00-062-0420,  $\text{LiCoO}_2$ . The dominate diffraction peaks are from graphite, and there are no obvious diffraction peaks from transition metal oxides or the simple salts which are the decomposed products as explained in Fig. 3. This result indicates that FJH activation and dilute acid treatment can effectively be applied to recycle the battery metals from black mass.



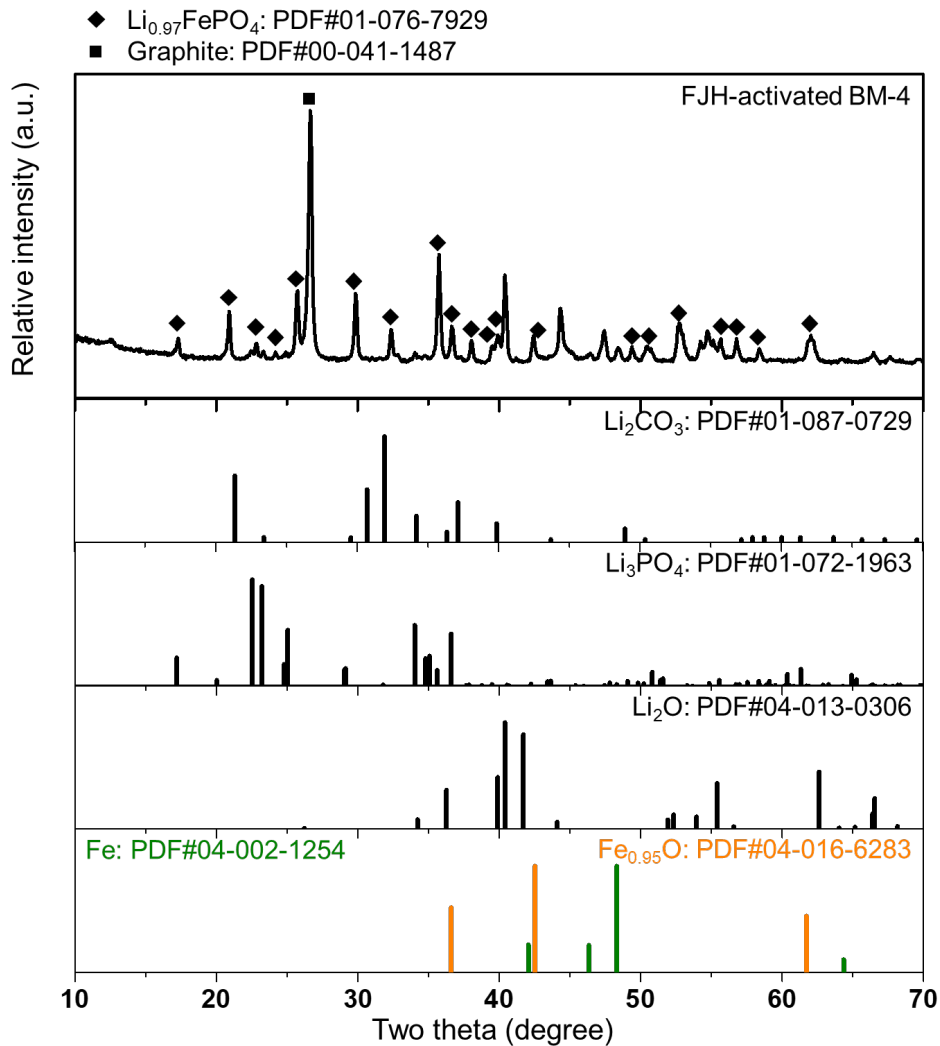
**Supplementary Fig. 24. Economic and environmental analysis of the FJH activation recycling process.** Water consumption, energy consumption, greenhouse gas emission and cost in treating 1 kg of spent batteries. The production of new cathode materials is not considered in this part. Hydro: hydrometallurgical method. Pyro: Pyrometallurgical method. FJH: Flash Joule heating activation recycling method.



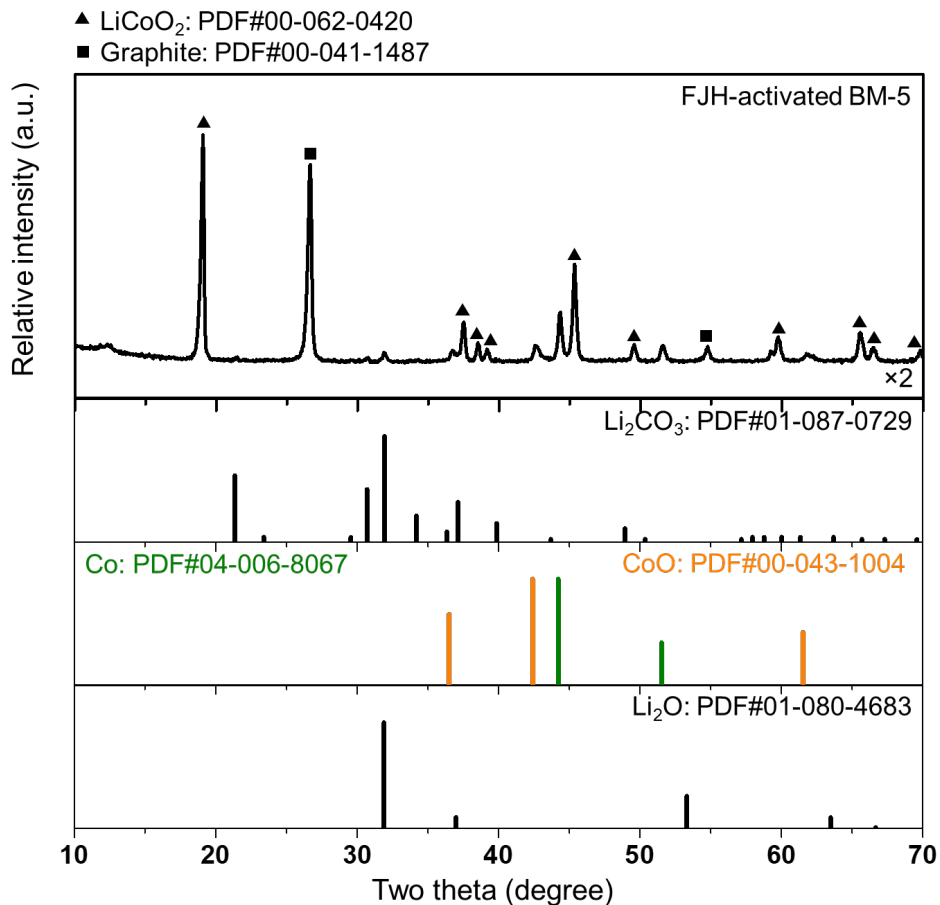
**Supplementary Fig. 25. The crystal structure of various FJH-activated black mass materials with distinct compositions.** FJH-activated BM-2 is shown here. The graph is magnified twice to compare with the raw BM-2 as shown in Supplementary Fig. 2. The relative peak intensities of the  $\text{LiNi}_{0.8}\text{Mn}_{0.1}\text{Co}_{0.1}\text{O}_2$  decrease, which indicates the decomposition and conversion of the cathode materials. The formation of simple salts, such as  $\text{Li}_2\text{CO}_3$ , simple oxides, such as  $\text{MnO}$ , and reduced metals  $\text{Co}$  and  $\text{Ni}$  can be seen after the FJH activation recycling of the black mass BM-2.



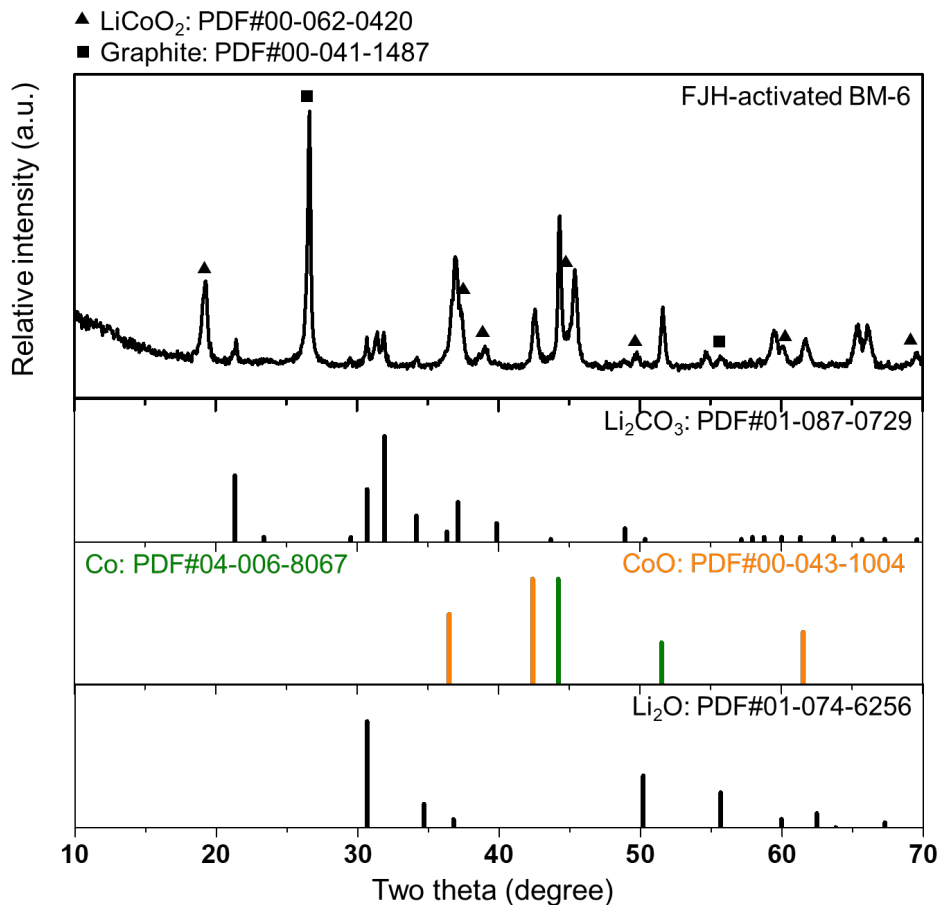
**Supplementary Fig. 26. The crystal structure of various FJH-activated black mass materials with distinct compositions.** FJH-activated BM-3 is shown here. The relative peak intensities of the  $\text{LiNi}_{0.8}\text{Co}_{0.15}\text{Al}_{0.05}\text{O}_2$  decrease, which indicates the thermal decomposition and conversion of the cathode materials. The formation of simple salts, such as  $\text{Li}_2\text{CO}_3$ , simple oxides, such as NiO and  $\text{Al}_2\text{O}_3$ , and reduced metals Co and Ni can be seen after the FJH activation recycling of the black mass BM-3.



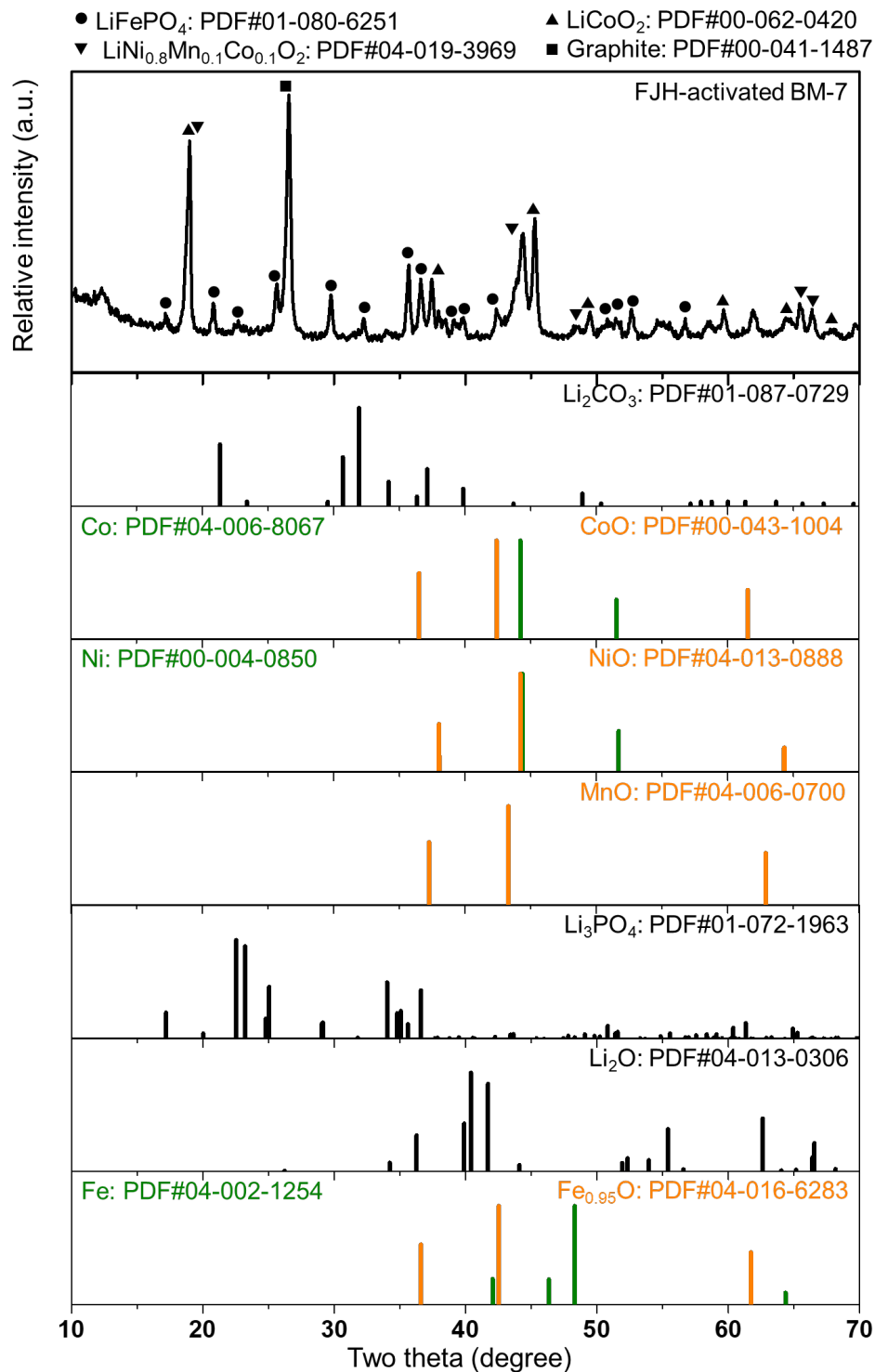
**Supplementary Fig. 27. The crystal structure of various FJH-activated black mass materials with distinct compositions.** FJH-activated BM-4 is shown here. The relative peak intensities of the  $\text{LiFePO}_4$  decrease, which indicates the thermal decomposition and conversion of the cathode materials. The formation of simple salts, such as  $\text{Li}_3\text{PO}_4$ , simple oxides, such as  $\text{Li}_2\text{O}$  and  $\text{Fe}_{0.95}\text{O}$ , and reduced metals Fe can be seen after the FJH activation recycling of the black mass BM-4.



**Supplementary Fig. 28. The crystal structure of various FJH-activated black mass materials with distinct compositions.** FJH-activated BM-5 is shown here. The relative peak intensities of the HT-LiCoO<sub>2</sub> decrease, which indicates the thermal decomposition and conversion of the cathode materials. The formation of simple salts, such as Li<sub>2</sub>CO<sub>3</sub>, simple oxides, such as Li<sub>2</sub>O and CoO, and reduced metals Co can be seen after the FJH activation recycling of the black mass BM-5.

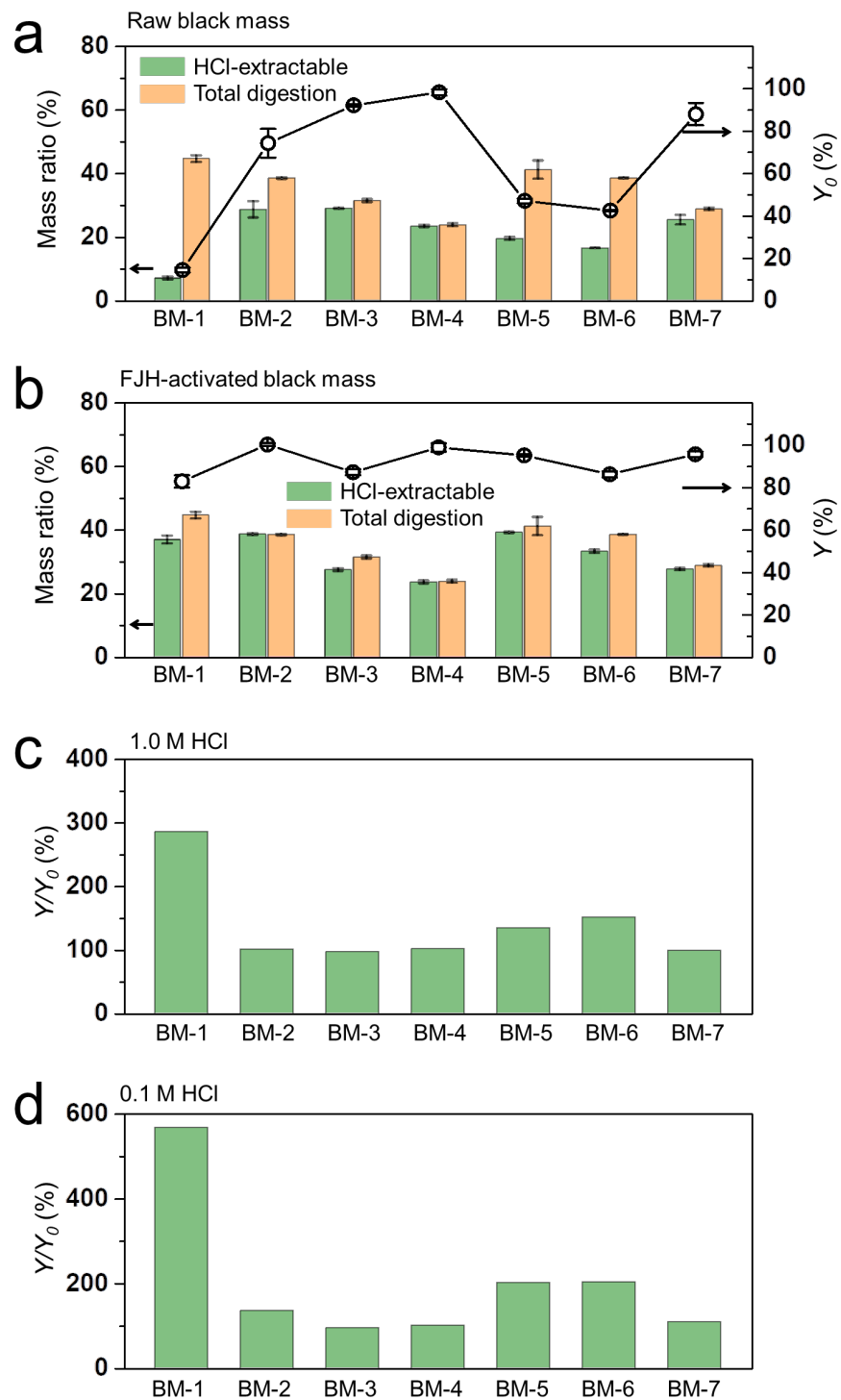


**Supplementary Fig. 29. The crystal structure of various FJH-activated black mass materials with distinct compositions.** FJH-activated BM-6 is shown here. The relative peak intensities of the LT-LiCoO<sub>2</sub> decrease, which indicates the thermal decomposition and conversion of the cathode materials. The formation of simple salts, such as Li<sub>2</sub>CO<sub>3</sub>, simple oxides, such as Li<sub>2</sub>O and CoO, and reduced metals Co can be seen after the FJH activation recycling of the black mass BM-6.



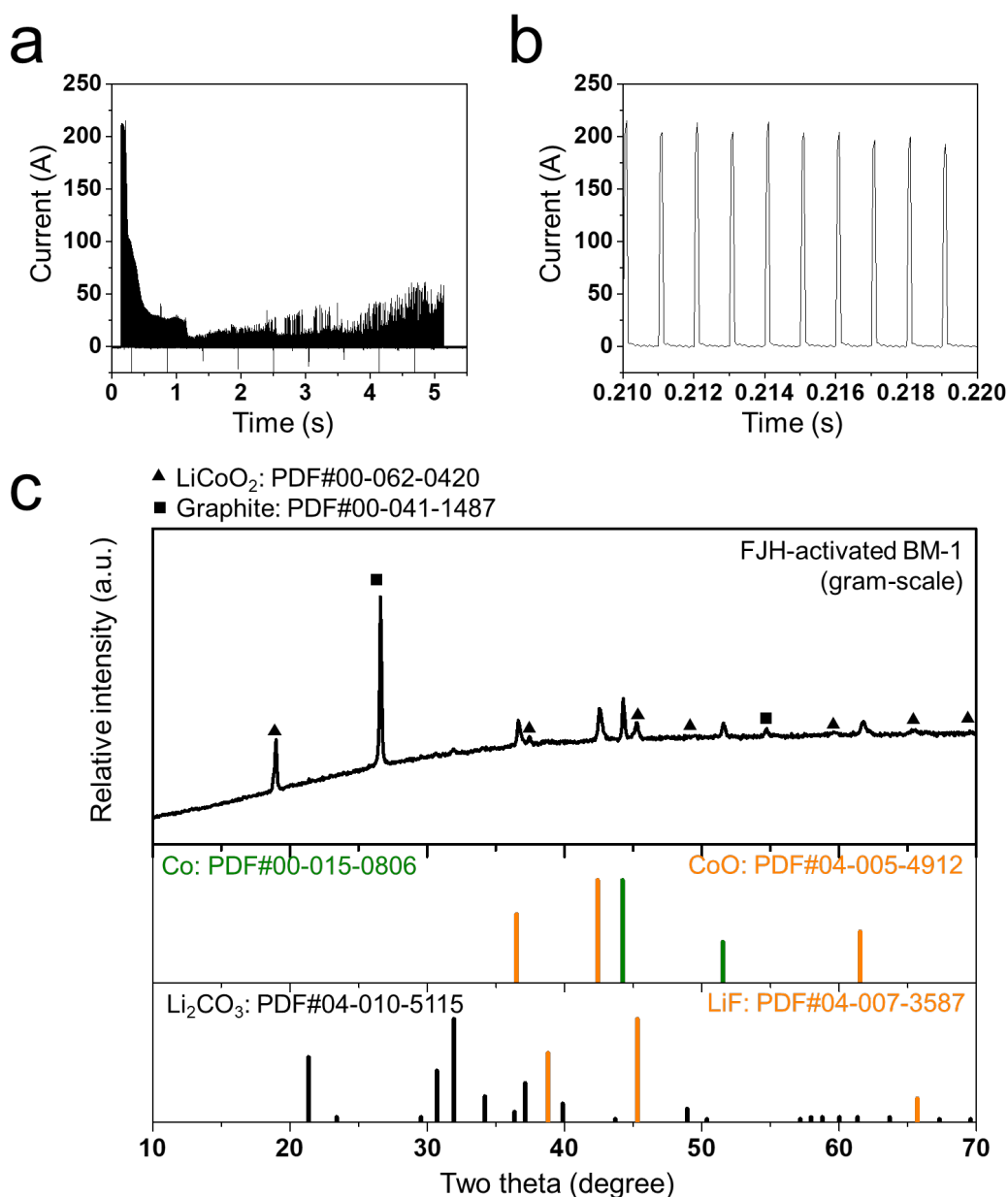
**Supplementary Fig. 30. The crystal structure of various FJH-activated black mass materials with distinct compositions.** BM-7 is the mixture of the black mass, and the cathode includes oxide-type LiCoO<sub>2</sub> and LiNi<sub>0.8</sub>Mn<sub>0.1</sub>Co<sub>0.1</sub>O<sub>2</sub>, as well as the phosphate-type LiFePO<sub>4</sub>.

The relative peak intensities decrease, which indicates the thermal decomposition and conversion of the cathode materials. The formation of simple salts, such as  $\text{Li}_2\text{CO}_3$  and  $\text{Li}_3\text{PO}_4$ , simple oxides, such as  $\text{Li}_2\text{O}$ ,  $\text{Fe}_{0.95}\text{O}$ ,  $\text{NiO}$ ,  $\text{CoO}$ , and  $\text{MnO}$ , as well as the reduced metals Fe, Co, and Ni can be seen after the FJH activation recycling of the black mass BM-7.



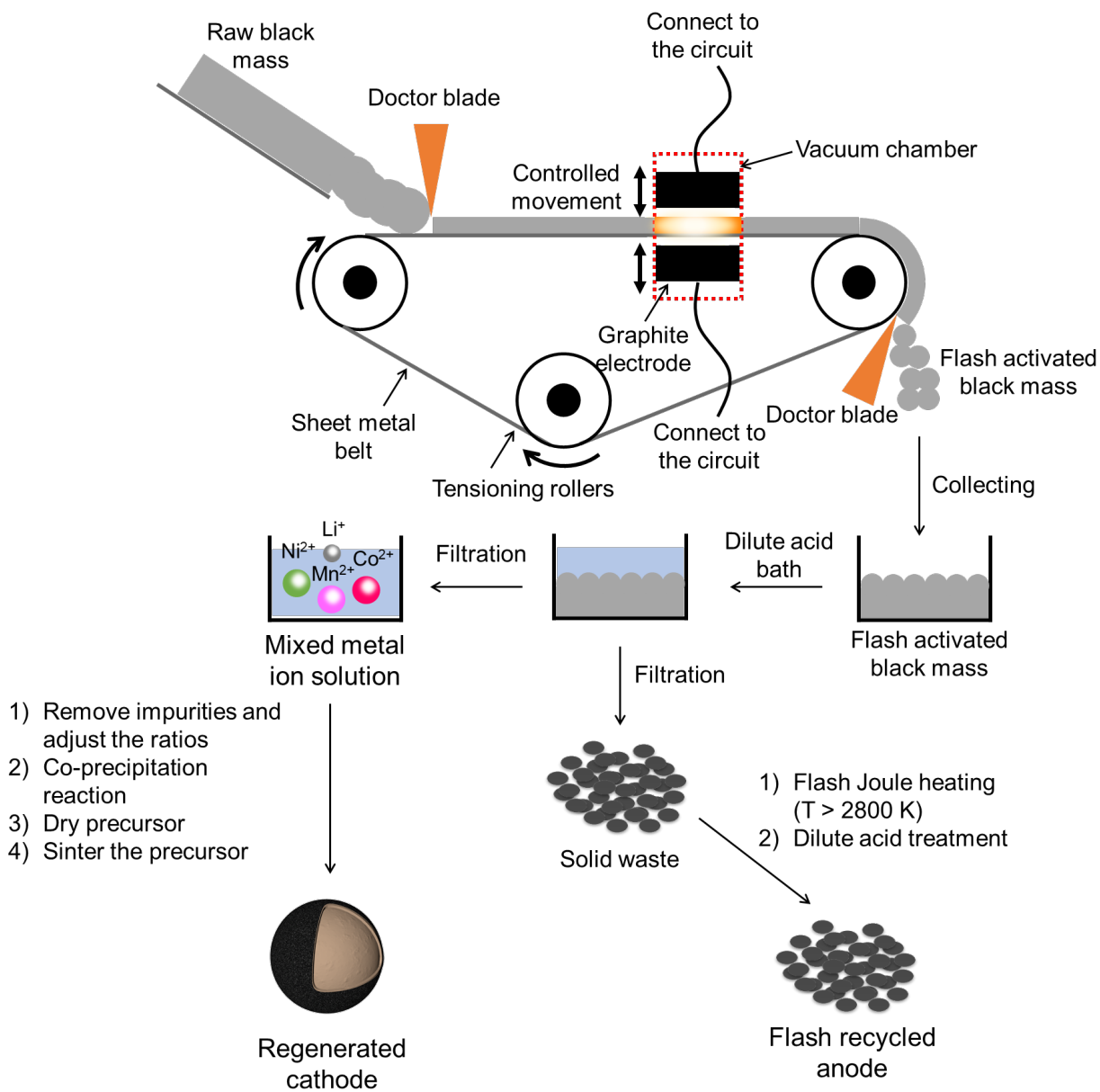
**Supplementary Fig. 31. The improved recovery yield of battery metals from FJH-activated black mass materials with various compositions. a,** The HCl-extractable battery metal

contents (0.1 M, 50 °C, 90 min) and the total quantification of battery metals (*aqua regia*, 50 °C, 90 min) in various black mass, and the recovery yield ( $Y_0$ ) of the battery metals from raw black mass by 0.1 M HCl. The error bars reflect the standard deviations from at least three individual measurements. The same below. **b**, HCl-leachability of battery metal contents (0.1 M, 50 °C, 90 min) from FJH-activated black mass with various chemistries and the total quantification of battery metals (*aqua regia*, 50 °C, 90 min) in various black mass, and the recovery yield ( $Y$ ) of the battery metals from various FJH-activated black mass by 0.1 M HCl. All the leaching durations are 90 min; the BM-1 in Supplementary Fig. 31. The leaching durations of BM-1 and FJH-activated BM-1 by 0.1 M HCl are 24 h to compare the leaching results near the equilibrium. **c**, The increases of the recovery yield ( $Y/Y_0$ ) of total battery metals from various FJH-activated black mass by 1.0 M HCl. **d**, The increases of the recovery yield ( $Y/Y_0$ ) of total battery metals from various FJH-activated black mass by 0.1 M HCl.



**Supplementary Fig. 32. The scaling up trials of the FJH activation process.** **a**, Current curve and **b**, the magnified curve showing the on/off current during the FJH process *via* variable frequency drive. The reactant is black mass BM-1. The detailed flash parameter can be seen in Experimental Section. **c**, The crystal structure of FJH-activated BM-1 prepared in the gram-scale trial. The relative peak intensities decrease, which indicates the thermal decomposition and conversion of the cathode materials. The formation of simple salts, such as  $\text{Li}_2\text{CO}_3$  and  $\text{LiF}$ ,

simple oxides, such as  $\text{CoO}$ , as well as the reduced metals  $\text{Co}$  can be seen after the FJH activation recycling of the black mass BM-1 in the gram-scale trial.



**Supplementary Fig. 33. Conceptual design of a continuous FJH reactor and the subsequent treatment steps to produce regenerated cathode and flash recycled anode.**

**Supplementary Table 1. The material properties and estimated market shares of various cathode materials in the black mass.**

Type	Material	Space group	Specific capacity (mAh g <sup>-1</sup> )	Average price (USD ton <sup>-1</sup> ) <sup>a</sup>	Recoverable metal	Market shares in 2022 <sup>b</sup>	Name <sup>d</sup>
Transition metal oxides (Only transition metal)	HT-LiCoO <sub>2</sub>	R-3m (Layered)	~165	~48000	Li and Co	~10%	BM-1 and BM-5
	LT-LiCoO <sub>2</sub>	Fd-3m (Spinel)	140-190	~48000	Li and Co	<1%	BM-6
	LiNi <sub>x</sub> Mn <sub>y</sub> Co <sub>z</sub> O <sub>2</sub> (NMC-type)	R-3m (Layered)	160-200	16000-22000	Li, Co, Ni, and Mn	~35% <sup>c</sup>	BM-2
Transition metal oxides (With non-transition metal)	LiNi <sub>x</sub> Co <sub>y</sub> Al <sub>z</sub> O <sub>2</sub> (NCA-type)	R-3m (Layered)	~185	~21500	Li, Co, Ni, and Al	~20%	BM-3
Transition metal phosphates	LiFePO <sub>4</sub> , LiCoPO <sub>4</sub>	Pnma (Olivine)	~170	~14000	Li and Fe	~30%	BM-4

Note:

<sup>a</sup> The data is estimated based on Everbatt 2020.

<sup>b</sup> The total market is estimated as ~500 GWh (<https://vspc.com/lithium-ion-batteries/>)

<sup>c</sup> The market shares of the lithiated manganese oxide (LMO, x = z = 0) and lithiated nickel-manganese oxide (LNMO, z = 0) are included here.

<sup>d</sup> BM-7 includes the mixture of the cathode active materials, LiNi<sub>0.8</sub>Mn<sub>0.1</sub>Co<sub>0.1</sub>O<sub>2</sub>, HT-LiCoO<sub>2</sub>, and LiFePO<sub>4</sub> cathodes. The detailed composition can be seen in the Table 1.

**Supplementary Table 2. Gibbs free energy changes during the acid dissolution of common battery metals and their compounds.**

Materials	Reaction	$\Delta G$ (kJ mol <sup>-1</sup> ) per mole metal
Co	$\text{Co(s)} + 2\text{H}^+(\text{aq}) = \text{Co}^{2+}(\text{aq}) + \text{H}_2(\text{g})$	-54.39
CoO	$\text{CoO(s)} + 2\text{H}^+(\text{aq}) = \text{Co}^{2+}(\text{aq}) + \text{H}_2\text{O(l)}$	-38.07
Co <sub>3</sub> O <sub>4</sub>	$\frac{1}{3}\text{Co}_3\text{O}_4(\text{s}) + \frac{8}{3}\text{H}^+(\text{aq}) = \frac{1}{3}\text{Co}^{2+}(\text{aq}) + \frac{2}{3}\text{Co}^{3+}(\text{aq}) + \frac{4}{3}\text{H}_2\text{O(l)}$	19.88
Ni	$\text{Ni(s)} + 2\text{H}^+(\text{aq}) = \text{Ni}^{2+}(\text{aq}) + \text{H}_2(\text{g})$	-45.61
NiO	$\text{NiO(s)} + 2\text{H}^+(\text{aq}) = \text{Ni}^{2+}(\text{aq}) + \text{H}_2\text{O(l)}$	-31.46
Ni <sub>2</sub> O <sub>3</sub>	$\frac{1}{2}\text{Ni}_2\text{O}_3(\text{s}) + 3\text{H}^+(\text{aq}) + \text{Cl}^-(\text{aq}) = \text{Ni}^{2+}(\text{aq}) + \frac{3}{2}\text{H}_2\text{O(l)} + \frac{1}{2}\text{Cl}_2(\text{g})$	-12.34
Mn	$\text{Mn(s)} + 2\text{H}^+(\text{aq}) = \text{Mn}^{2+}(\text{aq}) + \text{H}_2(\text{g})$	-228.03
MnO	$\text{MnO(s)} + 2\text{H}^+(\text{aq}) = \text{Mn}^{2+}(\text{aq}) + \text{H}_2\text{O(l)}$	-84.51
Mn <sub>3</sub> O <sub>4</sub>	$\frac{1}{3}\text{Mn}_3\text{O}_4(\text{s}) + \frac{8}{3}\text{H}^+(\text{aq}) + \frac{2}{3}\text{Cl}^-(\text{aq}) = \text{Mn}^{2+}(\text{aq}) + \frac{4}{3}\text{H}_2\text{O(l)} + \frac{1}{3}\text{Cl}_2(\text{g})$	-29.02
Mn <sub>2</sub> O <sub>3</sub>	$\frac{1}{2}\text{Mn}_2\text{O}_3(\text{s}) + 3\text{H}^+(\text{aq}) + \text{Cl}^-(\text{aq}) = \text{Mn}^{2+}(\text{aq}) + \frac{3}{2}\text{H}_2\text{O(l)} + \frac{1}{2}\text{Cl}_2(\text{g})$	-11.97
MnO <sub>2</sub>	$\text{MnO}_2(\text{s}) + 4\text{H}^+(\text{aq}) + 2\text{Cl}^-(\text{aq}) = \text{Mn}^{2+}(\text{aq}) + 2\text{H}_2\text{O(l)} + \text{Cl}_2(\text{g})$	41.05
Li	$\text{Li(s)} + \text{H}^+(\text{aq}) = \text{Li}^+(\text{aq}) + \frac{1}{2}\text{H}_2(\text{g})$	-282.50
Li <sub>2</sub> O	$\frac{1}{2}\text{Li}_2\text{O(s)} + \text{H}^+(\text{aq}) = \text{Li}^+(\text{aq}) + \frac{1}{2}\text{H}_2\text{O(l)}$	-97.54
Li <sub>2</sub> CO <sub>3</sub>	$\frac{1}{2}\text{Li}_2\text{CO}_3(\text{s}) + \text{H}^+(\text{aq}) = \text{Li}^+(\text{aq}) + \frac{1}{2}\text{H}_2\text{O(l)} + \frac{1}{2}\text{CO}_2(\text{g})$	-64.36
LiF	$\text{LiF(s)} + \text{H}^+(\text{aq}) = \text{Li}^+(\text{aq}) + \text{HF(aq)}$	-15.30
LiCl	$\text{LiCl(s)} + \text{H}^+(\text{aq}) = \text{Li}^+(\text{aq}) + \text{Cl}^-(\text{aq}) + \text{H}^+(\text{aq})$	-29.70
LiOH	$\text{LiOH(s)} + \text{H}^+(\text{aq}) = \text{Li}^+(\text{aq}) + \text{H}_2\text{O(l)}$	-80.77
HCOOLi	$\text{HCOOLi} \cdot \frac{9}{10}\text{H}_2\text{O(s)} + \text{H}^+(\text{aq}) = \text{Li}^+(\text{aq}) + \text{HCOOH(l)} + \frac{9}{10}\text{H}_2\text{O(l)}$	-50.15
Al	$\text{Al(s)} + 3\text{H}^+(\text{aq}) = \text{Al}^{3+}(\text{aq}) + \frac{3}{2}\text{H}_2(\text{g})$	-485.34
Al <sub>2</sub> O <sub>3</sub>	$\frac{1}{2}\text{Al}_2\text{O}_3(\text{s}) + 3\text{H}^+(\text{aq}) = \text{Al}^{3+}(\text{aq}) + \frac{3}{2}\text{H}_2\text{O(l)}$	-59.75
Fe	$\text{Fe(s)} + 2\text{H}^+(\text{aq}) = \text{Fe}^{2+}(\text{aq}) + \text{H}_2(\text{g})$	-78.87
FeO	$\text{FeO(s)} + 2\text{H}^+(\text{aq}) = \text{Fe}^{2+}(\text{aq}) + \text{H}_2\text{O(l)}$	-64.59
Fe <sub>3</sub> O <sub>4</sub>	$\frac{1}{3}\text{Fe}_3\text{O}_4(\text{s}) + \frac{8}{3}\text{H}^+(\text{aq}) = \frac{1}{3}\text{Fe}^{2+}(\text{aq}) + \frac{2}{3}\text{Fe}^{3+}(\text{aq}) + \frac{4}{3}\text{H}_2\text{O(l)}$	-7.11

Materials	Reaction	$\Delta G$ (kJ mol <sup>-1</sup> ) per mole metal
Fe <sub>2</sub> O <sub>3</sub>	$1/2\text{Fe}_2\text{O}_3(\text{s}) + 3\text{H}^+(\text{aq}) = \text{Fe}^{3+}(\text{aq}) + 3/2\text{H}_2\text{O}(\text{l})$	10.75

Note: Ni<sup>3+</sup> and Mn<sup>4+</sup> simple ions are unstable in the aqueous solution and Cl<sup>-</sup> is introduced for the redox reaction. Mn<sub>3</sub>O<sub>4</sub>, Mn<sub>2</sub>O<sub>3</sub>, MnO<sub>2</sub> and Ni<sub>2</sub>O<sub>3</sub> are not soluble in water or dilute acid. Hot concentrated 12 M HCl is required to dissolve the MnO<sub>2</sub> and Ni<sub>2</sub>O<sub>3</sub>, with the emission of Cl<sub>2</sub>.

**Supplementary Table 3. Gibbs free energy changes for the formation of oxides.**

Materials	Reaction	$\Delta G$ (kJ mol <sup>-1</sup> ) per mole O <sub>2</sub>
C	$2\text{C(s)} + \text{O}_2\text{(g)} = 2\text{CO(g)}$	$-221.1 - 0.1780 \times T$
Co	$2\text{Co(s)} + \text{O}_2\text{(g)} = 2\text{CoO(s)}$	$-475.5 + 0.1594 \times T$
	$3/2\text{Co(s)} + \text{O}_2\text{(g)} = 1/2\text{Co}_3\text{O}_4\text{(s)}$	$-455.0 + 0.1929 \times T$
Mn	$2\text{Mn(s)} + \text{O}_2\text{(g)} = 2\text{MnO(s)}$	$-725.8 + 0.1496 \times T$
	$\text{Mn(s)} + \text{O}_2\text{(g)} = \text{MnO}_2\text{(s)}$	$-465.1 + 0.1839 \times T$
Ni	$2\text{Ni(s)} + \text{O}_2\text{(g)} = 2\text{NiO(s)}$	$-480.0 + 0.1888 \times T$
	$4/3\text{Ni(s)} + \text{O}_2\text{(g)} = 2/3\text{Ni}_2\text{O}_3\text{(s)}$	$-326.3 + 0.1866 \times T$
Li	$4\text{Li(s)} + \text{O}_2\text{(g)} = 2\text{Li}_2\text{O(s)}$	$-1191.6 + 0.2456 \times T$

Note: T in the table is the absolute temperature in K.

**Supplementary Table 4. Comparison about the recovery efficiencies of battery metals from spent lithium-ion batteries.**

Materials	Treatments	Reagents	Temp. (°C)	Time (min)	Pulp density <sup>a</sup>	Leaching efficiency (%)		Ref
						Li	TM	
Black mass (Li, Co, Ni)	N/A <sup>b</sup>	1.0 M HCl	50	90	0.4%	62	33	This work
Black mass (Li, Co, Ni)	Flash Joule heating (>2000 K, <1 s)	1.0 M HCl	50	90	0.5%	98	98	This work
Cathode materials (Li, Co, Ni, Mn)	Flash Joule heating	1.0 M HCl	50	90	0.5%	99	99	This work
Black mass (Li, Co, Ni)	Flash Joule heating	1.0 M HCl	85	240	5%	99	92	This work
Black mass (Li, Co, Ni)	Flash Joule heating	0.5 M HCl	85	240	2%	98	93	This work
Black mass (Li, Co, Ni)	Flash Joule heating	0.1 M HCl	85	240	0.5%	99	92	This work
Spent cathode (Li, Co, Ni, Mn)	Drying (353 K, 24 h) Calcination (873 K, 6 h)	6.0 M CH <sub>3</sub> COOH 4% H <sub>2</sub> O <sub>2</sub>	60	10	3.3%	~96	~95	35
Black mass (Li, Co, Mn)	Roasting (773 K, 1 h)	1.75 M HCl	50	120	20%	99	~98	15
Black mass (Li, Co)	Heating (400 K, 1h) Calcination (773-1173 K, 0.5-2 h)	1 M HNO <sub>3</sub> 1.7% H <sub>2</sub> O <sub>2</sub>	75	30	2%	~95	~95	16
Spent cathode (Li, Co)	Combustion (1073 K, 2 h)	1 M HNO <sub>3</sub> 1% H <sub>2</sub> O <sub>2</sub>	80	60	2%	/ <sup>c</sup>	/	17
Spent cathode (Li, Co, Ni, Mn)	Drying (333 K, 24 h) Calcination (883 K, 5 h)	1.5 M lactic acid 0.5 % H <sub>2</sub> O <sub>2</sub>	70	20	2%	~97	~98	18
Spent cathode (Li, Co)	Sonication-assisted leaching (40 kHz, 2 h)	2.0 M H <sub>2</sub> SO <sub>4</sub> 2 % H <sub>2</sub> O <sub>2</sub>	60	120	3.3%	~96	~88	19
Spent cathode (Li, Co)	Vacuum pyrolysis (873 K, 0.5 h)	2.0 M H <sub>2</sub> SO <sub>4</sub> 5 % H <sub>2</sub> O <sub>2</sub>	80	60	5%	~99	~99	20

Materials	Treatments	Reagents	Temp. (°C)	Time (min)	Pulp density <sup>a</sup>	Leaching efficiency (%)		Ref
Spent cathode (Li, Co, Ni, Mn)	Drying (333 K, 24 h) Ultrasonic cleaning (1.5 h)	2.0 M Tartaric Acid 4% H <sub>2</sub> O <sub>2</sub>	70	30	1.7%	~99	~99	21
Spent cathode (Li, Co, Ni, Mn)	Heating (823 K, 1 h)	4.0 M NH <sub>3</sub> 1.5 M (NH <sub>4</sub> ) <sub>2</sub> SO <sub>4</sub> 0.5 M Na <sub>2</sub> SO <sub>3</sub>	80	300	1%	95	~59	22
Cathode materials (Li, Co, Ni, Mn)	N/A	1.0 M H <sub>2</sub> C <sub>2</sub> O <sub>4</sub>	95	720	1%	~95	~7	23
Cathode materials (Li, Co, Ni, Mn)	N/A	4.0 M H <sub>2</sub> SO <sub>4</sub> 30 % H <sub>2</sub> O <sub>2</sub>	80	180	/	~100	~100	24
Black mass (Li, Mn, Fe)	N/A	6.5 M HCl 15% H <sub>2</sub> O <sub>2</sub>	60	120	20%	~92	~91	25
Black mass (Li, Co)	N/A	2.0 M H <sub>2</sub> SO <sub>4</sub> 5 % H <sub>2</sub> O <sub>2</sub>	75	60	10%	~99	~70	26
Black mass (Li, Co)	/	4.0 M HCl	80	60	1%	~97	~97	27
Spent cathode (Li, Co)	N/A	Choline chloride and ethylene glycol (1:2)	180	1440	2%	~90	~50	28
Spent cathode (Li, Co)	Drying (333 K, 8 h), Vacuum pyrolysis (673 K, 2 h) Roasting (773 K, 0.08 h)	SiCl <sub>4</sub> :LiCoO <sub>2</sub> = 3:1 Water	20	/	20%	~98	~96	29
Black mass (Li, Mn)	Oxygen-free roasting (1073 K, 0.75 h)	Water	/	30	1%	~91	/	30
Black mass (Li, Co, Ni, Mn)	Vacuum pyrolysis (973 K, 0.5 h)	Water	/	/	2.5%	~66	/	31
Black mass (Li, Co)	Drying (343 K, 8 h) Preheating (823 K, 1 h), Vacuum pyrolysis (973 K, 0.75 h)	Water	/	/	2.5%	~93	~99 (mass)	32

Materials	Treatments	Reagents	Temp. (°C)	Time (min)	Pulp density <sup>a</sup>	Leaching efficiency (%)		Ref
Black mass (Li, Co)	Oxygen-free roasting (1273 K, 0.5 h) Magnetic separation (293 K, 48 h)	Water	20	2880	0.5%	~70	~75 (mass)	33
Black mass (Li, Co, Ni, Mn)	Preheating (673 K, 2 h) De-coking (1023 K, 6 h) Heating (1873 K, 3 h)	/	/	/	/	~100 (dust)	~100	34

Note:

<sup>a</sup> Pulp density is used to evaluate the solid to liquid ratio and the equation is shown below,

$$Pulp\ density = \frac{dry\ pulp}{Total\ slurry} \times 100\% \quad (17)$$

<sup>b</sup> “N/A” means no pretreatment for the battery materials.

<sup>c</sup> “/” means not mentioned in the literatures.

## Supplementary Table 5. Life cycle inventory of various black mass recycling methods

Hydrometallurgical method<sup>8</sup>

Procedures	Input	Amount	Output	Amount	Notes	Ref
Discharging and collecting	Spent batteries	1.00 kg	Spent batteries (100% SOD)	1.00 kg	1 MJ electricity produces 0.13 kg GHG and 0.67 L water. 1 kg diesel produces 45.6 MJ energy. The data is estimated based on Everbatt 2020. ~5 wt% NaCl solution is used for the discharging process.	9
	Energy	0.03 MJ	GHG	0.004 kg		
	Water	0.52 L				
Shredding	Spent batteries (100% SOD)	1.00 kg	Battery pieces	0.88 kg	The battery pieces included the spent batteries without the electrolyte. The data is the average result from the industrial production (~10 <sup>4</sup> tonne per year), the same below.	8
	Energy	0.38 MJ	GHG	0.050 kg		
	Water	0.26 L				
Low temperature calcination	Battery pieces	1.00 kg	Calcined battery pieces	0.94 kg	The purpose is to separate the active materials with current collectors, to decompose the binder, electrolyte residue and SEI components. The temperature is ~873 K for 2 h.	35
	Energy	6.05 MJ	GHG	0.79 kg		
	Water	4.05 L				
Wet granulation	Calcined battery pieces	1.00 kg	Wet battery pieces	1.00 kg	The amount of water is estimated as ~20 wt% of the solid	36
	Energy	0.007 MJ	GHG	0.001 kg		
	Water	0.205 L				
Density separation	Wet battery pieces	1.00 kg	Spent active materials	0.67 kg	The purpose is to separate the inactive materials, like plastics and steels, and the current collectors	8
	Energy	0.38 MJ	GHG	0.050 kg		
	Water	0.26 L				

Procedures	Input	Amount	Output	Amount	Notes	Ref
Froth flotation	<b>Spent active materials</b>	1.00 kg	<b>Spent cathode powder</b>	0.63 kg	The purpose is to separate the anode materials.	8
	Energy	0.67 MJ	GHG	0.087 kg		
	Water	0.45 L				
Acid leaching	<b>Spent cathode powder</b>	1.00 kg	<b>Leachate</b>	~50 kg	The average pulp density is ~2% and the concentration is ~4M HCl for the calculation in hydrometallurgical method. The density of 12M HCl is ~1.18 g cm <sup>-3</sup> and 4M HCl is ~1.07 g cm <sup>-3</sup>	27
	Energy	0.11 MJ	GHG	0.014 kg		
	Water	30.99 L				
	12 M HCl solution	18.02 kg				

Pyrometallurgical method<sup>8</sup>

Procedures	Input	Amount	Output	Amount	Notes	Ref
Discharging and collecting	Spent batteries	1.00 kg	Spent batteries (100% SOD)	1.00 kg	1 MJ electricity produces 0.13 kg GHG and 0.67 L water. 1 kg diesel produces 45.6 MJ energy. The data is estimated based on Everbatt 2020. ~5 wt% NaCl solution is used for the discharging process.	9
	Energy	0.03 MJ	GHG	0.004 kg		
	Water	0.52 L				
Smelting	Spent batteries (100% SOD)	1.00 kg	Matte (Co, Ni, Mn, Fe, Cu)	0.45 kg	The purpose is to reduce the transition metals and remove all the impurities. The byproducts include the slag with Al, Ca and Li, which requires the post-treatment to recycle the Li salts. The temperature is ~1873 K for 3 h.	8
	Energy	10.8 MJ	GHG	1.41 kg		
	Water	7.24 L				
Gas treatment	Energy	1.33 MJ	GHG	0.17 kg	For exhaust gas treatment	8
	Water	0.89 L				
Granulator	Matte (Co, Ni, Mn, Fe, Cu)	1.00 kg	Fine metal particles	0.99 kg		8
	Energy	0.007 MJ	GHG	0.001 kg		
	Water	0.005 L				
Acid leaching	Fine metal particles	1.00 kg	Leachate	50 kg	The average pulp density is ~2% and the concentration is ~1M HCl for the pyrometallurgical method. The density of	31
	Energy	0.11 MJ	GHG	0.014 kg		

Procedures	Input	Amount	Output	Amount	Notes	Ref
	Water	44.46 L			1M HCl is $\sim 1.06 \text{ g cm}^{-3}$ .	
	12 M HCl solution	4.55 kg				

FJH activation recycling method

Procedures	Input	Amount	Output	Amount	Notes	Ref
Discharge and collecting	Spent batteries	1.00 kg	Spent batteries (100% SOD)	1.00 kg	1 MJ electricity produces 0.13 kg GHG and 0.67 L water. 1 kg diesel produces 45.6 MJ energy. The data is estimated based on Everbatt 2020. ~5 wt% NaCl solution is used for the discharging process.	9
	Energy	0.03 MJ	GHG	0.004 kg		
	Water	0.52 L				
Disassembly and scrapping	Spent batteries (100% SOD)	1.00 kg	Spent active materials	0.61 kg	The spent active materials include spent 37cathode, anode powders and the electrolyte residue. Manual disassembly is considered to separate the spent active materials. The disassembly step can be achieved by a commercial core drill with a silicon carbide blade, which can reduce the manual disassembly cost.	37
	Energy	0.38 MJ	GHG	0.050 kg		
	Water	0.26 L				
Flash Joule heating	Spent active materials	1.00 kg	Flashed active materials	0.80 kg	The yield is ~80% for flashed active materials. The energy consumption is estimated based on gram scale experiment.	This work
	Energy	1.58 MJ	GHG	0.205 kg		
	Water	1.06 L				
Acid leaching	Flashed active materials	1.00 kg	Leachate	20.0 kg	The average pulp density is ~5% and the concentration is ~1M HCl for the pyrometallurgical method. The density of 1M HCl is ~1.06 g cm <sup>-3</sup> . Flash active materials	This work
	Energy	0.17 MJ	GHG	0.022 kg		

Procedures	Input	Amount	Output	Amount	Notes	Ref
	Water	17.38 L			include ~63% cathode materials (reduced transition metals and oxides) compared to the feedstock used in hydrometallurgical method.	
	12 M HCl solution	1.73 kg				

## References

- 1 Fan, W. *et al.* Synthesizing functional ceramic powders for solid oxide cells in minutes through thermal shock. *ACS Energy Lett.* **7**, 1223-1229 (2022).
- 2 Gu, W. *et al.* Compilation and evaluation of gas phase diffusion coefficients of halogenated organic compounds. *R. Soc. Open Sci.* **5**, 171936 (2018).
- 3 Luong, D. X. *et al.* Gram-scale bottom-up flash graphene synthesis. *Nature* **577**, 647-651 (2020).
- 4 Chen, W. *et al.* Ultrafast and controllable phase evolution by flash joule heating. *ACS Nano* **15**, 11158-11167 (2021).
- 5 Deng, B. *et al.* Rare earth elements from waste. *Sci. Adv.* **8**, eabm3132 (2022).
- 6 Ma, X. *et al.* Recycled cathode materials enabled superior performance for lithium-ion batteries. *Joule.* **5**, 1-16 (2021).
- 7 Wyss, K. M. *et al.* Upcycling end-of-life vehicle waste plastic into flash graphene. *Comms. Eng.* **1**, 3 (2022).
- 8 Dai, Q., Gaines, L., Spangenberg, J., Kelly, J. C., Ahmed, S., and Wang, M. Everbatt: A closed-loop battery recycling cost and environmental impacts model. [www.Anl.Gov/egs/everbatt](http://www.Anl.Gov/egs/everbatt). (2019)
- 9 M. Wang, *et al.* Summary of Expansions and Updates in GREET 2020, Lemont, IL, US, 2020 report.
- 10 Scaleup of FJH for graphene synthesis, see: <https://www.universalmatter.com/> (accessed 17 October 2022).
- 11 Chen, W. *et al.* Heteroatom-doped flash graphene. *ACS Nano* **16**, 6646-6656 (2022).

- 12 Ndalamo, J., Mulaba-Bafubiandi, A. F. & Mamba, B. B. UV/visible spectroscopic analysis of  $\text{Co}^{3+}$  and  $\text{Co}^{2+}$  during the dissolution of cobalt from mixed Co-Cu oxidized ores. *Int. J. Miner. Metall.* **18**, 260-269 (2011).
- 13 Furushima, Y. *et al.* Thermal stability and kinetics of delithiated  $\text{LiCoO}_2$ . *J. Power Sources* **196**, 2260-2263 (2011).
- 14 Zhang, C. *et al.* Closed-edged graphene nanoribbons from large-diameter collapsed nanotubes. *ACS Nano* **6**, 6023-6032 (2012).
- 15 Barik, S. P., Prabakaran, G. & Kumar, L. Leaching and separation of Co and Mn from electrode materials of spent lithium-ion batteries using hydrochloric acid: Laboratory and pilot scale study. *J. Clean. Prod.* **147**, 37-43 (2017).
- 16 Lee, C. K. & Rhee, K. -I. Reductive leaching of cathodic active materials from lithium ion battery wastes. *Hydrometallurgy* **68**, 5-10 (2003).
- 17 Li, L. *et al.* Preparation of  $\text{LiCoO}_2$  films from spent lithium-ion batteries by a combined recycling process. *Hydrometallurgy* **108**, 220-225 (2011).
- 18 Li, L. *et al.* Sustainable recovery of cathode materials from spent lithium-ion batteries using lactic acid leaching system. *ACS Sustain. Chem. Eng.* **5**, 5224-5233 (2017).
- 19 Zhu, S. -G. *et al.* Recovery of Co and Li from spent lithium-ion batteries by combination method of acid leaching and chemical precipitation. *Trans. Nonferrous Met. Soc. China* **22**, 2274-2281 (2012).
- 20 Sun, L. & Qiu, K. Vacuum pyrolysis and hydrometallurgical process for the recovery of valuable metals from spent lithium-ion batteries. *J. Hazard. Mater.* **194**, 378-384 (2011).

- 21 He, L.-P., Sun, S.-Y., Mu, Y.-Y., Song, X.-F. & Yu, J.-G. Recovery of lithium, nickel, cobalt, and manganese from spent lithium-ion batteries using l-tartaric acid as a leachant. *ACS Sustain. Chem. Eng.* **5**, 714-721 (2016).
- 22 Zheng, X. *et al.* Spent lithium-ion battery recycling – Reductive ammonia leaching of metals from cathode scrap by sodium sulphite. *Waste Manag.* **60**, 680-688 (2017).
- 23 Li, Q. *et al.* Process synthesis: Selective recovery of lithium from lithium-ion battery cathode materials. *Ind. Eng. Chem. Res.* **58**, 3118-3130 (2019).
- 24 Zou, H., Gratz, E., Apelian, D. & Wang, Y. A novel method to recycle mixed cathode materials for lithium ion batteries. *Green Chem.* **15**, 1183 (2013).
- 25 Huang, Y. *et al.* A stepwise recovery of metals from hybrid cathodes of spent Li-ion batteries with leaching-flotation-precipitation process. *J. Power Sources* **325**, 555-564 (2016).
- 26 Jha, M. K. *et al.* Recovery of lithium and cobalt from waste lithium ion batteries of mobile phone. *Waste Manag.* **33**, 1890-1897 (2013).
- 27 Zhang, P. *et al.* Hydrometallurgical process for recovery of metal values from spent lithium-ion secondary batteries. *Hydrometallurgy* **47**, 259-271 (1998).
- 28 Tran, M. K., Rodrigues, M.-T. F., Kato, K., Babu, G. & Ajayan, P. M. Deep eutectic solvents for cathode recycling of Li-ion batteries. *Nat. Energy* **4**, 339-345 (2019).
- 29 Li, M. *et al.* A SiCl<sub>4</sub>-assisted roasting approach for recovering spent LiCoO<sub>2</sub> cathode. *ACS Sustainable Chem. Eng.* **10**, 8305-8313 (2022).
- 30 Xiao, J., Li, J. & Xu, Z. Recycling metals from lithium ion battery by mechanical separation and vacuum metallurgy. *J. Hazard. Mater.* **338**, 124-131 (2017).

- 31 Xiao, J., Li, J. & Xu, Z. Novel approach for in situ recovery of lithium carbonate from spent lithium ion batteries using vacuum metallurgy. *Environ. Sci. Technol.* **51**, 11960-11966 (2017).
- 32 Tang, Y. *et al.* Recovery and regeneration of LiCoO<sub>2</sub>-based spent lithium-ion batteries by a carbothermic reduction vacuum pyrolysis approach: Controlling the recovery of CoO or Co. *Waste Manag.* **97**, 140-148 (2019).
- 33 Li, J., Wang, G. & Xu, Z. Environmentally-friendly oxygen-free roasting/wet magnetic separation technology for in situ recycling cobalt, lithium carbonate and graphite from spent LiCoO<sub>2</sub>/graphite lithium batteries. *J. Hazard. Mater.* **302**, 97-104 (2016).
- 34 Hu, X., Mousa, E., Tian, Y. & Ye, G. Recovery of Co, Ni, Mn, and Li from Li-ion batteries by smelting reduction - Part I: A laboratory-scale study. *J. Power Sources* **483**, 228936 (2021).
- 35 Zheng, Y. *et al.* Lithium nickel cobalt manganese oxide recovery *via* spray pyrolysis directly from the leachate of spent cathode scraps. *ACS Appl. Energy Mater.* **2**, 6952-6959 (2019).
- 36 Miwa, A., Yajima, T. & Itai, S. Prediction of suitable amount of water addition for wet granulation. *Int. J. Pharm.* **195**, 81-92 (2000).
- 37 Chen, W. *et al.* Flash recycling of graphite anodes. *Adv. Mater.* DOI: 10.1002/adma.202207303. (2022).